2-1-2016

The State-based Peridynamic Lattice Model and Reinforced Concrete Structures

Seth McVey

Seth M McVey
Candidate

Civil Engineering
Department

This thesis is approved, and it is acceptable in quality and form for publication:

Approved by the Thesis Committee:

Dr. Walter Gerstle, Chairperson

Dr. Timothy Ross

Dr. Mahmoud Reda Taha

THE STATE-BASED PERIDYNAMIC LATTICE MODEL AND REINFORCED CONCRETE STRUCTURES

by

SETH M MCVEY

B.S. CIVIL ENGINEERING
CARROLL COLLEGE

THESIS

Submitted in Partial Fulfillment of the
Requirements for the Degree of

Master of Science
Civil Engineering

The University of New Mexico
Albuquerque, New Mexico

November, 2015

ACKNOWLEDGMENTS

This thesis would not have been possible without the guidance of Dr. Walter Gerstle, the support of my gorgeous wife Brittany, the support and encouragement from my parents Mike and Laura McVey and my grandparent-in-laws Bernie and Patricia Gutierrez, and the mercy and grace of my Lord and Savior, Jesus Christ.

"If anyone imagines that he knows something, he does not yet know as he ought to know."

-1 Corinthians 8:2

THE STATE-BASED PERIDYNAMIC LATTICE MODEL AND REINFORCED CONCRETE STRUCTURES

By

Seth M McVey

B.S., Civil Engineering, Carroll College, 2014

M.S., Civil Engineering, University of New Mexico, 2015

ABSTRACT

Continuum mechanics is the leading tool used in computational solid mechanics. Continuum mechanics, however, assumes a material's body to be continuous, represented by analytical functions. This assumption is unrealistic for reinforced concrete structures, which become discontinuous as cracks form.

Silling has proposed a nonlocal theory called peridynamics and Gerstle has specialized his idea to develop the state-based peridynamic lattice model (SPLM). The SPLM sufficiently models nonlinear deformation fields using an organized lattice, force states, and stretches.

In this thesis, we use, develop, and modify the SPLM to model reinforced concrete structures. We use the SPLM to predict the strength of a very large reinforced concrete beam, develop the bond-slip model between steel and concrete in the SPLM, and we demonstrate how to apply loads sequentially to a beam.

TABLE OF CONTENTS

LIST OF FIGURES

LIST OF TABLES

Chapter 1

Introduction

1.1 – Motivation

We live in a world that uses technology for everything. iPhones, iPads, computers, supercomputers, and the like all portray a society bent on technology for survival. Without this technology, our world would look very different. In that aspect, we can appreciate technology and its uses in every part of our lives, including structural design. One of the most significant technological discoveries is the computer. The computer allows scientific research to thrive and researchers to push traditional concepts and principles to their limits and beyond.

Before the computer, structural design and analysis was performed by great minds, such as Newton, Euler, and the Bernoulli brothers using the tools available to them. They used differential calculus to determine the relationship between deflection, slope, and curvature of a structural member. Because of their approach to analyze and represent members using differential calculus, they assumed the member to deform in a continuous way, without accounting for discontinuities. At the time, this assumption seemed reasonable because fracture mechanics was not of interest.

As time progressed, it was determined that fracture and fatigue indeed play a major role in the strength of the materials. Engineers realized, with numerous failures in cars, railroads, and planes, that their assumptions needed to reevaluated and updated. Committees were formed and engineers began to bring unity to the world of design through written, standardized ‘codes’. For example, the American Concrete Institute (ACI), founded in 1904, was founded “to discuss the problem [of unsatisfactory building

requirements for the increased use of concrete] and attempt to bring some order to this expanding use of concrete" [1]. Many more societies and committees all sought to bring order and clarity in both design and construction. These committees have brought more than that, though. They have enabled universities to teach standard engineering design methods; they have brought the engineering industry cheap ways to design and build; and they have enabled organization in the sequence of construction itself.

With the development of these standardized codes comes a sense of tradition. These 'ways of doing things' can become a stumbling block for many engineers who aren't required to think outside the box during their learning years. For example, the idea of fracture mechanics wasn't really discussed or researched until the 1950's. That was only 60 years ago! Earth's history dates way further than that, but our understanding of fracture mechanics, specifically, is still young and growing

Most standard codes these committees write and agree upon are written with the ideas of continuum mechanics. In other words, they use traditional stress and strain principles to determine the size, strength, and material type of a member assuming small deformations. Continuum mechanics also assumes, as stated previously, a continuous deformation field. But testing and research have determined that discontinuities exist in many structural members. For example, where a crack is in a reinforced concrete beam as seen in Figure 1.1, there exists a discontinuity.

Figure 1.1 – Discontinuous deformation field in a reinforced concrete beam (courtesy of http://www.anatech.com/capabilities/material-behavior-modeling/reinforced-and-prestressed-concrete/)

Moreover, when focusing on the crack tip, the linear theory of elasticity would calculate a stress singularity, or where the stress goes to infinity. As a result, a new theory, outside continuum mechanics, called fracture mechanics, was developed to help engineers describe what is occurring where the theory of elasticity predicts stress singularities. But there are several limitations to fracture mechanics, which prevent the engineer from true evaluation and understanding what is actually happening. For example, the fracture process zone (FPZ) for concrete is too big, not allowing one term or another to dominate the solution.

A new material model has been developed called the State-based Peridynamic Lattice Model (SPLM), which takes a different approach to structural analysis. This model recognizes the importance of stress and strain, but predicts strength in a fundamentally different way. The model is used in this thesis to analyze, specifically, reinforced concrete beams. The model simulates a number of phenomena that occur when

a reinforced concrete beam is subject to an applied load. It uses computer technology, which previous generations did not have, to show its applicability in analysis. Although the model has been developed and is able to model members, it is still very young and needs to be used to be understood. Therefore, the motivation for this thesis is to show the model's practicality (or lack thereof) in engineering, especially for the design of reinforced concrete structures.

1.2 – Scope of Thesis: SPLM and Reinforced Concrete

In this thesis we present the developments of the SPLM since Gerstle [2] and others [3, 4, 5], implement these developments into reinforced concrete models, and use the SPLM in a recent competition hosted by the University of Toronto. The SPLM, which allows discontinuities in a deformation field, is based on Newton's three laws on at particle level. In other words, a body is composed of a discrete and finite number of particles that interact with one another according to Newton's laws of motion. Essentially,

- every particle in motion with constant velocity, continues in that state of motion unless an external force is applied to it
- the internal force vector, which is the sum of 18 internal force vectors in a three dimensional SPLM, acting on any particle, is equal to the mass of the particle multiplied by the acceleration vector of the particle
- if particle A exerts a force on particle B, then particle B exerts a force equal in magnitude and directly opposite in direction on particle A

Thus, a constitutive model arises from an assumed relationship between internal forces and internal bond stretches. In previous research [3], only elastic and plastic models were presented. This thesis will describe those models and also include a damage model.

1.3 – Outline of Thesis

This thesis includes seven chapters: Introduction, Literature Review, Revisiting the Bond-Slip Model, Rerun of Gerstle's Beam Trials with a New Bond-Slip Model, Sequential Load Application, Toronto Beam Competition, and a Conclusion.

Chapter Two provides a literature review of all material researched and relevant to this thesis. In this chapter we present Stewart Silling's bond-based and state-based continuum peridynamic models, Walter Gerstle's state-based peridynamic lattice model (SPLM), and the American Concrete Institute's (ACI) approach to structural analysis.

Chapter Three focuses on the bond-slip model we used throughout this thesis. In this chapter we provide previous research done in bond-slip, describe the SPLM's previous bond-slip model, propose a new bond-slip model implemented in the SPLM, and show examples of the new bond-slip model.

Chapter Four presents the new bond-slip model implemented in four simply supported reinforced concrete beams each with a different tensile steel ratio. We present a comparison of these tests against both Gerstle, using the SPLM's original bond-slip model, and the ACI.

Chapter Five describes the implementation of sequential load application in our models. We discuss the problems of not applying load sequentially in the SPLM, the

reasons why stages will benefit future SPLM users, the two stages used in this work, and an example of the sequential load application method.

Chapter Six discusses a competition in which we used the SPLM. We competed against other universities and industries in predicting the shear strength of a very large reinforced concrete beam. We present our prediction, the laboratory results, and our SPLM post-diction of the beam using the bond-slip model discussed in Chapter Three and the sequential load application method discussed in Chapter Five.

Chapter Seven provides a brief summary of this thesis and suggestions for future research in the SPLM.

Chapter 2

Literature Review

This chapter's objectives are to:

- Provide the reader with some background in classical mechanics
- Introduce and describe the work of Silling
- Introduce and describe the work of Gerstle
- Give the reader a methodical understanding of the American Concrete Institute's (ACI318) code for design of reinforced concrete members

Solid members, also referred to as deformable solids, have always been designed and analyzed using classical mechanics. Over the course of several hundred years, engineers and mathematicians have used these classical approaches to design and build the infrastructure of our society, including homes, business parks, entertainment facilities, water and wastewater treatment plants, etc. Engineers have spent valuable time using numerical approaches to design the simplest structures. What if this process could be shortened and improved?

2.1 - Review of Classical Mechanics

Given the desire to ease life and provide tools applicable to improving the world, many have attempted to revise the theories of deformable solids. Before we can describe revisions made to the current theories, including ours, we must understand the fundamentals and motivation of these theory's founders. Modeling solids extends all the way back to early civilization, as far back as the civilizations who built pyramids,

aqueducts, palaces, and fortifying walls. These "engineers", in retrospect, understood simple mathematics, including volume, area, and elevation calculations. Their understanding of these simple concepts manifested in the magnificent structures they were able to design and build.

As time passed, brilliant Greek and Roman philosophers, such as Pythagoras and Euclid took initiative in advancing their mathematical concepts. They taught their pupils and developed concepts still used today. We have these philosophers to thank for principles we use every day including the Pythagorean Theorem and the idea of Euclidian space. Later, natural philosophers (modern engineers), beginning with Leonardo da Vinci began to expand their thinking in the area of solid mechanics and solid modeling. Galileo Galilei, in his infamous cantilever beam problem, which is a simple model, revolutionized solid modeling. He opened the "can of worms" for upcoming natural philosophers, expanding their minds to think outside the box.

Likewise, we owe most of our understanding in the fundamentals of mechanics to Sir Isaac Newton, who gave us three laws that every deformable solid and fluid must follow in our finite four-dimensional, spatio-temporal universe. Newton, in his research [6], assumed that every particle which composed a fluid would react with its surrounding particles. With the application of some force, velocity, or load, he considered how a displacement wave would propagate through the fluid's particles. Although Newton did not explicitly focus on the deformation of solid bodies, he assumed his work could be considered true for solids, as solids are composed of billions of particles which react with each other in some fashion upon deformation. He hypothesized that the particles in a body either attract or repel one another.

Timoshenko in 1953 [7] provided an authoritative piece of work entitled "History of the Strength of Materials", in which he highlights the key figures in the development of the theories as well as putting forth his revision of the theory. However significant the key figures mentioned above are in the role of the development of the theories of deformable solids, it was Claude-Louis Navier and Augustin-Louis Cauchy in their incredible works "Treatise on the Laws of the Equilibrium and Movement of Solid Elastic Bodies" [8] and "Research on the Equilibrium and Interior Movement of Solid or Fluid, Elastic or Non-Elastic, Bodies" [9], respectively, to whom we owe our modern design technique and concepts. Their mathematically rigorous works gave us the concepts of "stress" and strain".

Now that stress and strain were defined, engineers, mathematicians, and researchers, had, with relative ease, ways to analyze the behavior of deformable solids. However, as time progressed following Navier and Cauchy's treatises, problems began to appear in their definition, calling for sub categories of mechanics of materials. For example, a limitation with Navier and Cauchy's theory of linear elasticity, which is based upon stress and strain, is the assumption of continuous deformation.

But, what happens when a crack appears in the body? Doesn't the material body become discontinuous? We now know that the theory of linear elasticity predicts a stress singularity (where the stress and strain go to infinity) at a crack tip. It is obvious that no material can sustain infinite stress or strain. With this infinite stress appearing at the crack tip, a stress-based theory would predict the crack to propagate under negligible loads, which is unrealistic as we know that after a solid member cracks, it continues to sustain significant loads. For instance, a reinforced, simply-supported concrete beam can

experience cracks due to some applied load but continue to sustain significant loads even after the first crack appears.

Therefore, in the middle of the twentieth century, an entirely new branch of mechanics, called fracture mechanics, was developed. The development of fracture mechanics attempted to handle the problem of stress singularities the linear theory of elasticity produced in certain situations. Fracture mechanics, essentially, provided a way for an engineer to describe and understand the singular stress field predicted by the linear elastic model. However, each of these theories still assumes a continuous material body, which is cumbersome to model. How can we model and account for the discontinuities that occur in the body more automatically and consistently?

With advances in computer hardware and software, modeling discontinuous deformation has become a possibility. Computers have allowed programmers and engineers to write codes which can solve both continuous and discontinuous problems. However, it wasn't until recently that discontinuous problems were attempted using computers. Implementing the discrete crack approach, the continuum damage approach, the discrete element approach, and the lattice approach, into a computer program has yielded somewhat successful and satisfying results, but these approaches are over-complicated because of their inability to be easily applied in every day engineering practice.

In 2000, Silling [4] introduced the continuum peridynamic model, which offers a way to include discontinuities. We will discuss Silling's work in the next section and later defend the idea that the state-based peridynamic lattice model (SPLM) has potential to open up new avenues for analysis of reinforced concrete structures.

2.2 – Silling's Work in Peridynamics

The peridynamic model proposed by Silling of Sandia National Labs is derived from its Greek roots 'peri', or near, and 'dynamic', or force. The model Silling developed is nonlocal and assumes a continuous material domain, and does not differentiate between points in the body where a discontinuity in displacement may be located. Peridynamics is categorized as nonlocal because of its ability to consider the interaction between particles separated by finite distances rather than only considering the interaction between particles infinitesimally distant. The model relies on integration, rather than differentiation, in its equations when computing the forces acting between particles, and therefore is valid even at the discontinuities that may occur in the deformation field, which is fundamentally different than previous theories. Silling's first peridynamic model, the bond-based model, is presented next.

2.2.1 – Bond-Based Continuum Peridynamics

Silling introduced the theory of bond-based continuum peridynamics in 2000 [4], which relinquishes an assumption of continuity in the displacement field but continues to assume continuity in the material space. In his journal work, Silling's model starts with the assumption that Newton's second law holds true on every infinitesimally small differential volume (continuum material particle) within the material domain. The bond-based model, furthermore, also assumes that the force between any two particles in a material body is a function only of the states of *those two* particles. This implies, according to Silling, that these two particles are insensitive to the states of other nearby particles. This assumption was later revised by Silling [5] to the state-based peridynamic

model, where he assumed that the force between two particles may depend upon the states of all neighboring particles contained within a specified material horizon.

In the bond-based model, a solid body composed of a finite number of particles occupies an initial, undeformed reference configuration, each represented by the reference vector $\boldsymbol{X}$. An important concept, as indirectly stated above, in the bond-based model is that each particle, $\boldsymbol{X}$, resides in a real Cartesian space, or within a continuous material space. Each particle in the material body interacts with neighboring particles by means of a pairwise force function, $\boldsymbol{f}$. The pairwise force function has units of force-per-volume squared and defines the constitutive model for any material:

$$\boldsymbol{f}(\boldsymbol{u}' - \boldsymbol{u}, \boldsymbol{X}' - \boldsymbol{X}) = \boldsymbol{f}(\boldsymbol{\eta}, \boldsymbol{\xi}), \text{ where} \qquad \textbf{(2.1)}$$

$\boldsymbol{f}$ is a function of the undeformed reference positions, $\boldsymbol{X}'$ and $\boldsymbol{X}$, and the displacements, $\boldsymbol{u}$ and $\boldsymbol{u}'$, of two different particles. Let it be noted that the undeformed, reference vectors are represented as $\boldsymbol{X}$ and the deformed, current vectors are represented as $\boldsymbol{x}$. These two particles potentially interact with each other if they are within a material horizon, δ, in the reference configuration. Silling defines relative position as $\boldsymbol{X}' - \boldsymbol{X} = \boldsymbol{\xi}$ and relative displacement as $\boldsymbol{u}(\boldsymbol{X}', \boldsymbol{t}) - \boldsymbol{u}(\boldsymbol{X}, \boldsymbol{t}) = \boldsymbol{\eta}$. In the bond-based peridynamic model, $\boldsymbol{f}$ is completely dependent on $\boldsymbol{\xi}$ and $\boldsymbol{\eta}$ and consequently independent of the deformations of other surrounding particles. The pairwise forces acting between any two particles are equal, opposite, and collinear with the particle's deformed position so that no couple develops and Newton's third law is obeyed.

According to Silling, each particle has a mass density, $\boldsymbol{\rho}$ and, therefore, the equation of motion is:

$$\boldsymbol{\rho}(\boldsymbol{X})\ddot{\boldsymbol{u}}(\boldsymbol{X}, \boldsymbol{t}) = \int_{\mathcal{H}_x} \boldsymbol{f}(\boldsymbol{\eta}, \boldsymbol{\xi}) dV_{\boldsymbol{X}'} + \boldsymbol{b}(\boldsymbol{X}, t), \text{ where} \qquad \textbf{(2.2)}$$

$\mathcal{H}_x$ is the material neighborhood surrounding particle $\boldsymbol{X}$ and $\boldsymbol{b}$ is the prescribed body force density field acting on each particle. Figure 2.1 shows the bond-based model.

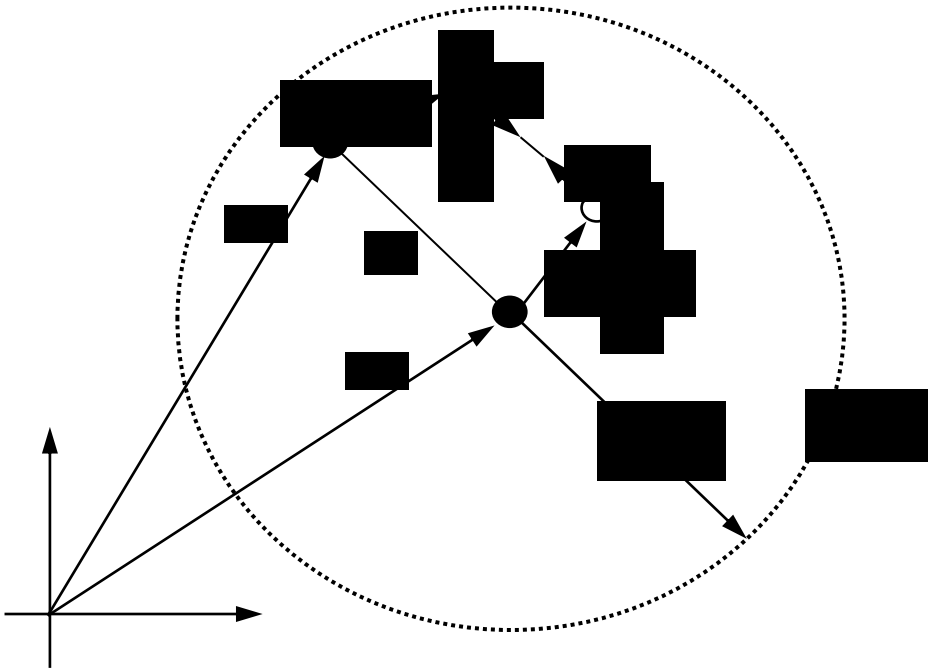

Figure 2.1 – Bond-based continuum peridynamic model

$\boldsymbol{\xi}$ defines the relative, undeformed position vector and is also called the 'bond' between the two interacting particles. The nonlocal bond over a finite distance between the two interacting particles is what makes the bond-based peridynamic fundamentally different from local continuum mechanics theories.

Although Silling and others were able to model damage and cracking using the bond-based peridynamic theory [10, 11, 12], several limitations were found. For example, plasticity can be modeled using the bond-based theory but this process does not prevent volumetric plastic strain, which is unrealistic in metals. The bond-based theory shows great potential but because of its limitations, Silling introduced the state-based peridynamic model, discussed next.

2.2.2 – State-Based Peridynamics

In the state-based peridynamic model, Silling [5] makes a fundamental change to his bond-based theory. That is, he now defines the interactions between particles using *force states* rather than *pairwise force functions*. Recalling that the pairwise force function, $\boldsymbol{f}$, is a function only of the relative position, $\boldsymbol{\xi}$, and relative displacement, $\boldsymbol{\eta}$, of the two interacting particles, Silling now proposes that the force state acting on any particle in the material body is dependent on all the particles located within the particle's material neighborhood, $\mathcal{H}$, with radius δ. These states are represented by an infinite set of tensors, elements of the set of m^{th}-order tensors, $\mathcal{L}_m$, located within a spherical material neighborhood.

In light of the limitation of the bond-based model – that the model was defined in terms of pairwise force functions, $\boldsymbol{f}$, and not tensor states – Silling argues that, like a second order tensor's ability to map vectors into vectors, so too do force states but with three major differences. One, a state is not, in general, a linear function of $\boldsymbol{\xi}$. Two, a state, in general, is not a continuous function of $\boldsymbol{\xi}$. And three, states are infinite dimensional, meaning there can be an infinite number of bonds between particles as long as the particles are within each other's material neighborhood making $\boldsymbol{f}$ a function of an infinite number of particle states. Because of these three differences, Silling develops two key tools to help the engineer understand vector states in terms of second order tensors and vice versa. The first tool is termed *expansion*, $\underline{\mathrm{e}}$, which is a function that expands a second order tensor $\mathbf{Q}$ into an equivalent vector state:

$$\underline{\mathrm{e}}(\mathbf{Q}) = \underline{\mathbf{Q}}\langle\boldsymbol{\xi}\rangle \quad \forall\boldsymbol{\xi} \text{ within } \mathcal{H}, \tag{2.3}$$

where the angle brackets refer to the bond on which the state operates and ∀ means 'for all values of'. The second tool is termed *reduction*, $\mathcal{R}$, which is a function that reduces a vector state of a particle to an approximately equal second order tensor, **A**:

$$\mathcal{R}(\underline{\mathbf{A}}\langle\boldsymbol{\xi}\rangle) = \mathbf{A}\boldsymbol{\xi} \quad \forall\boldsymbol{\xi} \text{ within } \mathcal{H}. \tag{2.4}$$

To execute these two tools, Silling needed to define several terms including the *influence function*, *tensor product*, the *reference position vector state*, and the *shape tensor*. The author finds defining these terms irrelevant to the current work, but if the reader is interested, the definition and explanation of each term can be found in Silling's work [5] or Raybeau Richardson's work [3].

Further, there are two kinds of force states in which particle forces act: *ordinary* and *non-ordinary*, as shown in Figure 2.2.

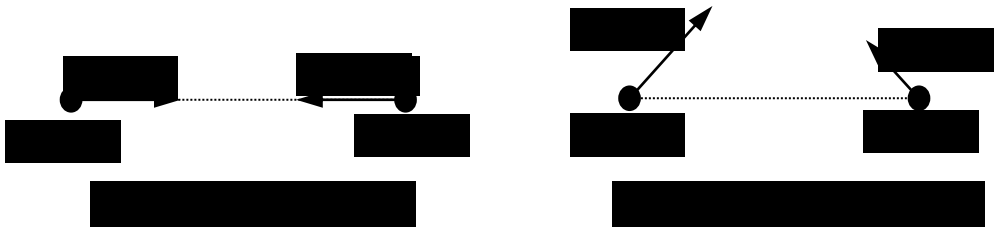

Figure 2.2 – Force states of particles in the state-based peridynamic model

The state-based model changes the equation of motion by replacing the pairwise force functions with the force vector state field of the particle:

$$\rho\ddot{\boldsymbol{u}} = \int_{\mathcal{H}_x}\{\underline{\boldsymbol{T}}\langle\boldsymbol{X}'-\boldsymbol{X}\rangle - \underline{\boldsymbol{T}}'\langle\boldsymbol{X}'-\boldsymbol{X}\rangle\}dV_{\boldsymbol{X}'} + \boldsymbol{b}. \tag{2.5}$$

In this equation, the particle acceleration, $\rho\ddot{\boldsymbol{u}}$, is equal to the body force, $\boldsymbol{b}$, plus the force state at $\boldsymbol{X}$ represented by $\underline{\boldsymbol{T}}\langle\boldsymbol{X}'-\boldsymbol{X}\rangle$ minus the force states of all particles $\boldsymbol{X}'$ which act upon $\boldsymbol{X}$, represented by $\underline{\boldsymbol{T}}'\langle\boldsymbol{X}'-\boldsymbol{X}\rangle$, integrated over the material horizon, $\mathcal{H}_x$.

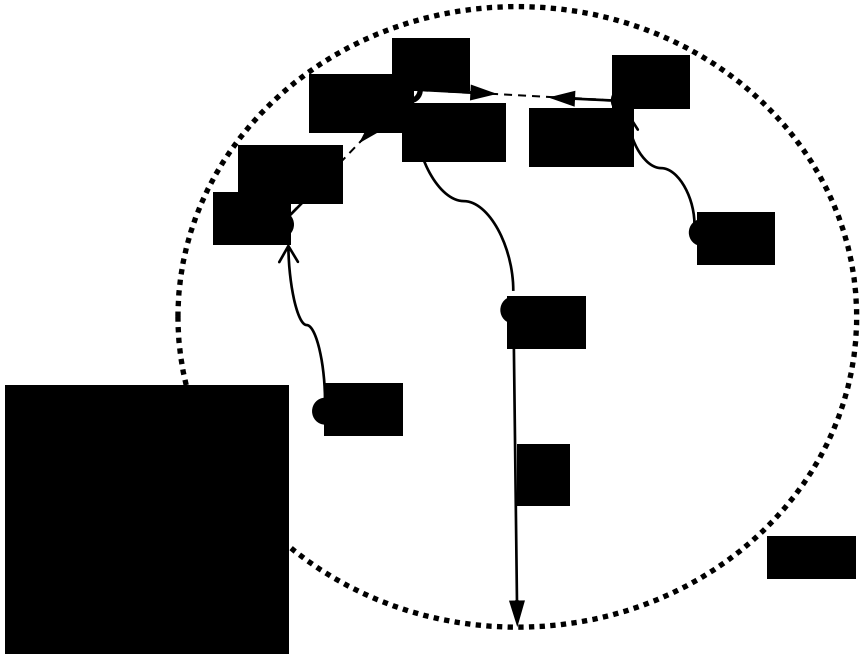

Figure 2.3 – State-based continuum peridynamic model

In Figure 2.3, particle $\mathbf{X}^{\boldsymbol{i}}$ is contained within a circular region, $\mathcal{H}_x$, that undergoes some deformation. Particle $\mathbf{X}^{\boldsymbol{i}}$ is surrounded by many particles, even perhaps an infinite number, which are within the material horizon, δ, and within the material neighborhood, $\mathcal{H}_x$. Each particle has an initial reference position, **X,** and deforms to $\boldsymbol{x}$. We can then develop the deformation state $\underline{\mathbf{Y}}$ of the particle in focus, $\mathbf{X}^{\boldsymbol{i}}$, and reduce the deformation state to a second order tensor using Equation 2.4. This second order tensor is shown in [5] to be approximately equal to the deformation gradient found using continuum mechanics. The deformation gradient can then be used to find the first Piola-Kirchhoff stress tensor and consequently we can expand the force state $\underline{\mathbf{T}}$ using Equation 2.3 to find the relation between the force state of particle **X** and the Piola-Kirchhoff stress tensor:

$$\underline{\mathbf{T}}\langle \boldsymbol{\xi} \rangle = \underline{\varepsilon}(\mathbf{P^o}). \qquad \textbf{(2.6)}$$

Silling, thus, has created a more general approach than what he first laid out in the bond-based model and from what we see in continuum mechanics. Although he generalized his method, it is perhaps too general to be implemented into practical models. For instance, his model still leaves the user to define material parameters in the model, including the material horizon, the influence function and the discretization amongst other things.

Silling uses a continuum mechanics approach to find the stress tensor after reducing the deformation state then expands that stress tensor using his *expansion method*. We, like [3] and [2], feel there is no need to base our conclusions on continuum mechanics approaches. By doing so, we are assuming the continuum mechanics approaches are correct in every situation. Engineers are finding that there are problems with continuum mechanics approaches, which have been discussed earlier and will be discussed further later in this chapter.

2.3 – Gerstle's State-Based Peridynamic Lattice Model

To aid in implementing Silling's bond-based and state-based models discussed in Section 2.3, Gerstle introduced the state-based peridynamic lattice model (SPLM) [2]. This model was proposed because Gerstle was unable to use the previous models to simulate three-dimensional elastic bodies with Poisson's ratios different from one-quarter. This model uses the same principles Silling proposed, but adds a particle lattice. A particle lattice allows the user to reduce the number of particles in a body from infinite to a quantifiable number. Because the peridynamic states are infinite-dimensional due to an infinite number of particles in the continuum, the lattice reduces the peridynamic state

to a finite-dimensional object. Three essential models are implemented using the SPLM, which we will present here:

- an elastic model
- a plastic model
- and a damage model.

2.3.1 – SPLM Lattice Model

According to Gerstle, an N_R-dimensional lattice, Λ^{N_R}, contains an infinite number of lattice points located in $\mathbb{R}^{N_R}$, a N_R-dimensional Euclidian space. Consider $\mathcal{R}$ an N_R-dimensional solid body located in $\mathbb{R}^{N_R}$. He defines the lattice body, $\mathcal{L}_{\mathcal{R}}$, and its topology as:

$$\mathcal{L}_{\mathcal{R}} = \{\Lambda^{N_R} \cap \mathcal{R}, P_{\phi}\}. \quad \textbf{(2.7)}$$

In other words, "the lattice body $\mathcal{L}_{\mathcal{R}}$ contains a subset of particles with the region $\mathcal{R}$, as well as a null particle P_{ϕ}." [2, pp. 186] Thus, if $\mathcal{R}$ is a finite volume, $\mathcal{L}_{\mathcal{R}}$ contains a finite number of particles, each with a finite mass and volume. These particles are arranged as a Face-Centered Cubic (FCC) lattice, as shown in Figure 2.4.

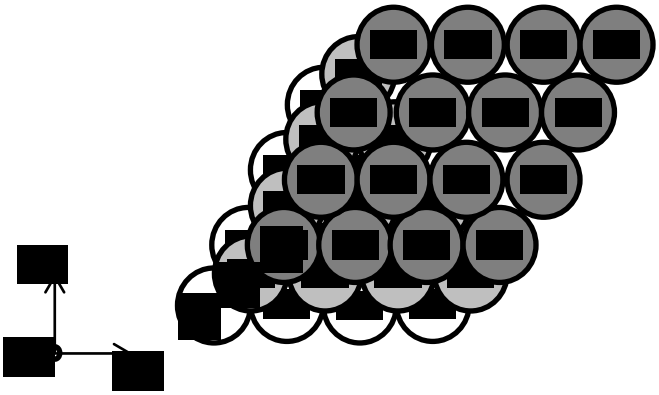

Figure 2.4 – FCC configuration (from [2] pp. 187)

The topology, furthermore, is shown in Figure 2.5:

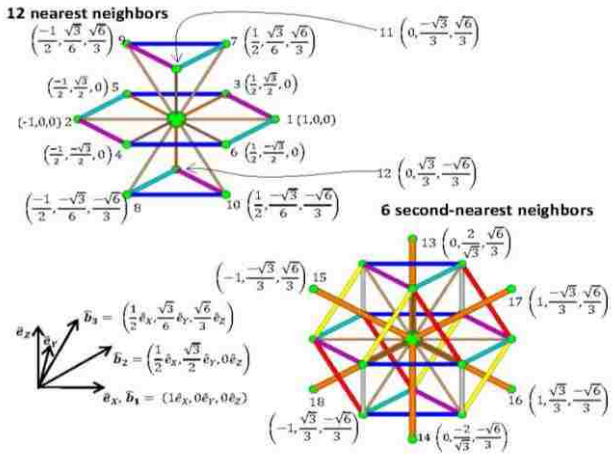

Figure 2.5 – Lattice topology in the SPLM (from [2] pp. 191)

There are a few definitions Gerstle gives that will help us understand the implementation of lattice bodies and their corresponding topologies into computational analysis. First, he defines a *structure* as a collection of lattice bodies $\mathcal{L}_{\mathcal{R}}$, where these lattice bodies interact only through body interactions. Next, he defines a *material body* as an object which contains a lattice body with a corresponding particle bond list, a neighbor list for each of the particles in the lattice body, which lists particles and their neighboring particles, a particle mass, and a *peridynamic force state function*, $\widetilde{\mathbf{T}}$. Within the material body are material particles, which are characterized by particle fixed attributes and particle alterable attributes. These particles will have some attributes that are unchanging and other attributes that change upon loading. The *peridynamic force state function*, $\widetilde{\mathbf{T}}$, relates the force state, $\underline{\mathbf{T}}$, and the deformation state, $\underline{\mathbf{Y}}$, which includes particle position, damage, plastic stretch, and temperature. Finally, a *body interaction* specifies how the material particles interact with each other.

With these definitions and understanding of a particle lattice, we can discuss the three key models Gerstle developed for the SPLM.

2.3.2 – Elastic SPLM

In elasticity, a body returns to its original state after the load is removed. The SPLM avoids the continuum mechanics approaches to determining the constitutive behavior, specifically stress and strain. Gerstle uses the ideas of *force* and *stretch* instead. Stretch is defined as:

$$S_j = \frac{|\boldsymbol{x}_R[\mathrm{P}_i,t]\langle B_j\rangle| - |\boldsymbol{X}_R[\mathrm{P}_i,t]\langle B_j\rangle|}{|\boldsymbol{X}_R[\mathrm{P}_i,t]\langle B_j\rangle|} = \frac{L-L_0}{L_0}, \text{ where} \tag{2.8}$$

$$L \equiv \sqrt{\left(x_j - x_i\right)^2 + \left(y_j - y_i\right)^2 + \left(z_j - z_i\right)^2}, \text{ and} \tag{2.9}$$

$$L_0 \equiv \sqrt{\left(X_j - X_i\right)^2 + \left(Y_j - Y_i\right)^2 + \left(Z_j - Z_i\right)^2}. \tag{2.10}$$

In the equations above, L_0 is the initial, reference configuration length of the bond between particle i and particle j, and L is the deformed length of the bond between particle i and particle j. Because each particle can have up to 18 bonds with neightboring particles in three dimensions due to the lattice topology, the stretch matrix is therefore:

$$\{S\}_i = \begin{Bmatrix} S_1 \\ \vdots \\ S_j \\ \vdots \\ S_{18} \end{Bmatrix}_i. \tag{2.11}$$

It is noteworthy to mention that there may not exist 18 non-null neighbors for particles located on the lattice body.

The force matrix, $\{T\}$, is similar to the stretch matrix in that there are potentially 18 forces that any given particle can interact with:

$$\{T\}_i = \frac{1}{2}\begin{Bmatrix} F_1 \\ \vdots \\ F_j \\ \vdots \\ F_{18} \end{Bmatrix}_i . \qquad \textbf{(2.12)}$$

Essentially, force state $\{T\}$ is one-half of the vector of peridynamic force magnitudes, $\{F\}$, acting in each bond direction, directed away from the particle seen in Figure 2.3. Therefore, the magnitude of the pairwise force acting on any particle, P_i, due to interaction with its neighbor is:

$$F_i\langle B_j\rangle = \left|\underline{\mathbf{T}}[P_i]\langle B_j\rangle\right| - \left|\underline{\mathbf{T}}\left[\mathcal{N}[P_i]\langle B_j\rangle\right]\langle B_j{}'\rangle\right|, \text{ where} \qquad \textbf{(2.13)}$$

$\underline{\mathbf{T}}[P_i]\langle B_j\rangle$ is the bond-based force vector state field evaluated at every time step and $\underline{\mathbf{T}}\left[\mathcal{N}[P_i]\langle B_j\rangle\right]\langle B_j{}'\rangle$ is the bond-based force vector state field of the neighboring particle evaluated at every time step.

Finally, Gerstle establishes the relationship between the force matrix, $\{F\}$, and the elastic stretch matrix, $\{S^e\}$:

$$\{F\} = [K]\{S^e\}, \text{ where} \qquad \textbf{(2.14)}$$

$[K]$ is an 18 x 18 symmetric matrix called the *micro-elastic SPLM spring stiffness matrix*. $[K]$ is defined in terms of constants *a*, *b*, and *c*:

$$[K] = \begin{bmatrix} \begin{bmatrix} a+b & b & \cdots & b \\ b & a+b & \ldots & b \\ \vdots & \vdots & \ddots & \vdots \\ b & b & \ldots & a+b \end{bmatrix} & \begin{matrix}[0] \\ (12 \text{ x } 6)\end{matrix} \\ \begin{matrix}(12 \text{ x } 12)\end{matrix} & \begin{bmatrix} c & 0 & \ldots & 0 \\ 0 & c & 0 & \vdots \\ \vdots & 0 & \ddots & 0 \\ 0 & \ldots & 0 & c \end{bmatrix} \\ \begin{matrix}[0] \\ (6 \text{ x } 12)\end{matrix} & \begin{matrix}(6 \text{ x } 6)\end{matrix} \end{bmatrix}. \qquad \textbf{(2.15)}$$

By equating the classical strain energy density equation to the peridynamic strain energy density equation, Gerstle solves for *a*, *b*, and *c*:

$$a = \frac{EL^2}{\sqrt{2}(\nu+1)}, \tag{2.16}$$

$$b = \frac{\sqrt{2}EL^2(1-4\nu)}{32(2\nu-1)(\nu+1)}, \text{ and} \tag{2.17}$$

$$c = \frac{EL^2}{4(\nu+1)} = \frac{1}{2\sqrt{2}}a. \tag{2.18}$$

Thus, Gerstle has developed the elastic "spring stiffness" between interacting particles under spatially homogeneous deformations fields as a function of only E and ν. Gerstle, goes through an extensive explanation explaining the relationship between *force* and stress and *stretch* and strain, verifying the elastic behavior of particles, which may be referred to if desired [2, pp. 253-262].

2.3.3 – Plastic SPLM

Gerstle [2] asserts that an elastic-plastic model can be developed without reverting to continuum mechanics' stress and strain concepts. In the SPLM, the total stretch is computed, as seen in Equation 2.8, and this is a summation of the elastic stretch matrix $\{S^e\}$ and the plastic stretch matrix $\{S^p\}$:

$$\underline{S^e}[P_i]\langle B_j\rangle = \underline{S}[P_i]\langle B_j\rangle - \frac{1}{2}\left(\underline{S^p}[P_i]\langle B_j\rangle + \underline{S^p}[P_k]\langle B_j\rangle\right). \tag{2.19}$$

With this equation arises a question: when does plastic stretch commence? Gerstle outlines two approaches to answer this question.

In his *first force state plasticity model*, he assumes that plastic flow commences when the norm of the deviatoric component of the force matrix reaches a specified value $F_{devYield}$, which is a measure of the critical force state. He found that this assumption was

no good because the yield criterion depended upon elastic parameters and not *only* upon force state. Therefore, he proposed the second plastic model which depended on force state alone.

Assuming that a material will yield when the strain energy density of the deviatoric component of the stress reaches a critical value, Gerstle introduces the J_2 plasticity criterion. In the SPLM, J_2 is equivalent to Von Mises plasticity. By definition $J_2 = k^2$, where k is a material constant equal to $k = \tau_{Yield} = \frac{\sigma_{Yield}}{\sqrt{3}}$. If J_2 is less than k^2, then the material only deforms elastically and no plastic flow takes place. Gerstle, using previous equations in [2], derives J_2 as it applies in the SPLM as:

$$J_2 = \frac{1}{36L^4}(A + B + C + D + E + F) \quad \textbf{(2.20)}$$

where A, B, C, D, E, and F are constants defined in terms of the components of the force matrix, $\{F\}$. If J_2 becomes greater than k^2, then the plastic flow, $\{\Delta S^p\}$, can be calculated as follows:

$$\{\Delta S^p\} = \Delta\lambda \frac{\{F_{dev}\}}{F_{devYield}}, \text{ and} \quad \textbf{(2.21)}$$

$$\Delta\lambda = \frac{\sigma_{Yield}}{E}\left(\frac{\|F_{dev}\|}{F_{devYield}} - 1\right). \quad \textbf{(2.22)}$$

Gerstle closes his explanation of plasticity with, "The primary advantage of the SPLM model is that it allows one to combine damage and fracture with plasticity" ([2], pp. 296). We next consider damage.

2.3.4 – SPLM Damage

Gerstle seeks to develop a damage model that is independent of lattice rotation, at least under conditions of spatially homogeneous strain. Within the SPLM, the user has

the ability to rotate the lattice, which could affect crack propagation. However, this non-objectivity is minimized by defining the damage model as a scalar function.

The SPLM stipulates that damage commences when:

$$S_{Avg} = \epsilon_t \left(\frac{1-2\nu}{3}\right) = \frac{\sigma_t}{E}\left(\frac{1-2\nu}{3}\right), \text{ where} \quad \textbf{(2.23)}$$

$$S_{Avg} = \frac{\sum S_i}{18}. \quad \textbf{(2.24)}$$

The damage commences when the average stretch, S_{Avg}, reaches a critical value, $S_{AvgCrit}$. However, this only establishes when the damage will commence. After the damage commences, Gerstle uses an equivalent crack opening displacement, COD_{eq}, to activate crack evolution. The crack opening displacement is equal to $COD_{eq} = S_{TotMax}L$, where S_{TotMax} is the maximum stretch of any bond connected to a particle in focus taking into account both elastic and plastic stretches and L is the lattice spacing. Therefore, tensile damage ω develops according to:

- if $S^e_{Avg} < S_{AvgCrit}$ then $\omega = \max(0, \omega_{prev})$,
- elseif $COD_{eq} \leq COD_c$ then $\omega = \max\left(1 - \frac{\gamma \frac{\sigma_t L}{E COD_c}(COD_c - COD_{eq})}{COD_c}, \omega_{prev}\right)$,
- else $\omega = 1$, where **(2.25)**

S^e_{Avg} is the average elastic stretch of all 18 bonds on a particle, COD_c is the critical crack opening displacement, σ_t is the tensile strength of concrete, and γ is shown in Figure 2.6.

In other words, if the average elastic stretch, S^e_{Avg}, is less than the critical stretch, $S_{AvgCrit}$, then the tensile damage is the maximum of 0 and the value of damage the particle had in the previous time step. Or, if the crack opening displacement, meaning damage has already initiated and which takes into account both the elastic and plastic

stretches, is less than or equal to the critical crack opening displacement, COD_c, then the tensile damage is the maximum of the previous time step's damage and an equation that takes into account the tensile stretch. Or, the particle experiences complete damage, when $\omega = 1$ and $COD_{eq} > COD_c$. Figure 2.6 shows the damage model.

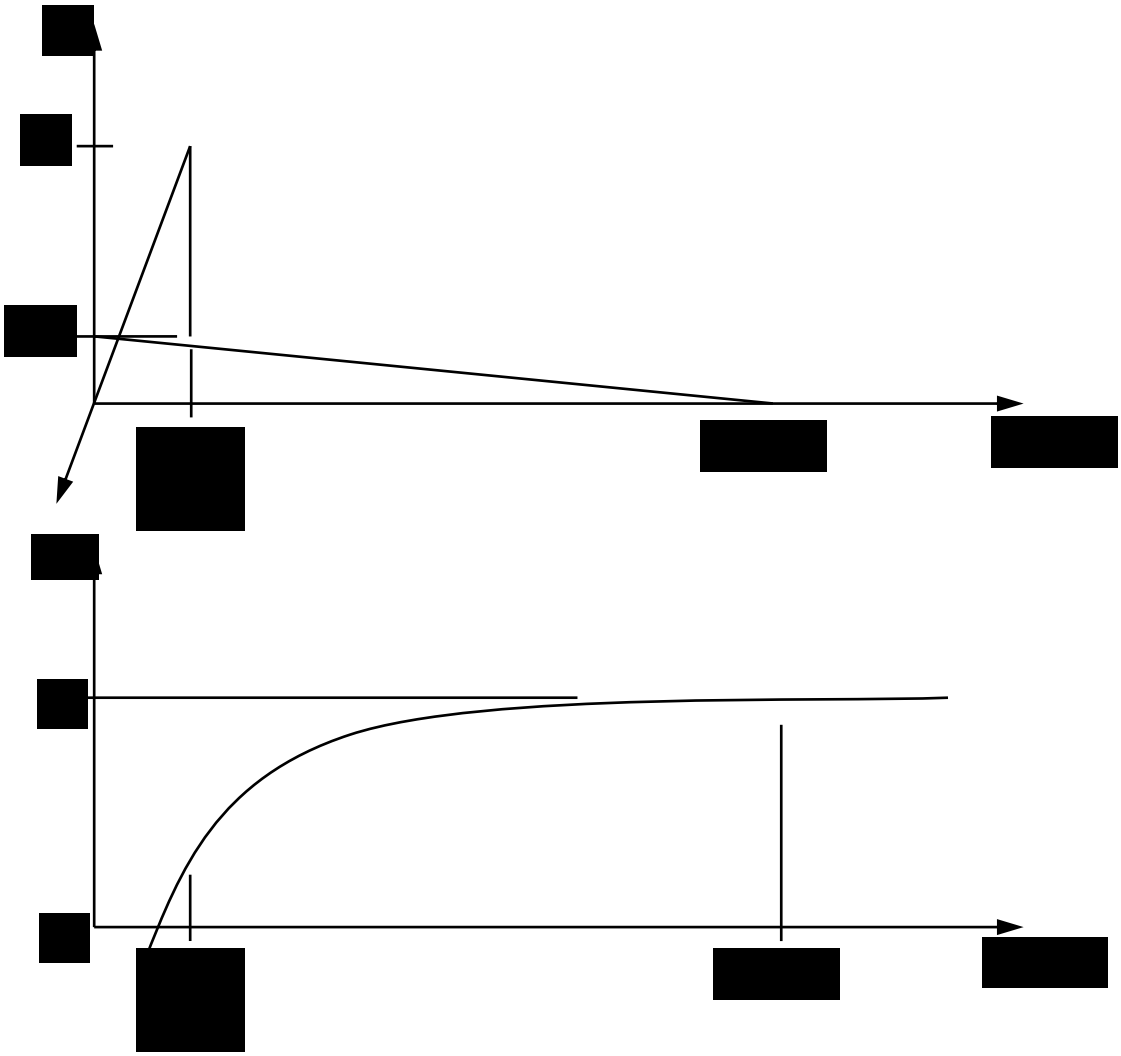

Figure 2.6 – Stress versus equivalent crack opening displacement (top) and damage versus equivalent crack opening displacement (bottom) (from [2] pp. 320)

This damage model is, as described by Gerstle, perfectly isotropic in a homogeneous deformation field, but only up to the point when damage initiates. This is the point in the top graph in Figure 2.6 where the stress exactly hits the tensile stress, σ_t. According to Gerstle's damage model, damage will develop once initiated and may eventually manifest in a macrocrack. But because damage initiation is not a function of lattice rotation, the damage evolution is reasonably objective when it comes to crack propagation.

We discuss the American Concrete Institute (ACI) design methods in the next section.

2.4 – ACI Code

ACI318 [13] is usually used in designing concrete structures. There are noteworthy constraints in the ACI and in Chapter 6 we will show the limitations when using the ACI in certain situations. The ACI Code was developed to aid in the design of concrete structures within the United States. It is founded on the ideas and fundamental principles of continuum mechanics, as it uses stress and strain to ensure safety and security. Although the ACI uses these principles, there are still plenty assumptions made to predict the strength, such as the allowable maximum moment of a beam. We have to thank hundreds of engineers in the development of these amazing and helpful principles. Without them, the author recognizes that the world may not look the way it does. In the following sections, we will present the principles found in the ACI Code and other mechanics approaches as they pertain to this work.

2.4.1 – Shear and Moment Calculations with ACI

The ACI is broken up into numerous chapters and appendices, each pertaining to a certain design criterion. Chapter 11 of ACI318 discusses the calculations for shear and torsion. In accordance with this present work, our interest is in the calculation of shear. According to ACI318,

$$\phi V_n \geq V_u, \text{ where} \quad \textbf{(2.26)}$$

V_u is the factored shear force, V_n is the nominal shear strength, and ϕ is a reduction safety factor.

The nominal shear strength, V_n, is the summation of the concrete's shear strength and the steel's shear strength:

$$V_n = V_s + V_c, \text{ where} \quad \textbf{(2.27)}$$

$$V_c = 2\lambda\sqrt{f'_c}b_w d \text{ and} \quad \textbf{(2.28)}$$

$$V_s = \frac{A_v f_{yt} d}{s}, \text{ where} \quad \textbf{(2.29)}$$

A_v is the area of shear reinforcement with spacing s, f_{yt} is the tensile yield strength of the steel, and d is the depth of the steel shear reinforcement, measured from the top of the member. Using these equations, one can predict the shear strength of a reinforced concrete member with shear reinforcement.

Further, the nominal bending strength, M_n, allowed in a reinforced concrete member is:

$$M_n = C_s(d - d') + C_c\left(d - \frac{a}{2}\right), \text{ where} \quad \textbf{(2.30)}$$

C_s is the moment causing force in both the tensile and compressive steel, C_c is the moment causing force in the concrete, d is the depth of the tensile steel measured from the top of the member, d' is the depth of the compressive steel measured from the top of

the member, and a is the depth of the compression block. The moment causing forces in the steel and concrete are determined by:

$$C_s = A'_s\left(f'_s - 0.85f'_c\right), \text{ and} \quad \textbf{(2.31)}$$

$$C_c = 0.85f'_c\beta_1 cb, \text{ where} \quad \textbf{(2.32)}$$

A'_s is the area of the compressive steel, f'_s is the yield strength of the compressive steel, f'_c is the compressive strength of the concrete, β_1 is a constant multiplier, c is the depth of the Whitney stress block, and b is the cross-sectional width of the member. Using Equation 2.31 and 2.32 in Equation 2.30, the nominal moment is found. To verify Equation 2.31 and 2.32, the concept of equilibrium can be observed. In other words, the compression the member feels must be equal to the tension:

$$C_c + C_s = T, \text{ where} \quad \textbf{(2.33)}$$

$$T = A_s f_y \text{ and} \quad \textbf{(2.34)}$$

A_s is the area of the tensile steel and f_y is the yield strength of the tensile steel. Therefore, the tension and resulting compression force are calculated and they should be the same.

The nominal bending strength is important because, like shear:

$$\phi M_n \geq M_u. \quad \textbf{(2.35)}$$

Although these approaches are simple and used in the most basic of structures, their use in more complex, less researched members are questionable. For example, very large beams may behave in ways that the ACI code does not account for. In fact, ACI's equations come from the testing of hundreds of small beams. And even though their equations produce results that are most often overly conservative, how can we trust their use in members that have no test data, such as a very large beam? These and other questions, we wish to address later in this work.

2.5 –Summary

We have outlined in this chapter many of the approaches that engineers use in everyday design and analysis of reinforced concrete members. Silling, Gerstle, and others have proposed and developed a new solid mechanics model called peridynamics, which strays from the traditional approaches to problem solving while implementing new fundamentals through modern technology and nonlinear mechanics. Although peridynamics may seem way too far ‘out there’, once understood, it may offer a useful tool to solve problems in reinforced concrete. Peridynamics offers the engineer the ability to predict the strength of reinforced concrete sturctures (and other types in the near future) including crack propagation. The engineer is charged with the task of protecting society’s safety and well-being. What if that can be better accomplished using nontraditional approaches like peridynamics?

Chapter 3

Revisiting the Bond-Slip Model

This chapter's objectives are to:

- Explore bond-slip and its application in reinforced concrete
- Discuss Gerstle's work
- Investigate a linear elastic 'tension-pull' model
- Describe a new SPLM bond-slip model
- Demonstrate SPLM tension-pull models with the new bond-slip model
- Explain and discuss the SPLM 'tension-pull' model

Bond-slip has become a model of interest for both computational engineers and practicing engineers. Bond-slip is important to understand because it controls the behavior of composite materials. A bond-slip model is necessary to predict the strength of reinforced concrete members. In the following section, we will explain bond-slip and its application in reinforced concrete members.

3.1 – The Bond-Slip Model and its Application

Bond-slip became a focus of study as engineers began to use composite structures in design. Engineers began to understand that the use of two or more materials in a structural member would increase the strength of the member. One must understand the idea of a bond before we can discuss bond-slip.

3.1.1 – Bond

It is essential for steel and concrete to deform compatibly in reinforced concrete. Ideally, the same deformations that take place in the concrete also happen in the steel. In order for the member to act compositely, there must be adequate load transfer between the steel and concrete as force is applied to the member.

The bond and consequently its strength are characterized by several factors including constitutive material parameters, mechanical properties, geometry, and load history of the materials. Another bond characteristic is the 'ribs' present in modern steel reinforcement. Figure 3.1 shows a sketch of a deformed rebar and surrounding concrete.

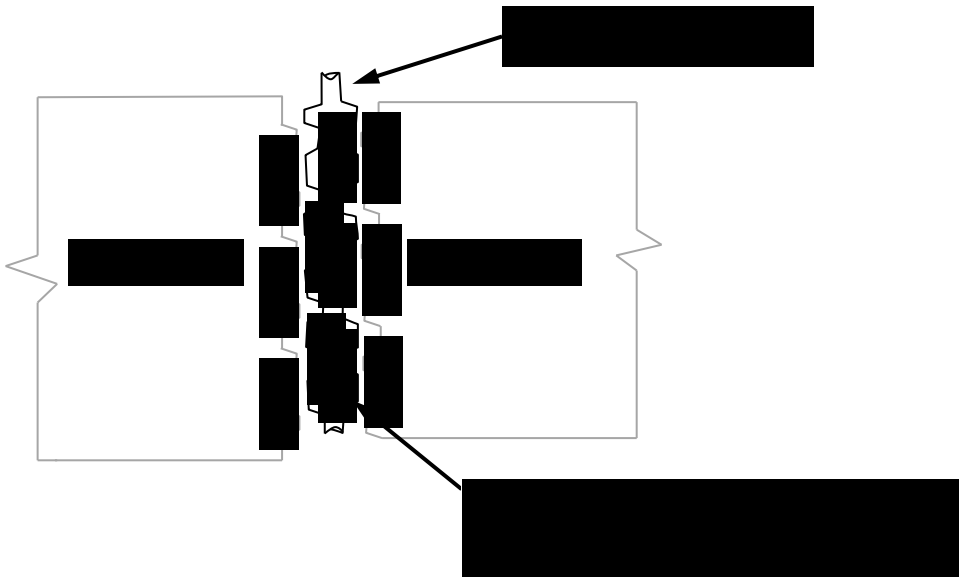

Figure 3.1 – Concrete-to-steel bond

The 'ribs' in the steel strengthen the bond between the steel and concrete and act as grippers, aiding in composite action. If there is inadequate grip between the steel and the concrete, the member could experience various failure modes, including rebar pull-out.

3.1.2 – Bond-Slip

With this discussion of bond, we can define and identify bond-slip. Bond-slip, as the name implies, occurs when the steel slips with respect to the concrete. The slip can result from an inadequate amount of reinforcement, insufficient ribs, or applied grease, which is done intentionally in some prestressed concrete beams, for example. There are many bond-slip models [17, 18, 19]; it seems that this phenomenon is still in development and engineers are still trying to understand it.

3.2 – Gerstle's Developments in Bond-Slip

In his master's thesis, Gerstle [14] investigated bond-slip using linear elastic models and finite element codes. He modeled a six-inch diameter, 72-inch long concrete cylinder, which had one #8 rebar surrounded by the concrete (originally tested by Broms and Raab [16]). Figure 3.2 shows the test cylinder Gerstle used in his analysis.

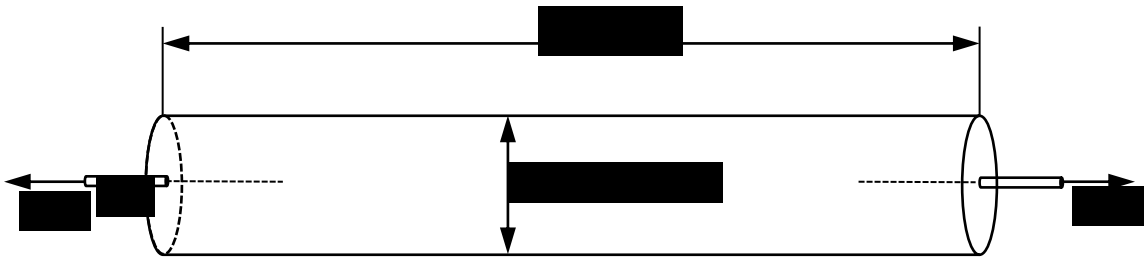

Figure 3.2 – Tension-Pull specimen analyzed by Gerstle (after Gerstle [14])

Gerstle investigated the cracking pattern and bond-slip characteristics of the cylinder using FEFAP, a finite element code. The protruding steel was pulled from both ends, as shown in Figure 3.2.

Gerstle and many others [14, 15, 16] investigated the tension-pull specimen because it represents a number of situations including the situation at the bottom of a reinforced concrete beam. This simplified model can help us understand the bond between different materials and bond-slip that could occur in larger, more applicable circumstances.

In Gerstle's thesis, there are several failure modes he ignores. For example, he used an axisymmetric option in FEFAP which does not model longitudinal splitting cracks. Therefore, this specific mode of softening was ignored and interpretation of his results needs to be considered accordingly. He also ignored other softening behaviors such as concrete crushing, which occurs on the compression side of the ribs. He justifies his ignorance of concrete crushing using [20], where Houde and Mirza show that no crushing occurs on the compression side of the ribs, rendering both modes of crushing and compressive stresses irrelevant to his study on the tension-pull specimen.
Gerstle concluded the tension-pull tests saying,

> "As load is applied to the specimen, the first secondary crack forms at a very low load, at the location where the rebar exits the concrete…Each secondary crack was seen to form at the location where a rib bore on the concrete…As the load increased, secondary cracks propagated, and at the same time additional secondary cracks nucleated at ribs further and further away from the end of the specimen…At a certain load, the tensile stress in the concrete at the midlength of the specimen, which was constant throughout the concrete cross section as long as the specimen was long enough, reached the tensile strength of the concrete…At this point, a crack formed through the entire concrete cross section. Due to

symmetry, the crack could not slant in either direction, but instead formed a flat surface. This type of crack is called a primary crack." [14, pp. 79]

Figure 3.3 shows a sketch of Gerstle's idea about the mechanism of "bond-slip".

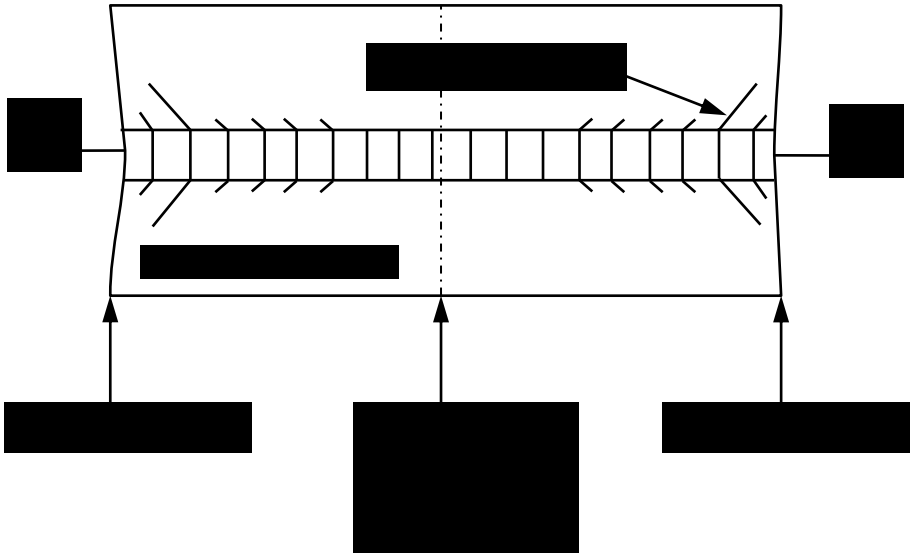

Figure 3.3 – Gerstle's 12 in tension-pull specimen results (deflected shape) (redrawn from [14] pp. 92)

Note the direction of the secondary cracks as opposed to the primary cracks. The secondary cracks are oriented at a near 45 degree angle, while the primary cracks are vertical in their propagation direction. Also, these secondary cracks propagate radially outward from the steel into the concrete.

Using the results of the tests he performed, Gerstle developed a load vs. displacement graph for the tension-pull specimen shown in Figure 3.4. We will compare our load vs. displacement graph to Gerstle's later in this chapter.

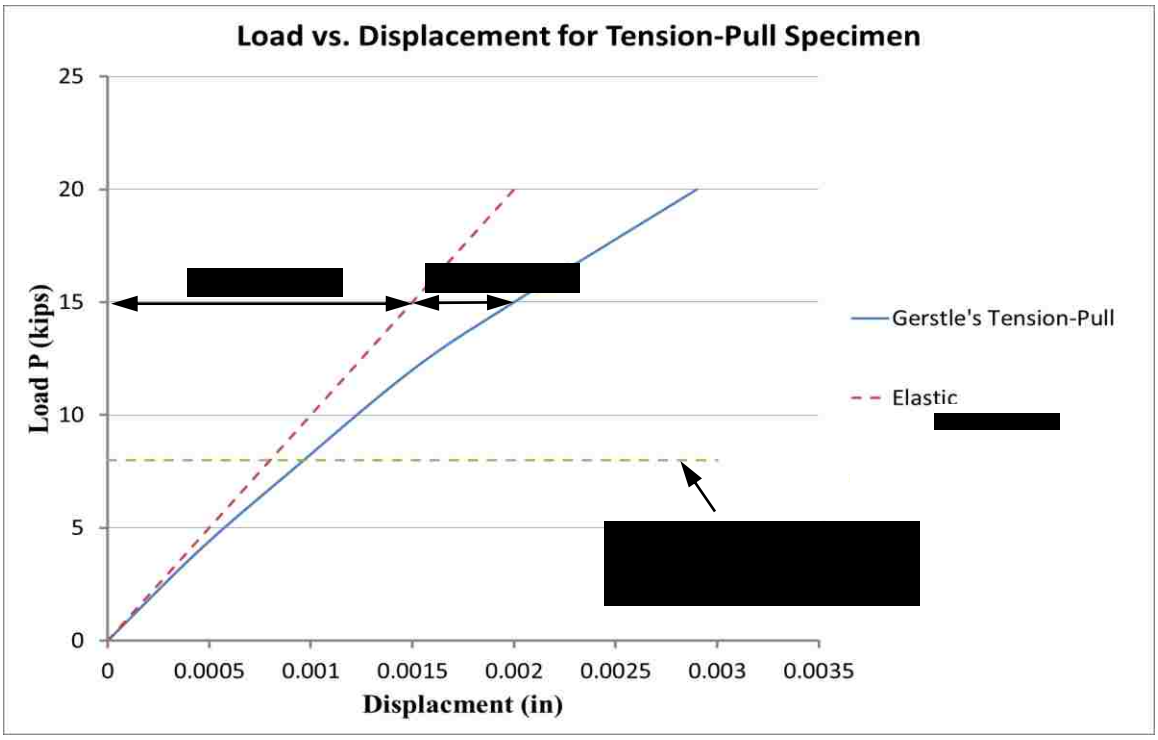

Figure 3.4 – Load vs. displacement graph for Gerstle's tension-pull specimen (redrawn using Fig. 5.15 from [14] pp. 103)

In the graph in Figure 3.4, the end displacement for half of a 12-inch specimen, or 6-inch segment (one for either side of the 12-inch specimen) can be divided into two portions: an elastic portion, represented by Δ elastic, and the inelastic or bond-slip portion, represented by Δ slip. It was, therefore, concluded in Gerstle's thesis that steady "tension softening" transpires as the load is transmitted across the steel-concrete interface. Essentially, wherever these bond-slip displacements occur, there is a softening of the material which is independent of the primary crack spacing and dependent on the properties of the reinforcing bar, on the material properties of the concrete, and on the force in the bar.

Gerstle, furthermore, compared his results to Goto's [21] tests. Goto performed laboratory experiments on similar tension-pull specimens, where they inserted ink into

the specimens and split the cylinder longitudinally in order to point out crack patterns. The cracking pattern observed by Goto can be seen in Figure 3.5.

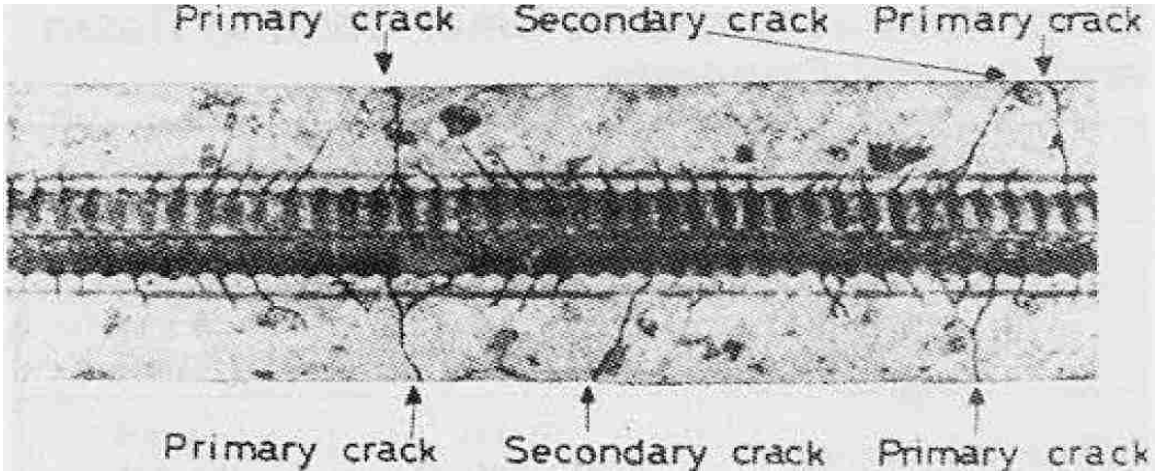

Figure 3.5 – Goto's tension-pull specimen injected with ink and split longitudinally (from [21])

Later in his career, Gerstle wrote an article with Ingraffea [22], where they investigated tension-pull specimens differently than had ever been done before. Gerstle and Ingraffea conducted laboratory tests on a tension-pull specimen made of Evercoat Clear Casting Resin with one 0.25-inch diameter steel reinforcing bar. Although there are differences between the constitutive characteristics of concrete and clear casting resin, they decided to use this resin because it is a clear material, resulting in an obvious cracking pattern seen with the naked eye without having to split the sample longitudinally as Goto had done. Gerstle and Ingraffea's initial and end results can be seen in Figure 3.6 and 3.7.

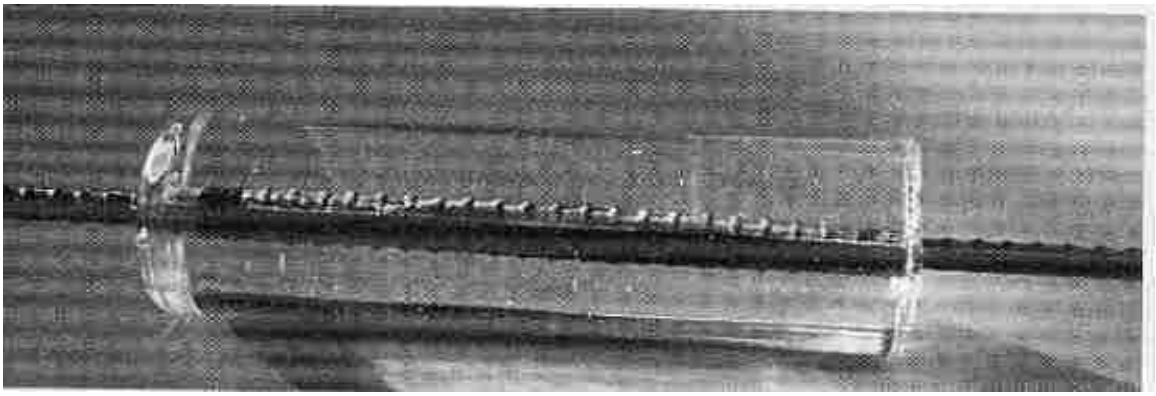

Figure 3.6 – Initial clear resin tension-pull specimen (from [22])

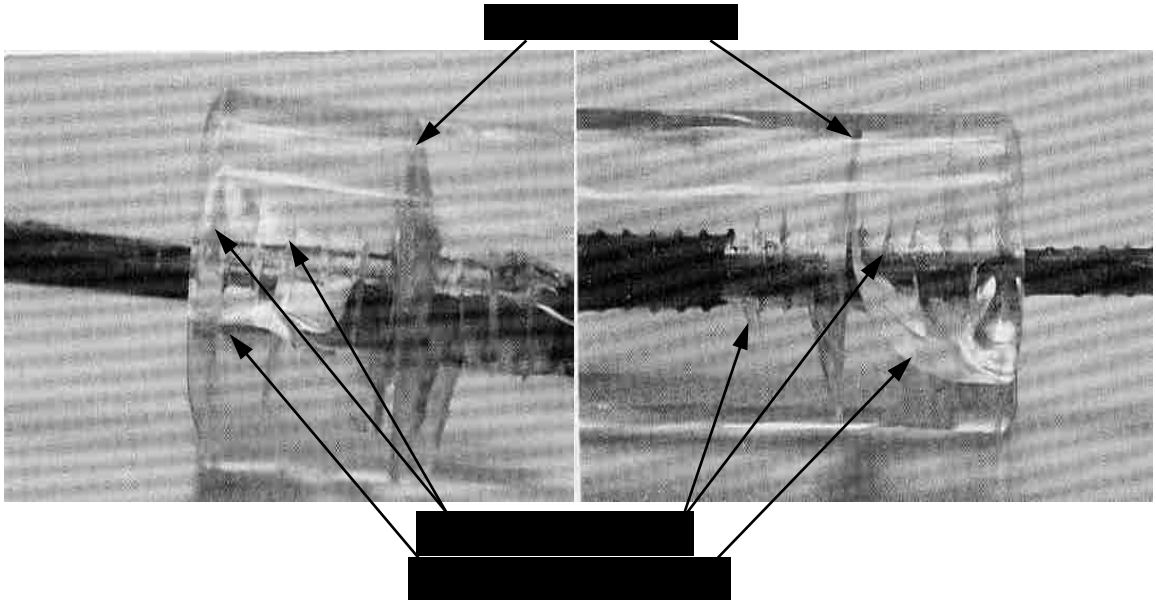

Figure 3.7 – Clear resin tension-pull specimen results (from [22])

The primary, secondary, and longitudinal cracks can be seen clearly starting from the outside, where the steel enters the resin, and developing towards the middle of the specimen as the force is transmitted further and further into the specimen. We note the very irregular crack pattern, which is random at best. Gerstle and Ingraffea concluded with three observations. First, they noted that complex, three-dimensional cracking configurations are found to accompany bond-slip. In a side note, they state that the

complexity of the cracking is even greater than that seen in Goto's experiments. Second, they propose this resin material can be used, in the future, to approximately simulate concrete structures. Finally, they conclude their investigation strongly suggests that bond-slip is not so much governed by the interface properties between the steel and the concrete, but is more controlled by the fracture behavior of the concrete.

Previous research shows bond-slip is still a highly debated issue among engineers. Its complex nature has been examined by many engineers. Its multifaceted nature stems from the nonlinear behavior that occurs at the meso level. In the SPLM, a different bond-slip model, which takes into account the nonlinear characteristics at the meso level, is discussed in the next section.

3.2.1 – Gerstle's Bond-Slip Model for the SPLM

In his recent book, Gerstle [2] proposes a basic bond-slip model intended to be used in a wide variety of problems using the advantages peridynamics presents by using force states and stretches. There are two properties that affect his model. First, a stiffness is assumed between a steel particle and a neighboring concrete particle. Second, Gerstle defines an interface horizon beyond which steel and concrete particles do not interact. Because the steel and concrete particles lattices could have different spacings, this distance is expressed as a multiple of the maximum lattice spacing.

3.2.2 – Steel-Concrete Stiffness

Gerstle denotes K_{bond} as the bond stiffness between a steel and concrete particle. It is defined as:

$$K_{bond} = (1.0 - damage) * K_{conc} * m_{steel}/m_{conc}, \text{ where} \quad \textbf{(3.1)}$$

K_{conc} is the stiffness between concrete particles, $damage$ is the amount of damage the concrete particle experiences at that time step (either partially damaged with some value less than 1.0 or fully damaged with a value of 1.0), m_{steel} is the mass of the steel particle, and m_{conc} is the mass of a concrete particle.

Furthermore, the force between the particles is directed as a central force between the connected particles. The force equation between a steel and concrete particle is:

$$F_i(iDir) = dc\ (iDir) * (K_{bond} * str + linkForceDamp), \text{ where} \quad \textbf{(3.2)}$$

F_i is the force component in direction i, dc is a direction cosine vector in which the force acts, K_{bond} is bond stiffness, str is the stretch between two particles, and $linkForceDamp$ is the damping factor between two particles. Essentially, the force is a function of the stretch, damping coefficient, and material definition.

3.2.3 – The Interface Horizon between Steel and Concrete

The interface horizon of steel particles is the second characteristic that affects Gerstle's bond-slip model. Principally, what is the radial distance in which a steel particle would directly affect a concrete particle? 'Directly' implies there is an initial bond in the undeformed, reference configuration between a steel particle and a concrete particle.

If the distance between a steel and a concrete particle is greater than a tolerance value which is used to ensure stability but is less than the bond material horizon in the material body, then a link (or bond) between the steel and concrete is created. Initially, Gerstle decided that the steel particles, representing rebar, would only interact with concrete particles located within the concrete lattice spacing as seen in Figure 3.8. The

question is, do the steel particles directly affect concrete particles outside the concrete lattice spacing, say two times the maximum lattice spacing? This question, along with the value of K_{bond} is discussed in the next section.

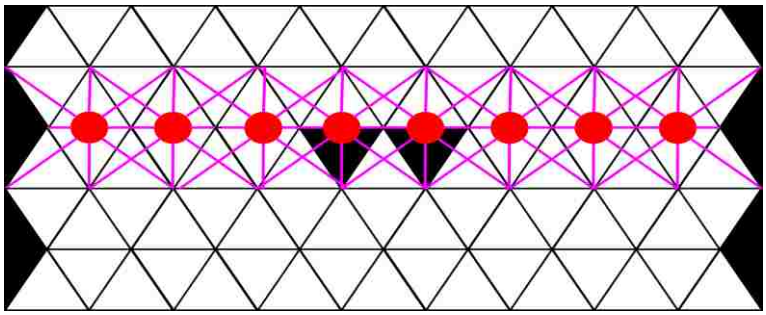

Figure 3.8 – Typical lattice showing bonds (magenta) between steel (red) and concrete (black) particles within the maximum lattice spacing

3.3 – New Bond-Slip Model

In this section we modify Gerstle's bond-slip model and later run several SPLM models with the intention of verifying the new bond-slip model. First, to show the differences between our model and current modeling software, we present a finite element analysis using SAP2000 of the tension-pull specimen.

3.3.1 – Linear Elastic Tension-Pull Specimen

Figure 3.9 shows the initial SAP2000 tension-pull specimen. The specimen is 20 inches long, 6 inches in height, made of concrete, and has one #8 rebar represented by frame elements surrounded by plane stress concrete. The specimen was pulled with a force of 20 kips from both ends.

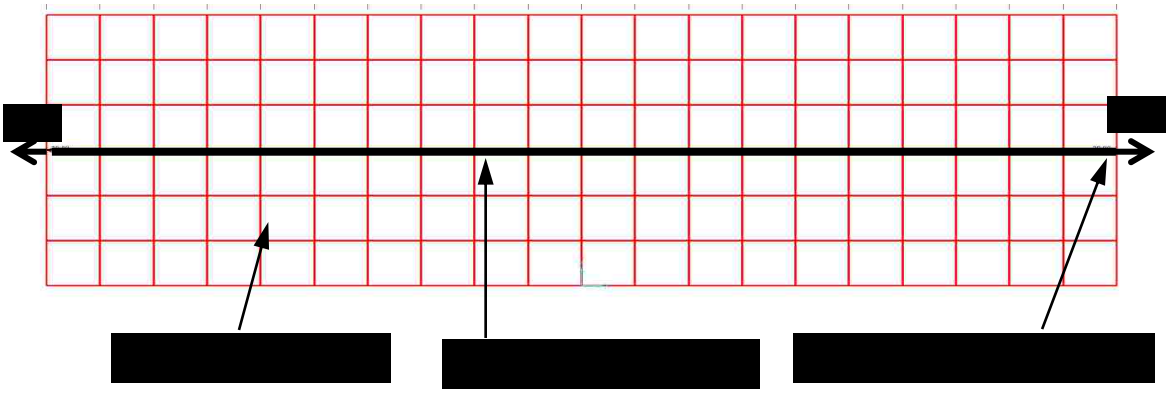

Figure 3.9 – SAP tension-pull specimen

Figure 3.10 shows the result of the SAP analysis.

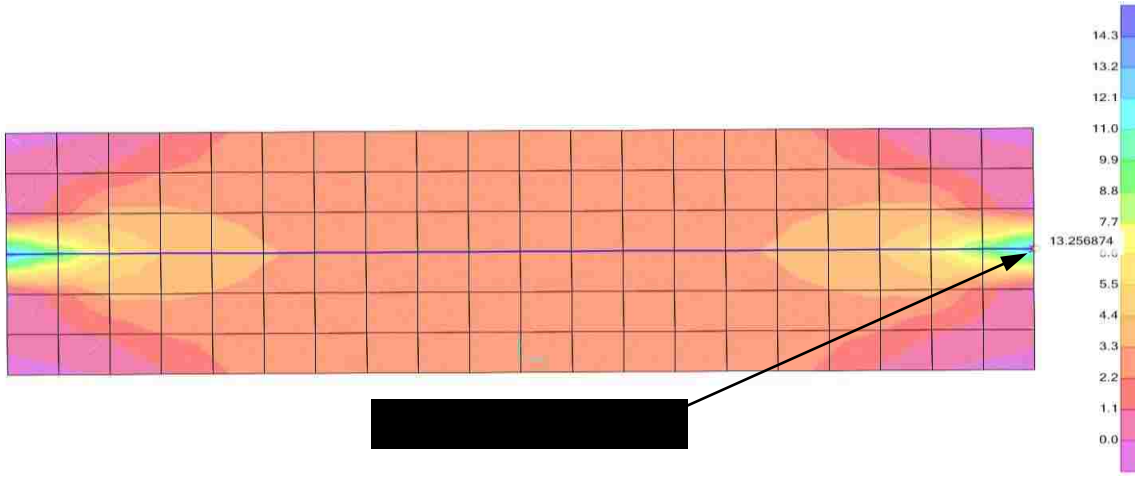

Figure 3.10 – SAP results of tension-pull specimen

Notice the stress concentration where the tensile "point load" is applied. It can be shown that if the mesh is refined around this point, the stress would increase without bound. Our intention of including the SAP analysis is to show that linear FEM models do not show the strength of the structure, rather they only display what would happen in terms of stress flow if the material remained linear elastic, which is approximate, and leaves the engineer to determine the strength of member.

Nonlinear finite element models do exist but these models are so complex their application in practical engineering circumstances is limited. These codes, moreover,

leave the user in the dark because even if the quantitative results are understood and interpreted correctly, there is still question to as what the code is actually doing. In linear and nonlinear finite element codes, the engineer is also required to perform mesh convergence studies to reach a solution, which is still an approximate solution in the end. We recognize the significance of such models and their importance, but what if there was a model that tells the engineer the strength of the member without much interpretation? Would it render models like this obsolete?

3.3.2 – Initial SPLM Tension-Pull Models

Our interest in the SPLM bond-slip and the motivation for this chapter was a result of a desire to use the model in a competition. The competition, which is discussed more formally in Chapter 6, was to see who, out of universities and commercial industries throughout the world, could most accurately predict the shear strength of a very large reinforced concrete beam. We submitted a prediction using the SPLM for the shear strength of the beam using Gerstle's original bond-slip model. The results surprised us, as the actual strength of the beam was significantly lower than the SPLM predicted or what ACI predicted. The SPLM predicted a much stronger beam than what laboratory results showed; therefore, we suspected a flaw in our bond-slip model.

We simplified our model of this large beam down to the tension-pull specimen. This would allow us to explore our bond-slip model without focusing on the huge beam and its computational demand. We started with the bond-slip model described in Sections 3.2.1-3.2.3, only altering the interface horizon of the steel particles, and experimented on the tension-pull specimen in Figure 3.2. The outcome of these experiments revealed that

there was a problem with the bond-slip, which we suspected, as the final crack pattern was unrealistic.

We concluded in these initial experiments the interface horizon plays a vital role in the crack pattern of the analysis. Continuing in similar tests, we changed the bond stiffness and the interface horizon, but continued to get unrealistic crack patterns. Thus, the question needed to be asked: can the SPLM model bond-slip? Maybe it's a phenomenon too sophisticated to predict using the SPLM?

3.3.4 – Our Change in K_{bond}

Gerstle originally defined K_{bond} to be a function of the damage of a concrete-concrete bond, but at which scale was Gerstle considering damage to dominate in the bond stiffness; the micro, meso, or macro? Thus, we redefined K_{bond} to equal:

$$K_{bond} = \alpha * K_{conc} * m_{Min}/m_{conc}, \text{ where} \quad \textbf{(3.3)}$$

K_{conc} is the concrete stiffness, m_{Min} is the minimum of the mass of the steel and the concrete particles, m_{conc} is the mass of a concrete particle, and α is a parameter that defines the stiffness of the bond. Equation 3.3 states that the stiffness between the steel and concrete is a function of the stiffness between two concrete particles, as the stiffness between a steel and concrete particle would not be so much different than the stiffness between two concrete particles, multiplied by the ratio of the masses of the concrete and the smallest particle mass. The mass ratio ensures the time period of the steel-concrete mode of vibration is sufficiently long that dynamic instability is avoided in the time integration procedure.

α will ultimately determine the numerical stability of the model. If this value is not great enough, the model treats the links between the steel and concrete like flexible rubber bands. A rubber band-like link between the steel and concrete particles would allow too much bond-slip. In other words, the concrete would not deform together with the steel and the rebar would pull out from the concrete without affecting the surrounding concrete. However, if α is too great, the model would become dynamically unstable. With unstable behavior, essentially, we observed the steel particles vibrating in their initial position until the concrete surrounding those particles became fully damaged, allowing the steel to then separate from the concrete. The SPLM's bond-slip model is essentially established determining α, but how? In the next section, we present models run with varying α to determine the bounds and optimal value of the constant.

3.4 – SPLM Tension-Pull Tests with the New Bond-Slip Model

3.4.1 – Establishing the Bounds of α

Figures 3.11-13 show the progression of a very stiff tension-pull specimen. The model was run with the following parameters:

- lattice spacing (concrete, rebar) = 0.0254 m (1 in)
- length = 0.50 m (20 in)
- height = 0.1524 m (6 in)
- α = 110.0
- interface horizon = 1.5 * maximum lattice spacing
- applied displacement to ends of rebar = 0.0012 m (0.05 in)
- diameter of rebar = 1 in

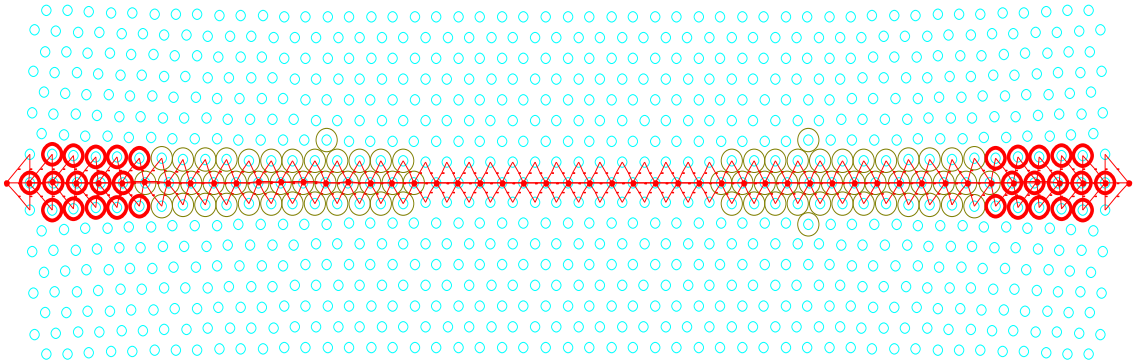

Figure 3.11 – SPLM tension-pull test at 20% total applied strain, deformation magnified by 100

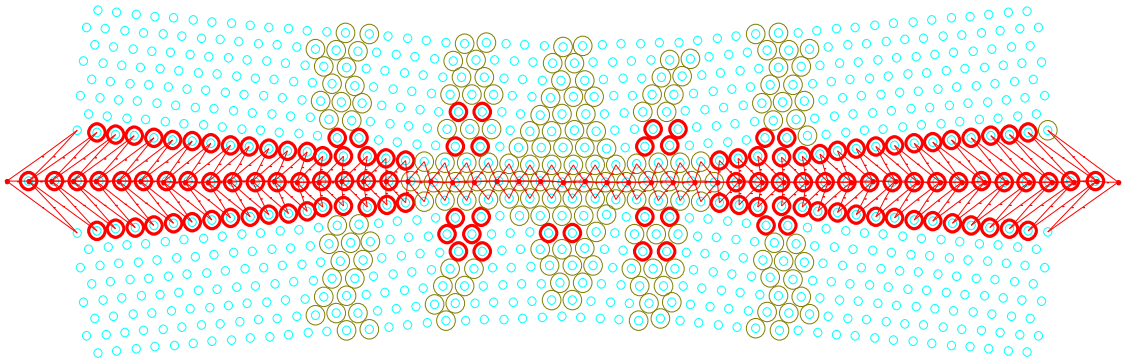

Figure 3.12 – SPLM tension-pull test at 50% total applied strain, deformation magnified by 100

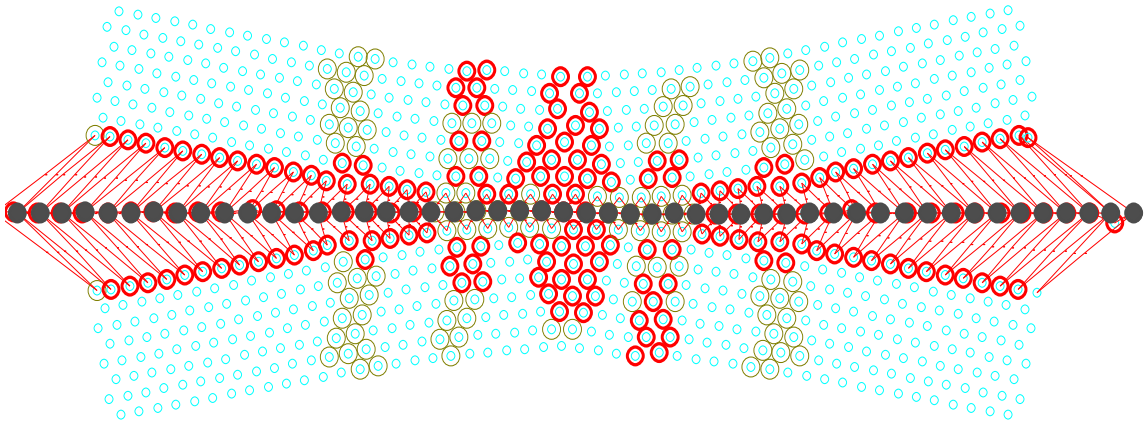

Figure 3.13 – SPLM tension-pull specimen test at 100% total applied strain, deformation magnified by 100

In these figures blue circles represent concrete particles, yellow particles represent partially damaged concrete particles, hollow red particles represent totally damaged concrete particles, solid red particles represent steel particles, solid grey particles represent yielded steel particles, and red lines represent bonds between particles. We can

categorize the model above as very stiff for several reasons. First, $\alpha = 110$ when calculating K_{bond}, which was the highest value we could use before the SPLM calculated the force between the steel and concrete particles jumping to infinity, seen in Figure 3.14 with $\alpha = 115$.

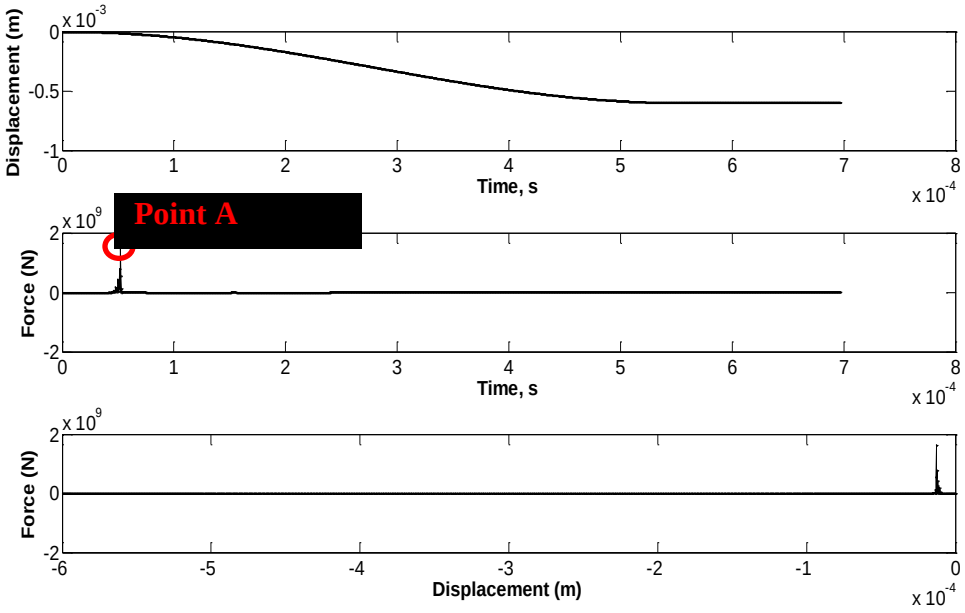

Figure 3.14 – SPLM results of tension-pull specimen with $\alpha = 115$

Point A in Figure 3.14 shows that force in the steel jumps to infinity suddenly when $\alpha = 115$, demonstrating dynamic instability of the bond. Therefore, we have established our upper bound for α as 110. To determine the lower bound we set α close to 0 where we expect the bond between the steel and concrete to become less composite in action. Figures 3.15-17 show the progression of a simulation displaying a lack of composite action. The models were run with the following parameters:

- lattice spacing (concrete, rebar) = 0.0254 m (1 in)
- length = 0.50 m (20 in)
- height = 0.1524 m (6 in)

- $\alpha = 0.001$
- interface horizon = 1.5 * maximum lattice spacings
- applied displacement to ends of rebar = 0.0012 m (0.05 in)
- diameter of rebar = 1 in

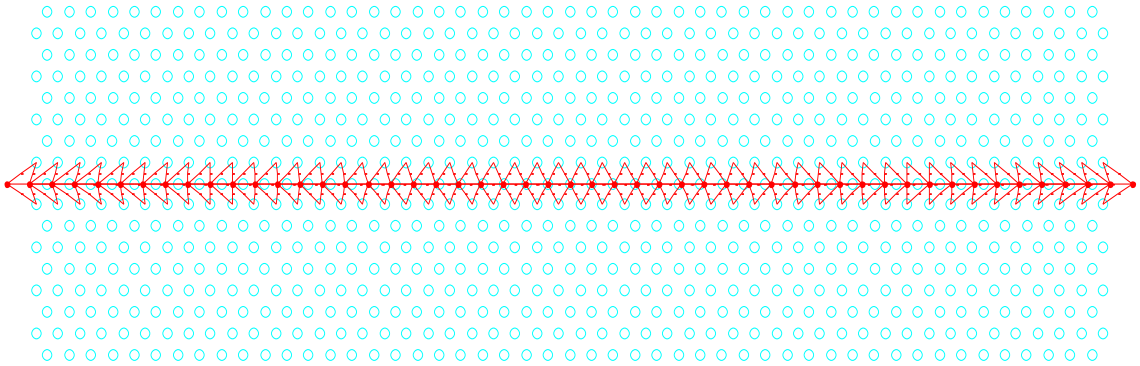

Figure 3.15 – SPLM tension-pull test at 20% total applied strain, deformation magnified by 100

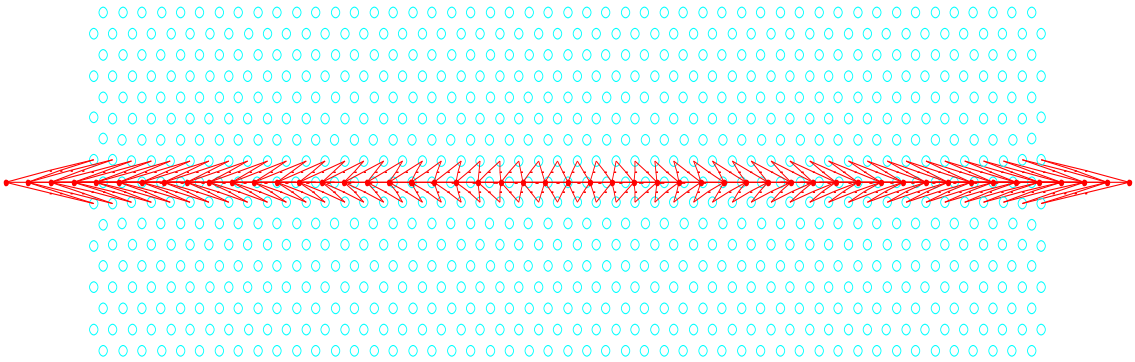

Figure 3.16 – SPLM tension-pull test at 50% total applied strain, deformation magnified by 100

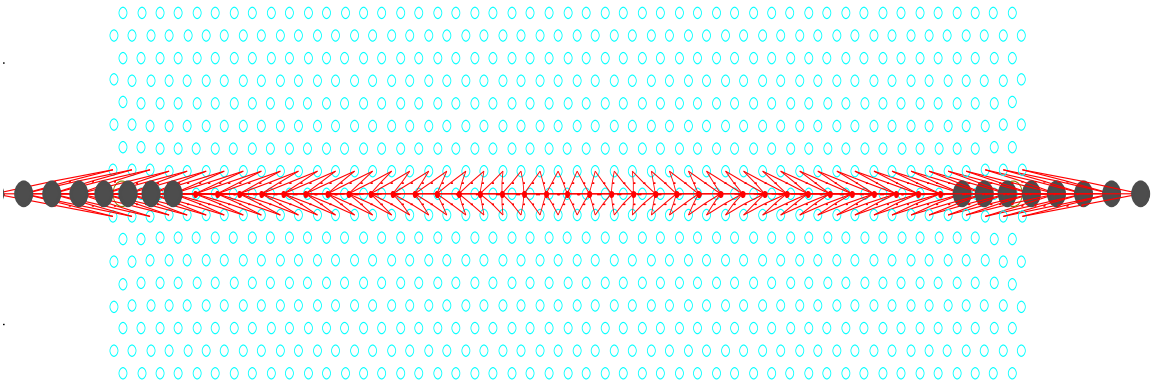

Figure 3.17 – SPLM tension-pull specimen test at 100% total applied strain, deformation magnified by 100

Figures 3.15 - 3.17 above verify that our model is almost non-composite with $\alpha = 0.001$. The lack of composite action is exemplified as the steel displaces, it has no effect on the surrounding concrete. As a result, we establish the lower limit of α. We hypothesize that there must be a value of α that models 'realistic' behavior. Essentially, we want to establish as stiff a bond between the steel and concrete as possible while avoiding unstable dynamic behavior as seen in Figure 3.14. The next section presents this model and discusses the behavior of this model.

3.4.2 – The Final Bond-Slip Model and Discussion

Our goal is to find a value that will cause the bond model to respond as stiffly as possible without causing a stability issue. Figures 3.18-20 show the progression of a reasonable model. The relative parameters for the mode are:

- lattice spacing (concrete, rebar) = 0.0254 m (1 in)
- length = 0.50 m (20 in)
- height = 0.1524 m (6 in)
- $\alpha = 0.10$
- interface horizon = 1.5 * maximum lattice spacings
- applied displacement to rebar ends = 0.0012 m (0.05 in)
- diameter of rebar = 1 in

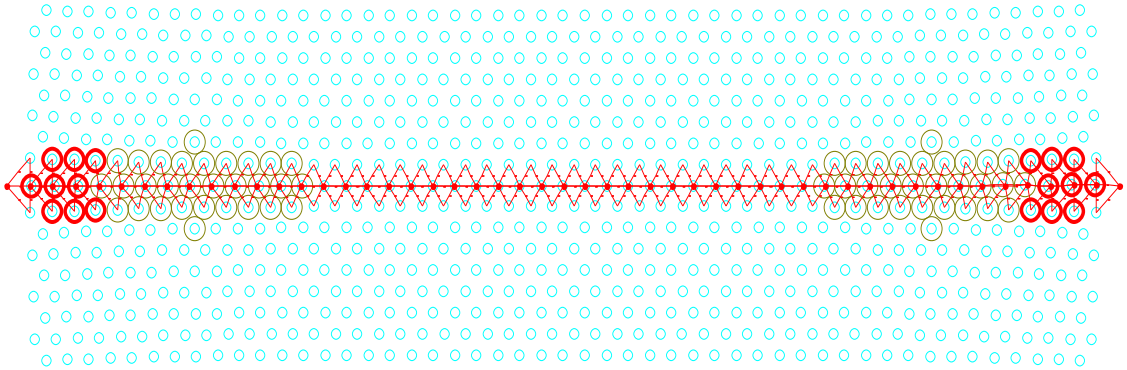

Figure 3.18 – SPLM tension-pull test at 20% total applied strain, deformation magnified by 100

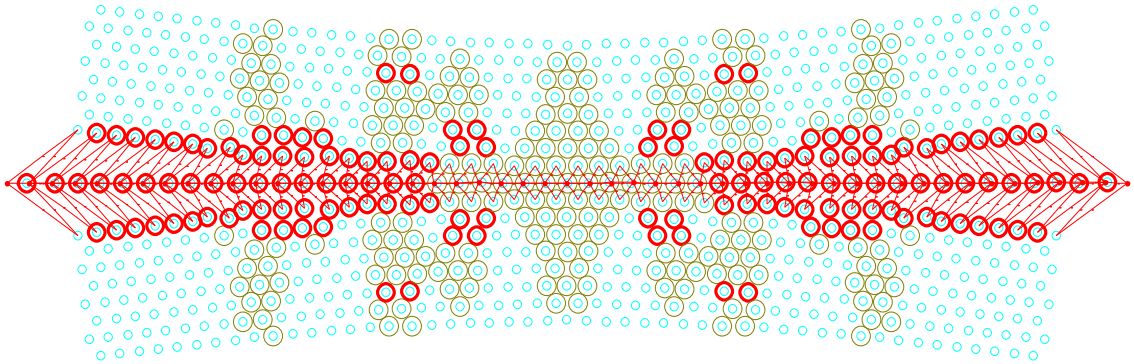

Figure 3.19 – SPLM tension-pull Test at 50% total applied strain, deformation magnified by 100

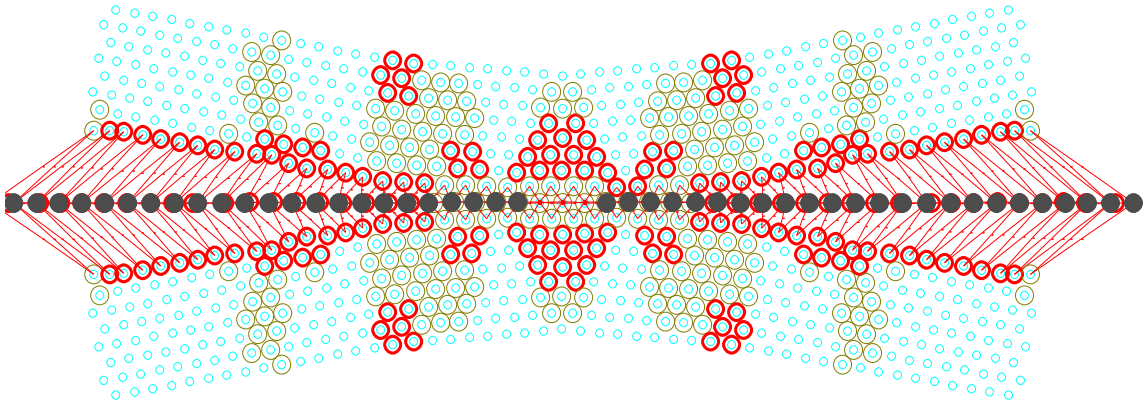

Figure 3.20 – SPLM tension-pull specimen test at 100% total applied strain, deformation magnified by 100

We believe this to be a reasonable model for several reasons. First, we are trying to model bond-slip, which is a three-dimensional phenomenon, using a two-dimensional model. We did not initially consider the differences between a two-dimensional model and a three-dimensional model in terms of crack origination and propagation. We think the models would be similar in some ways and different in other ways. The main difference is the formation of radial secondary cracks Gerstle and Goto observed in their experiments. These cracks are the result of a cone-shaped stress field in the concrete originating at the point of highest stress, where the steel exits the concrete, as shown in Figure 3.21.

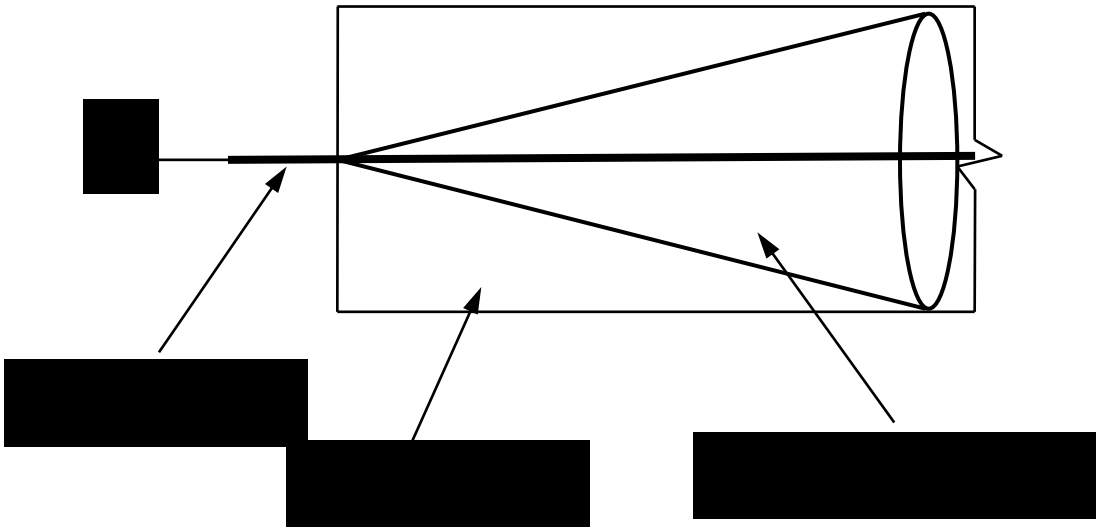

Figure 3.21 – Cone-shaped stress field travelling through tension-pull specimen

Because this shape only forms in three dimensions, the response is going to be different than what we would expect to see in two dimensions.

In our two-dimensional model, however, we would not expect to replicate this response. Our 2D model is visualized better by imagining two concrete bricks glued together with steel rebar between them. The expected result is a 'peel-back' response, where the concrete peels away from the steel as a tensile force is applied to each end of the specimen. This type of action is observed in Figures 3.18-20. Notice that the concrete "unzips" from the steel particles starting where the steel exits the concrete propagating towards the middle of the specimen as the displacement increases. The unzipping action continues until the force state reaches a point to form symmetrical primary cracks on both sides of the specimen. We note that none of the figures show concrete-concrete bonds, which do cross over the rebar.

The lack of radial, secondary cracks is also explained in the method of analysis. That is, our two-dimensional model is run in a plane stress case. We call it a plane stress

case, but the SPLM calculates force states and stretches as opposed to stress and strain in a 2D plane. The lack of calculating the force states and stretches out of plane definitely affect the crack pattern. To see further explanation of out of plane stresses in the SPLM, see [2] and/or [3].

The results shown in Figures 3.18-20 also display reasonable results in the fact that we observe all the steel particles yielding. We applied enough displacement, 0.0012 meters (0.05 inches), expecting to see the steel yield. Therefore, our model appears to react as realistically as we can expect for a two-dimensional model.

Finally, we did not change the interface horizon from 1.5*maximum lattice spacings in our trials. We focused more of our attention on the stiffness in the bond, as we speculated this would be the controlling factor, but realize that the interface horizon distance also plays a role in the results. We suggest future research in determining the optimal interface horizon distance. To further verify our model, we decided to model the tension-pull specimen in three-dimensions, discussed in the next section.

3.5 – 3D SPLM Tension-Pull Model

We analyzed the same tension-pull specimen in the previous section in terms of geometry and material parameters, but instead of a plane stress case the cylindrical specimen was analyzed in three-dimensions, as shown in Figure 3.22.

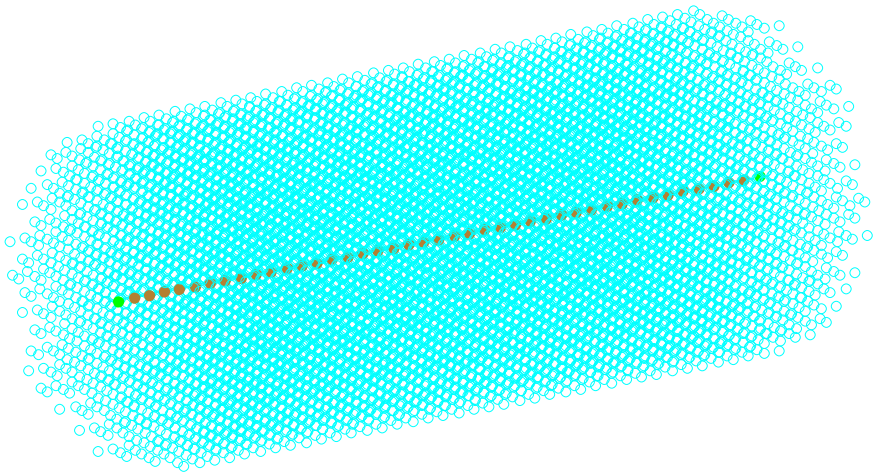

Figure 3.22 – 3D tension-pull specimen

To simplify visualization of the results, we considered a slice of the cylinder three particles deep to observe what was occurring in the cylinder without visual chaos. The results are shown in Figures 3.23-25.

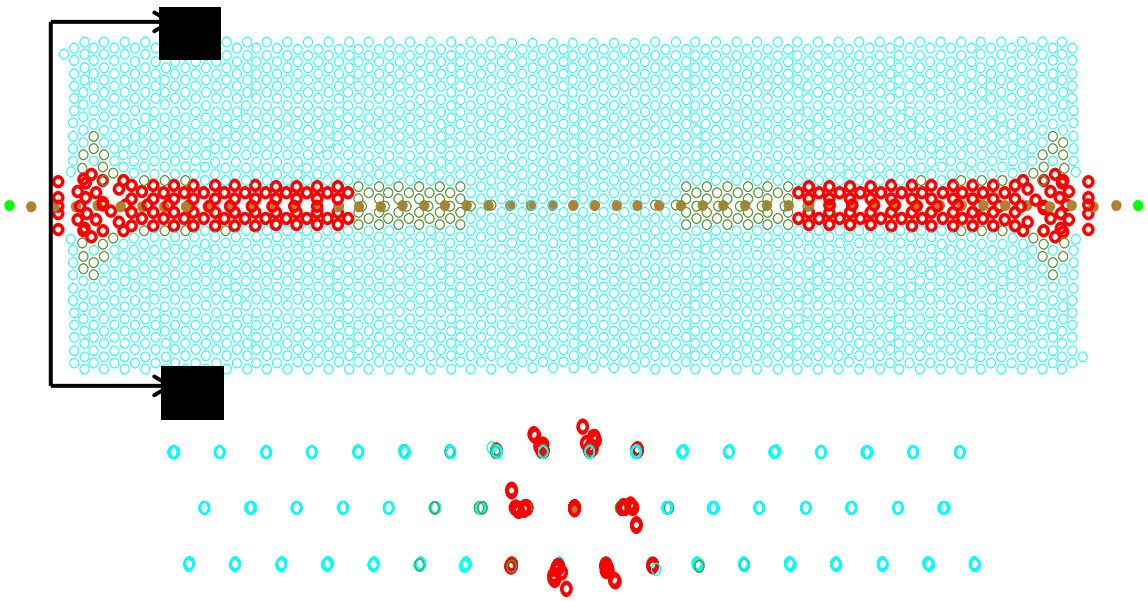

Figure 3.23 – 3D SPLM tension-pull specimen at 20% total applied strain; diametric view (top), cross-sectional view (A-A) (bottom)

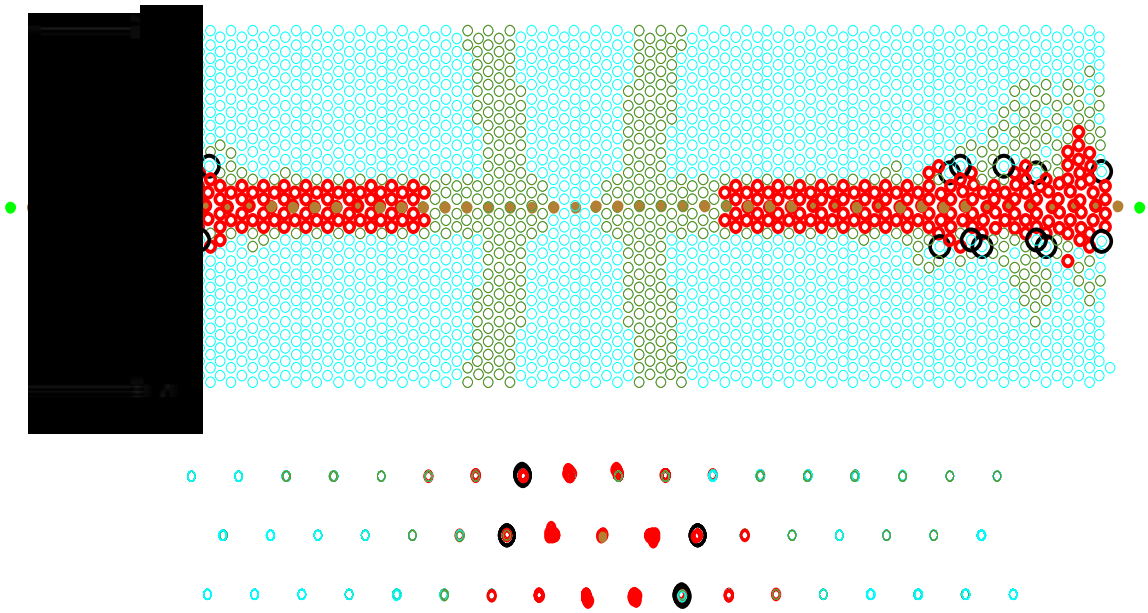

Figure 3.24 – 3D SPLM tension-pull specimen at 30% total applied strain; diametric view (top), cross-sectional view (bottom)

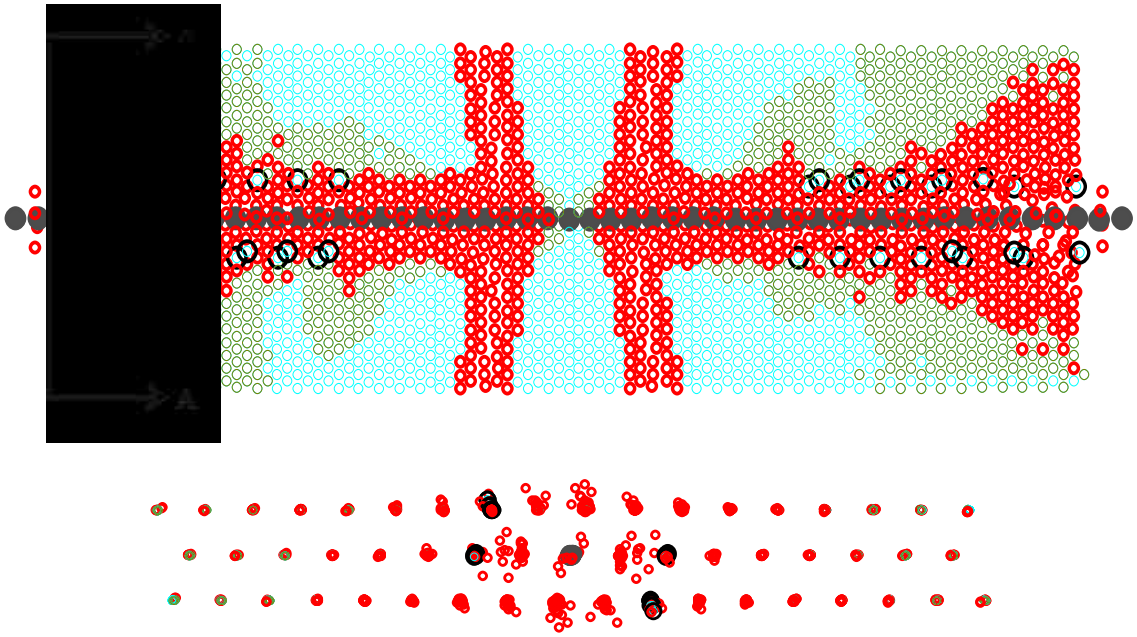

Figure 3.25 – 3D SPLM tension-pull specimen at 100% total applied strain; diametric view (top), cross-sectional view (bottom)

We saw in our two-dimensional model presented in the previous section a lack of radial cracking and we concluded this was due to the fact the model was analyzed in two

dimensions. Here, in a three-dimensional analysis, we see the appearance of these secondary, radial cracks. These cracks are seen in the top figure in Figure 3.23 as first appearing near where the steel exists the concrete and where the stress is the greatest. As the applied displacement continues the radial cracks originate from the steel beginning more towards the center of the specimen as time goes on. When enough displacement has been applied, two primary cracks form in the middle of the specimen which is probably due to the inference of two tensile stress waves.

The secondary, radial cracks can also be seen propagating from the steel outward by the bottom figures in each of the above Figures. Notice in Figure 3.23, the damage begins in the center where the steel is located then propagates radially from the steel through the concrete to the edge of the specimen. It is worthwhile to mention that most of the damage done in the concrete occurs where the steel exits the concrete, again, where the stress is the greatest.

3.5.1 - Discussion of 3D SPLM Results

Figures 3.18–20 and Figures 3.23–25 show the progression of test simulations which we think are qualitatively reasonable models. We say ‘qualitatively reasonable’ because there is very limited quantitative information on tests like these. We have presented in Section 3.2 many tension-pull tests, but most experiments are done to observe the cracking pattern without specifically recording quantitative results.

When looking at the SPLM test above qualitatively, it seems to follow the description that Gerstle made in his thesis. We can see that there seems to be some

debonding at both ends where the steel exits the concrete, which is expected due to the stress singularity that classical theories predict.

Previously, we provided a load vs. displacement graph Gerstle developed in his thesis (Figure 3.4) for the tension-pull specimen, which is known to be over-simplified. Nonetheless, we have used this graph as comparison of results. Figure 3.26 shows our results compared to what Gerstle provided.

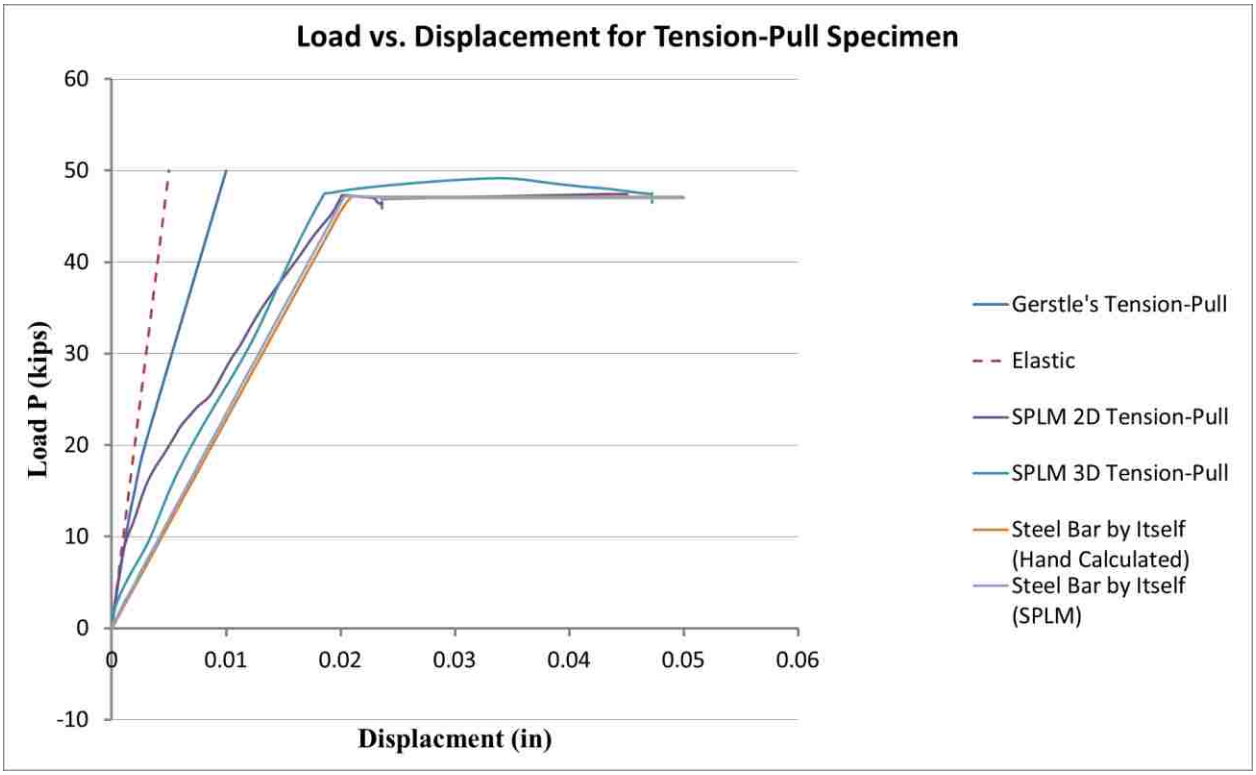

Figure 3.26 – SPLM results versus Gerstle's results

The SPLM predicts a notably softer reaction than what Gerstle predicted, and this could be explained by the fundamental differences in the theories

Figure 3.26 also displays two analyses of a single rebar loaded in tension. The orange line shows a linear elastic, hand calculation of the load vs. displacement curve of the rebar and the sky blue shows the SPLM prediction of this single rebar. The SPLM's

prediction of the steel rebar's load vs. displacement curve follows what we would calculate using linear theories (definite elastic and plastic portion of the curve). Therefore, the SPLM is realistically calculating the reaction of rebar. Figure 3.26, in addition, shows that both the 2D and 3D SPLM analyses are stiffer that the single rebar put in tension. This is expected, as the stiffness of a composite member would be stiffer than a member composed of only one material.

We think, moreover, this bond-slip model is ready to be applied to larger, more applicable problems, which are presented in the next chapter.

3.6 – Summary

Bond-slip has been a focus of study for many engineers because of the increased use of reinforced concrete structures in design. There have been many models and tests presented in this chapter that have tried to accurately model bond-slip and its effect on strength and deformation. Despite the many models presented, it seems that bond-slip is still a misunderstood phenomenon. Or maybe, the numerous scenarios in which bond-slip potentially occurs call for different models? Maybe one is not better than another, just different. We have presented in this chapter an applicable bond-slip model for the SPLM.

The SPLM results show a cracking pattern that is very similar to that of the laboratory data we have researched. The model, moreover, displays reasonable crack propagation, specifically displaying where and when cracking would begin, which objective with respect to the lattice or lattice rotation.

The SPLM's ability to predict these is based on two parameters: K_{bond}, which defines the stiffness of the bond, and the interface horizon of a steel particle. There is an

optimal value for K_{bond} which will ensure the force between the steel particle and the concrete particle is realistic and remains realistic as deformation occurs, meaning the bond doesn't behave like a rubber band and also that the bond isn't too stiff causing stability issues. The interface horizon distance, on the other hand, is the subject of a philosophical debate. What is the radius of influence a steel particle would directly have? Our study has shown that a radius of 1.5 * maximum lattice spacing to 2.0 * maximum lattice spacing yields the best results. The bond-slip model will be applied to several engineering problems in the following chapters.

Chapter 4

Rerun of Gerstle's Beam Trials with the New Bond-Slip Model

This chapter's objectives are to:

- present Gerstle's reinforced concrete beam problems (from [2])
- discuss Gerstle's results
- show our revised models of his problems
- discuss our results

Gerstle [2] performed four simulations of the reinforced concrete beam shown in Figure 4.1. Gerstle's intention was to exhibit the SPLM's capabilities to simulate reinforced concrete beams. Each of the tests only varied in one thing: the steel reinforcement ratio.

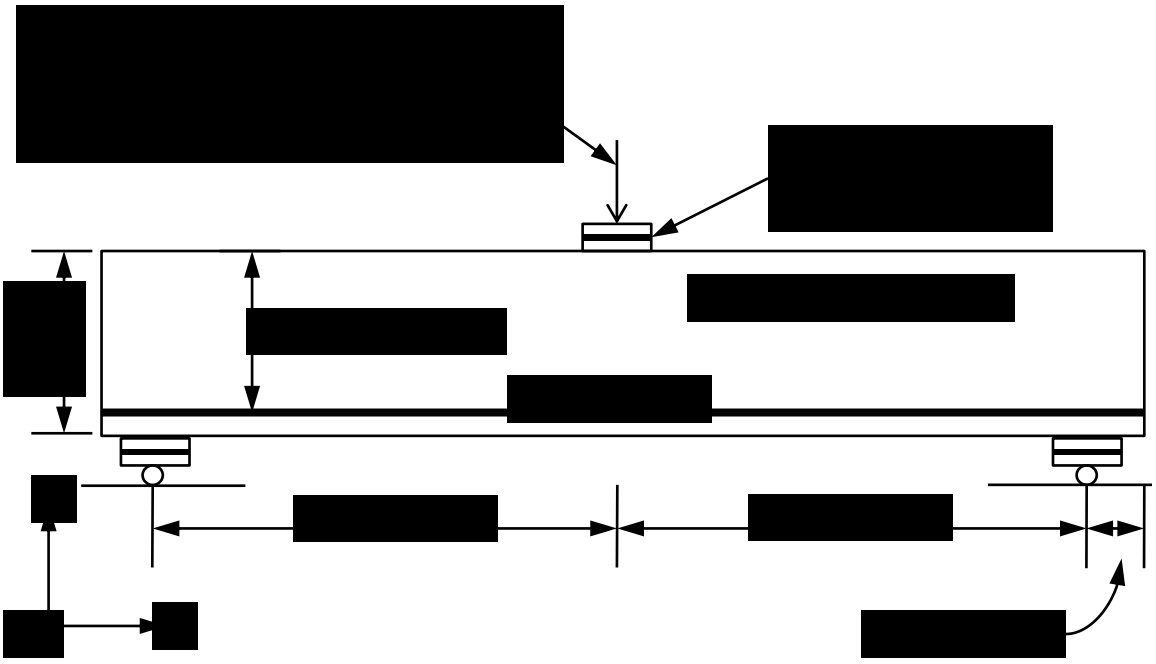

Figure 4.1 – Beam analyzed by Gerstle ([2], pp. 386)

Gerstle tested the beam with steel ratios of $\rho_s = 0.2\%$, $\rho_s = 0.5\%$, $\rho_s = 1.0\%$, and $\rho_s = 2.0\%$. Tables 4.1 and 4.2 show the material parameters used in the analysis.

Parameter	U.S. Customary Units	SI Value
Compressive Strength, $F'_c = \sigma_{yield}$	4000 PSI	27.58 Mpa
Young's Modulus, E	3605 KSI	24.86 Mpa
Poisson's Ratio, ν	0.20	0.20
Mass Density, ρ	145 PSI	2323 Kg/m^3
Lattice Spacing, L	0.3937 in	1.0 cm
Internal Damping Ratio, $\xi_{internal}$	0.20	0.20
Uniaxial Tensile Strength, $F_t = \sigma_t$	400 PSI	2.758 Mpa
Ultimate Tensile Damage Crack Opening Displacement, w_c	0.008739 in	0.20 mm
Tensile Damage Parameter, γ	0.25	0.25
Fracture Energy, G_F (derived)	0.787 lb/in	137.9 N/m

Table 4.1 – Material parameters for concrete

Parameter	U.S. Customary Value	SI Value
Yield Strength, $F_Y = \sigma_{Yield}$	60,000 PSI	413.7 Mpa
Young's Modulus, E	29,000 KSI	200 Gpa
Poisson's Ration, ν	0.30	0.30
Mass Density, ρ	490 PSF	7849 Kg/m^3
Lattice Spacing, L	0.3937 inches	1.0 cm
Damping Ratio, ξ	0.20	0.20

Table 4.2 – Material parameters for steel reinforcement

4.1 – Gerstle's Analysis and Results

4.1.1 – Test Results

Gerstle applied the displacement over eight fundamental periods (T = 0.02 sec) of the structure; the total number of time steps equaled 1.6 million. Gerstle calculated the

fundamental period of the structure using linear elastic analysis. The maximum applied displacement was 0.02 m (0.787 in.) downward or the negative y-direction. Figures 4.2, 4.3, 4.4, and 4.5 show the results of Gerstle's analyses, each figure displaying a different steel ratio.

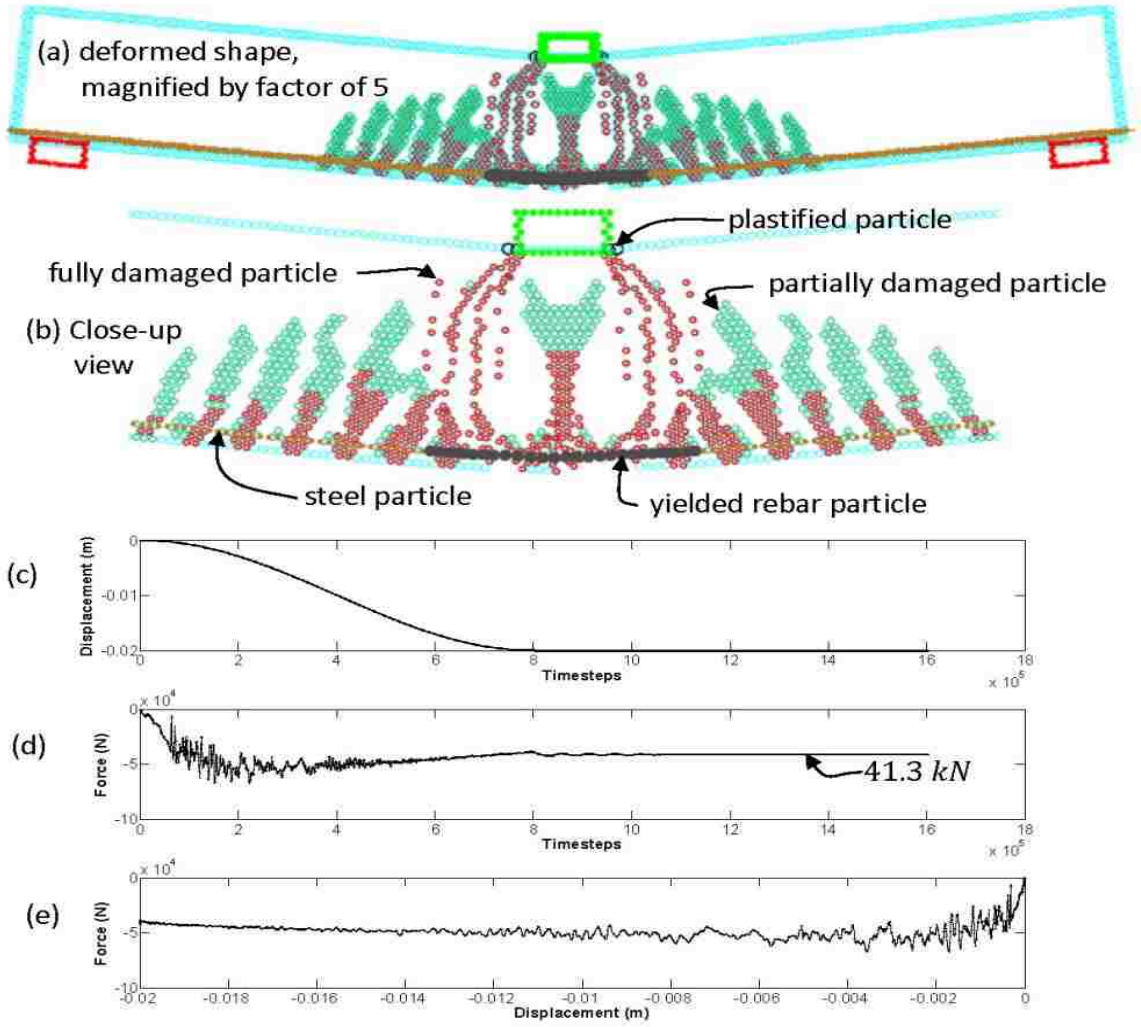

Figure 4.2 – Simulation results of beam with flexural steel ratio ρs=0.2%. (a) Deformed shape at end of simulation; (b) Close-up view; (c) Applied load point displacement vs. time step; (d) Force between loading plate and concrete beam vs. time step; (e) Load vs. load point displacement (from [2], pp. 387)

Using ACI318 [13], Gerstle calculated what the code would predict the strength of these beams would be then compared them to the corresponding SPLM results. Equation 4.1 shows the ACI's flexural beam strength prediction.

$$A_s = A_s bd = 0.2m \times 0.3m \times 0.28m = 0.000168m^2$$

$$a = \frac{A_s F_y}{0.85 F'_c b} = \frac{0.000168m^2 \times 413.7 \times 10^6 Pa}{0.85 \times 27.58 \times 10^6 Pa \times 0.3m} = 0.009882m \quad \textbf{(4.1)}$$

$$M_{n(ACI)} = A_s F_y \left(d - \frac{a}{2}\right) = 0.000168m^2 \times 413.7 \times 10^6 Pa \left(0.28m - \frac{0.009882m}{2}\right)$$

$$= 19.12\ kN - m$$

$$P_{n(ACIbending)} = \frac{4M_{n(ACI)}}{L} = \frac{4 \times 19.12\ kN-m}{2m} = \underline{38.2\ kN}$$

Thus, the SPLM predicts the bending strength of the beam to be 41.3 kN and ACI predicts the bending strength to be 38.2 kN. Gerstle uses Equation 4.2 below to calculate the shear strength of the beam and determine whether flexure or shear controls. In this case, flexure controls.

$$V_{n(ACI)} = 2\left[\sqrt{F'_c (in\ PSI)}(in\ PSI)\right] bd$$

$$= 2\sqrt{4000(PSI)} \times \frac{6894.8Pa}{PSI} \times 0.3m \times 0.28m = 73.3\ kN \quad \textbf{(4.2)}$$

$$P_{n(ACIshear)} = 2V_{n(ACI)} = 2 \times 73.3\ kN = \underline{146.5\ kN}$$

Gerstle performs these calculations after every analysis and we will summarize the results at the end of this section.

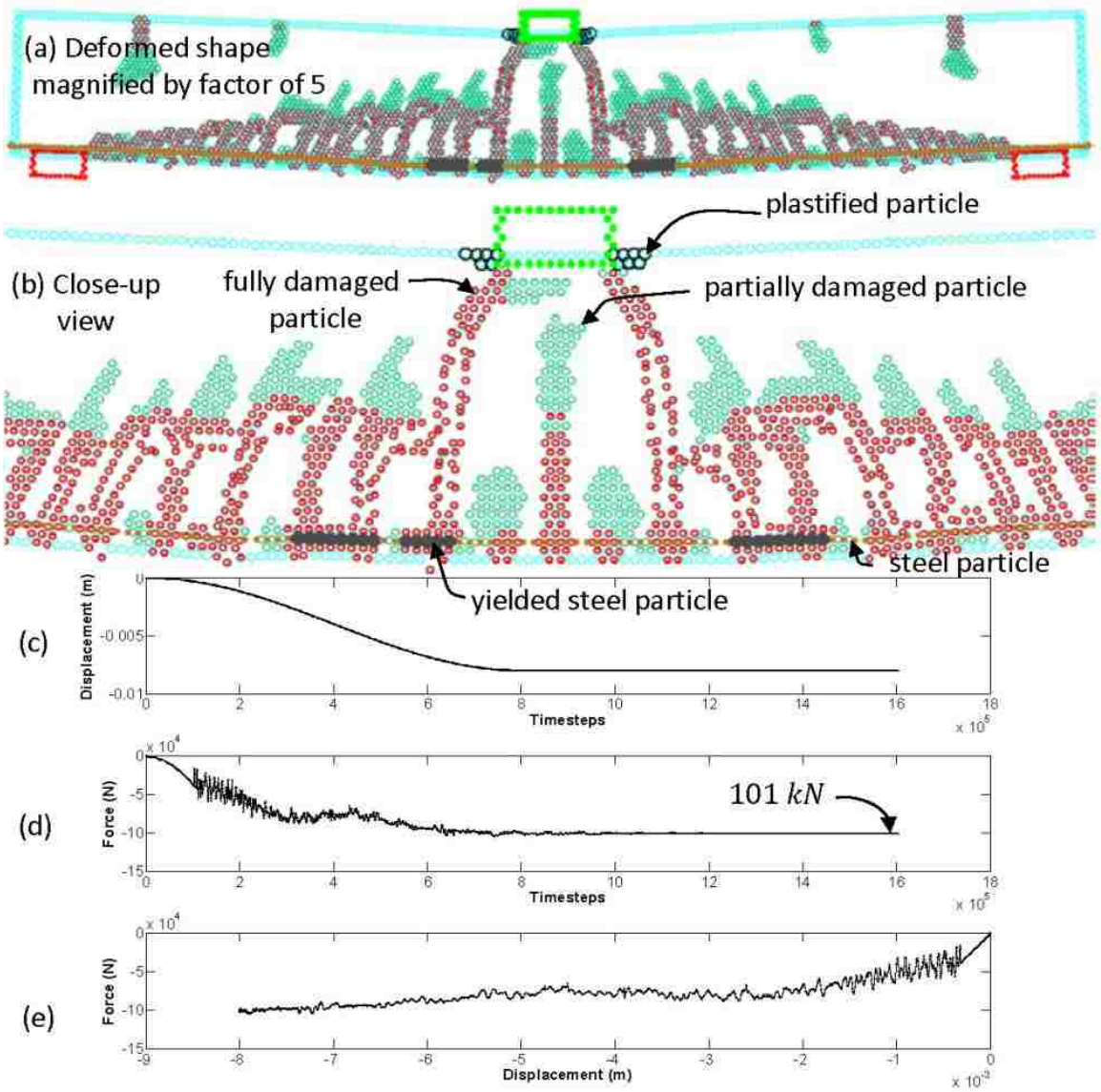

Figure 4.3 - Simulation results of beam with flexural steel ratio ρs=0.5%. (a) Magnified deformed shape at end of simulation; (b) Close-up view; (c) Applied load point displacement vs. time step; (d) Force between loading plate and concrete beam vs. time step; (e) Load vs. load point displacement (from [2], pp. 389)

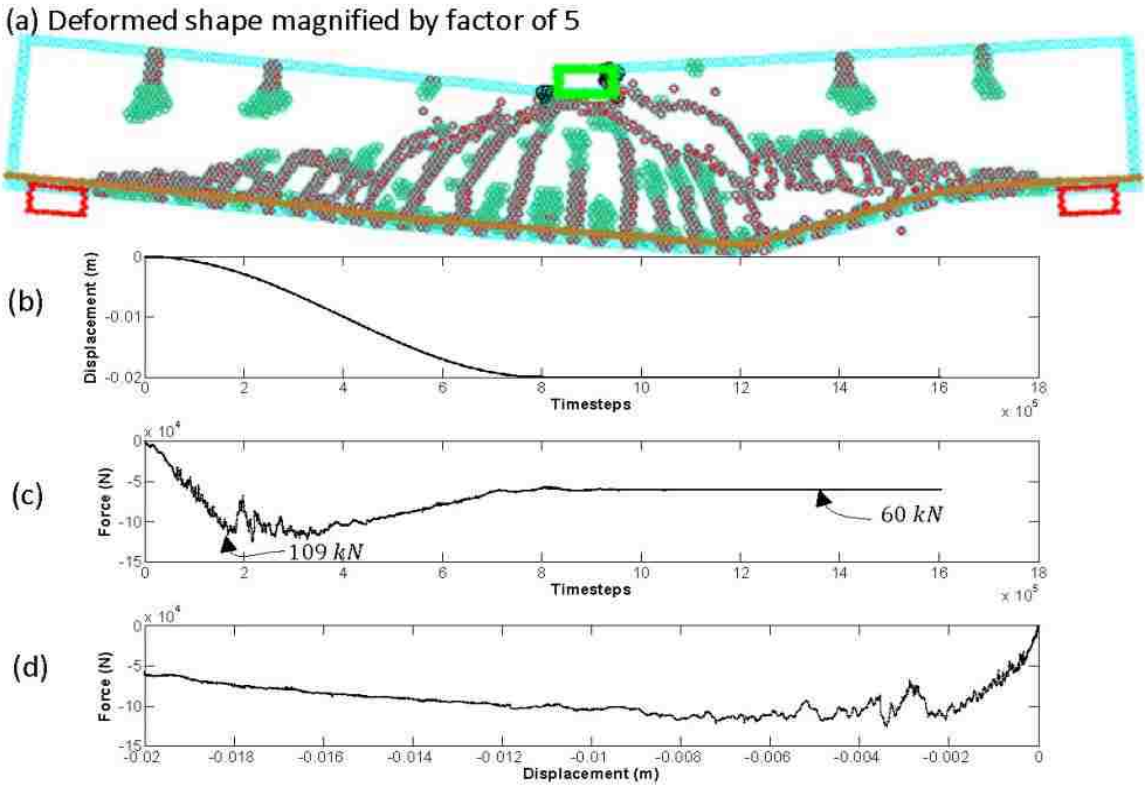

Figure 4.4 - Simulation results of beam with flexural steel ratio ρs=1.0%. (a) Deformed shape at end of simulation; (b) Applied load point displacement vs. time step; (c) Force between loading plate and concrete beam vs. time step; (d) Load vs. load point displacement (from [2], pp. 390)

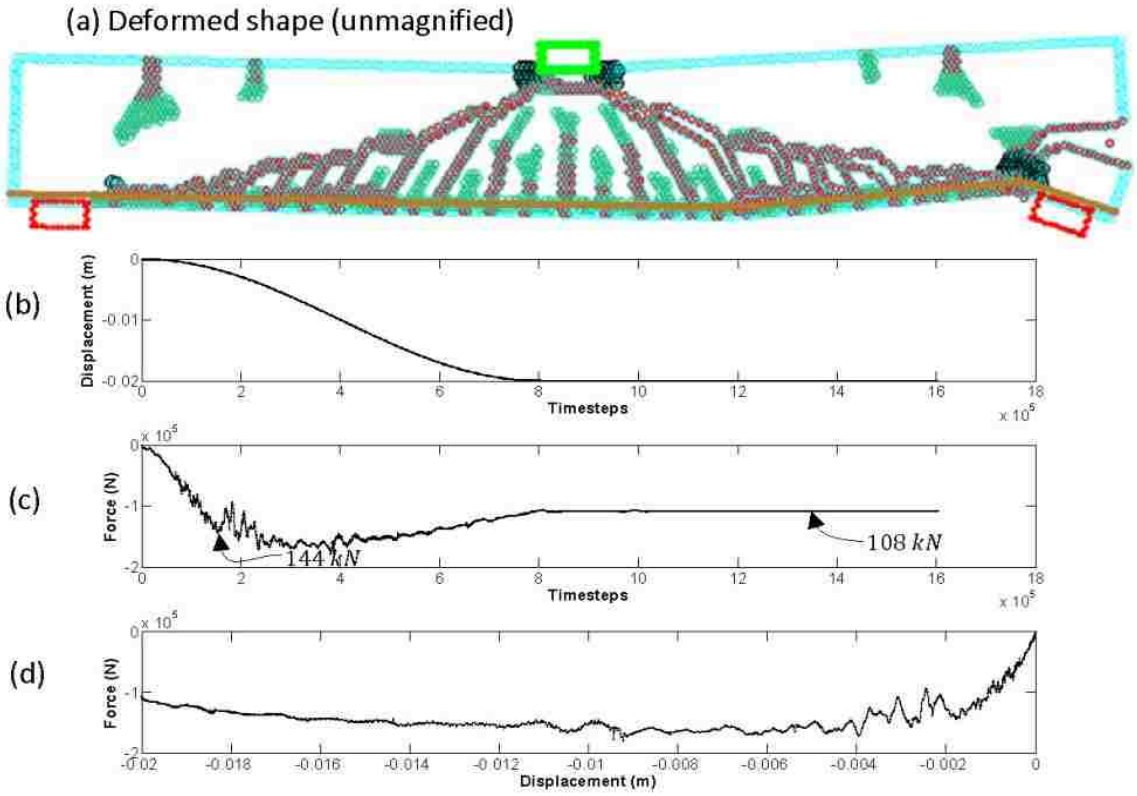

Figure 4.5 - Simulation results of beam with flexural steel ratio ρs=2.0%. (a) Deformed shape at end of simulation; (b) Applied load point displacement vs. time step; (c) Force between loading plate and concrete beam vs. time step; (d) Load vs. load point displacement (from [2], pp. 391)

4.1.2 – Discussion of Test Results

Table 4.3 summarizes Gerstle's results and compares them to ACI.

ρ_s	$P_{ACI,V}$	$P_{ACI,M}$	Failure Mode	P_{SPLM}	Failure Mode
0.2%	146.5 kN	38.2 kN	Flexure	41.3 kN	Flexure
0.5%	146.5 kN	93 kN	Flexure	101 kN	Flexure
1.0%	146.5 kN	177.4 kN	Shear	109 kN	Shear
2.0%	146.5 kN	320.5 kN	Shear	144 kN	Anchorage

Table 4.3 – Summary of ACI and Gerstle's predictions

Gerstle's beam simulations take into account elastic, plastic, and damage behavior. The graphs in Figures 4.2-4.5 display an initial linear elastic curve signifying

an initial elastic response upon loading, which is what we would expect. As the displacement increases, we observe that flexural cracks appear and begin to propagate, first under the load, working outward toward the supports. It is also apparent in each of the figures that there is cracking. The cracking propagates from the flexural cracks at a near 45 degree angle toward the point of loading, which is what we expect to see as well. This seems to validate the plastic and damage models within SPLM.

The correct cracking pattern is not the only aspect favoring the plastic and damage models. As seen in Figure 4.2 and 4.3, the steel particles are yielding. We would expect the steel to yield in these two tests because the beams are under-reinforced. It also makes sense that flexural failure would control, due to the low steel ratios. As both the ACI and SPLM predict, as the steel ratio increases, shear would begin to eclipse flexure and eventually control. We wish to point out that Gerstle predicts an anchorage failure when the steel ratio is greatest, as seen in Figure 4.5. This is explainable in that there may be an insufficient amount of concrete covering the large amount of steel both along the length of the beam and the height. Essentially, Gerstle is modeling rebar pullout which is reasonable considering the amount of steel.

Gerstle argues that the SPLM results are sufficient and realistic for a number of reasons. First, he says neither the ACI nor the SPLM are highly precise but the SPLM results seem more rational and reasonably predicts much more behavior than the ACI including crack spacing, deflections, and dynamic effects. Secondly, each method of prediction has different approximations taken into account. Thirdly, concrete is a random material. No two concrete specimens are the same, and therefore, we cannot expect every specimen to react the same to the same loading. Gerstle emphasizes no engineer should

only rely on or expect high precision in ACI or SPLM, but argues the SPLM rationally simulates concrete's essential features which the ACI code does not.

Qualitatively, the results from the SPLM models are convincing. They display the overall reaction of a reinforced concrete that we would expect to see. In light of this success, we have re-run Gerstle's tests to reemphasize the success of the SPLM's application of elastic and plastic models, implement our bond-slip model developed in the previous chapter, and setup our model used in Chapter 6 of this work. We discuss our tests in the next section.

4.2 – Rerun with the New Bond-Slip Model

Using the same geometry shown in Figure 4.1, the same material parameters shown in Tables 4.1 and 4.2, and the same steel ratios, we reran Gerstle's tests to verify his results. Our model, however, was run with the new bond-slip model discussed in Chapter 3. Figure 4.6 shows the analysis with a beam having a steel ratio of 0.2%.

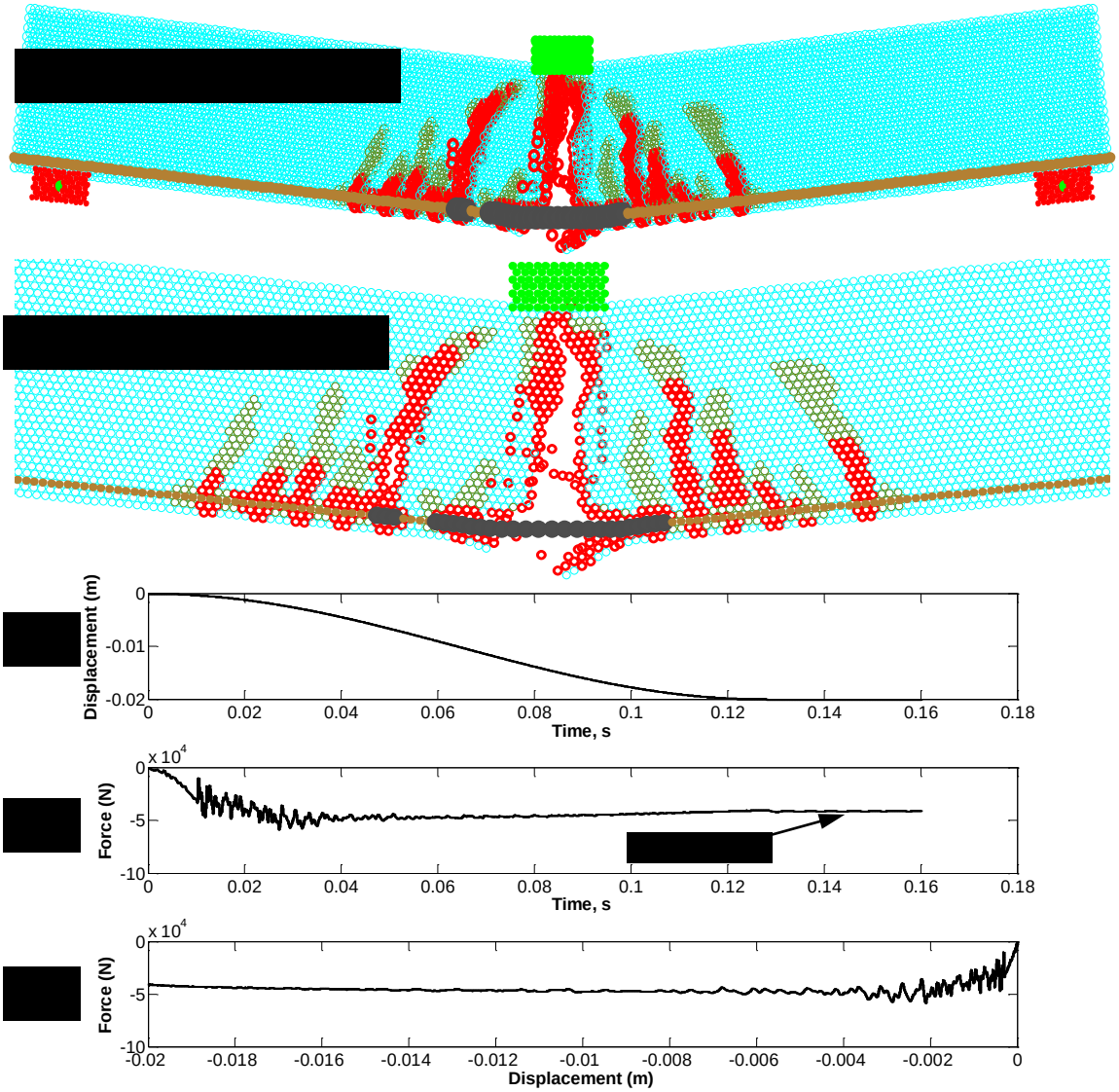

Figure 4.6 – Simulation results of beam with flexural steel ratio ρs=0.2%. (a) Deformed shape at end of simulation; (b) Close-up view; (c) Applied load point displacement vs. time step; (d) Force between loading plate and concrete beam vs. time step; (e) Load vs. load point displacement

The SPLM with the new bond-slip model predicts the strength of the beam to be 41.1 kN, which is 0.5% lower than what Gerstle predicted in [2] and 7.6% greater than what ACI predicts. Notice in Figure 4.6 a) that a primary flexural crack is controlling the strength, which is what both Gerstle and ACI predict. There are some differences between our SPLM results and Gerstle's SPLM results. Obviously one is the minor difference in

strength, but in Gerstle's analysis, there was crushing of concrete which did not happen when the new bond-slip model was implemented which may be due to the increase in interface horizon distance. Also, the primary flexural crack in Gerstle's analysis was not as severe as what our model shows, which is most likely due to the stiffness in the bond-slip model used by Gerstle. Figure 4.7 shows the SPLM analysis of the beam with a steel ratio of 0.5%.

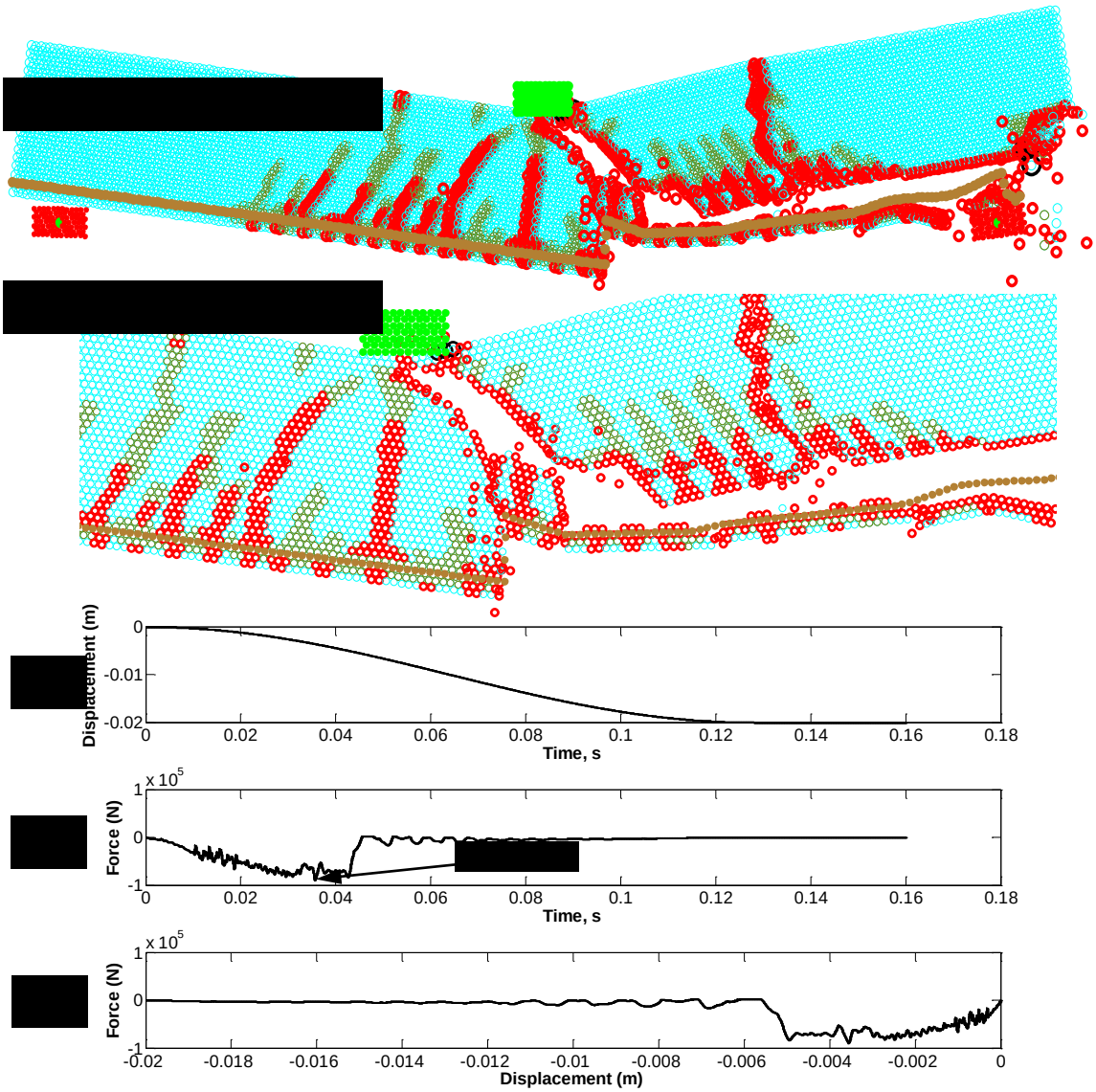

Figure 4.7 – Simulation results of beam with flexural steel ratio ρs=0.5%. (a) Deformed shape at end of simulation; (b) Close-up view; (c) Applied load point displacement vs. time step; (d) Force between loading plate and concrete beam vs. time step; (e) Load vs. load point displacement

The cracking pattern of shown in Figure 4.7 is different than what Gerstle's cracking pattern looked like. His cracking pattern (Figure 4.3) looked more like what we would expect to see given the steel ratio of the beam, as we would expect the beam to be controlled by flexure. However, our strength prediction of the beam is closer to what ACI would predict. Our model predicts a strength that is 3.2% lower, where Gerstle's prediction was 8.6% higher. Figure 4.7 also shows that the beam will fail in shear which neither Gerstle nor ACI predicted—they predicted it would fail in flexure at a load of 93 kN. Figure 4.8 shows the results of a beam loaded with a steel ratio of 1.0%.

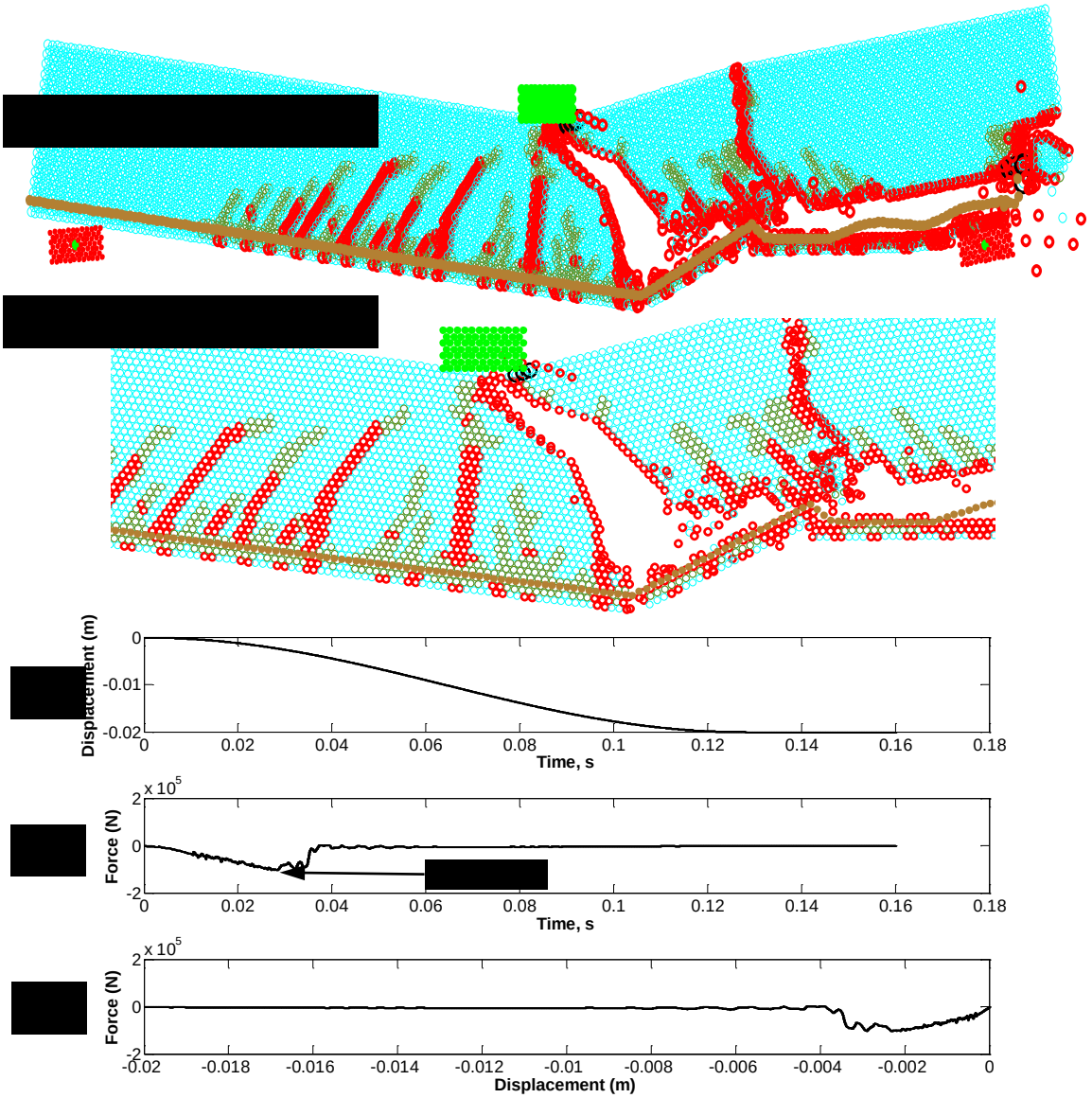

Figure 4.8 – Simulation results of beam with flexural steel ratio ρs=1.0%. (a) Deformed shape at end of simulation; (b) Close-up view; (c) Applied load point displacement vs. time step; (d) Force between loading plate and concrete beam vs. time step; (e) Load vs. load point displacement

Figure 4.8 shows that the beam is failing in shear which both Gerstle and ACI would predict. However, our beam has a strength of 102 kN, which is 6.4% lower than Gerstle's prediction and 30.4% lower than ACI. As Gerstle points out ([2], pp. 391), the difference between the ACI strength and the SPLM's prediction is most likely due to the fact that the ACI considers post-cracking aggregate interlock whereas the SPLM does not.

Considering aggregate interlock would increase the strength of the beam and something which future SPLM researchers should consider implementing into the model. Figure 4.9 shows a simply supported beam with a steel ratio of 2.0% loaded in the middle.

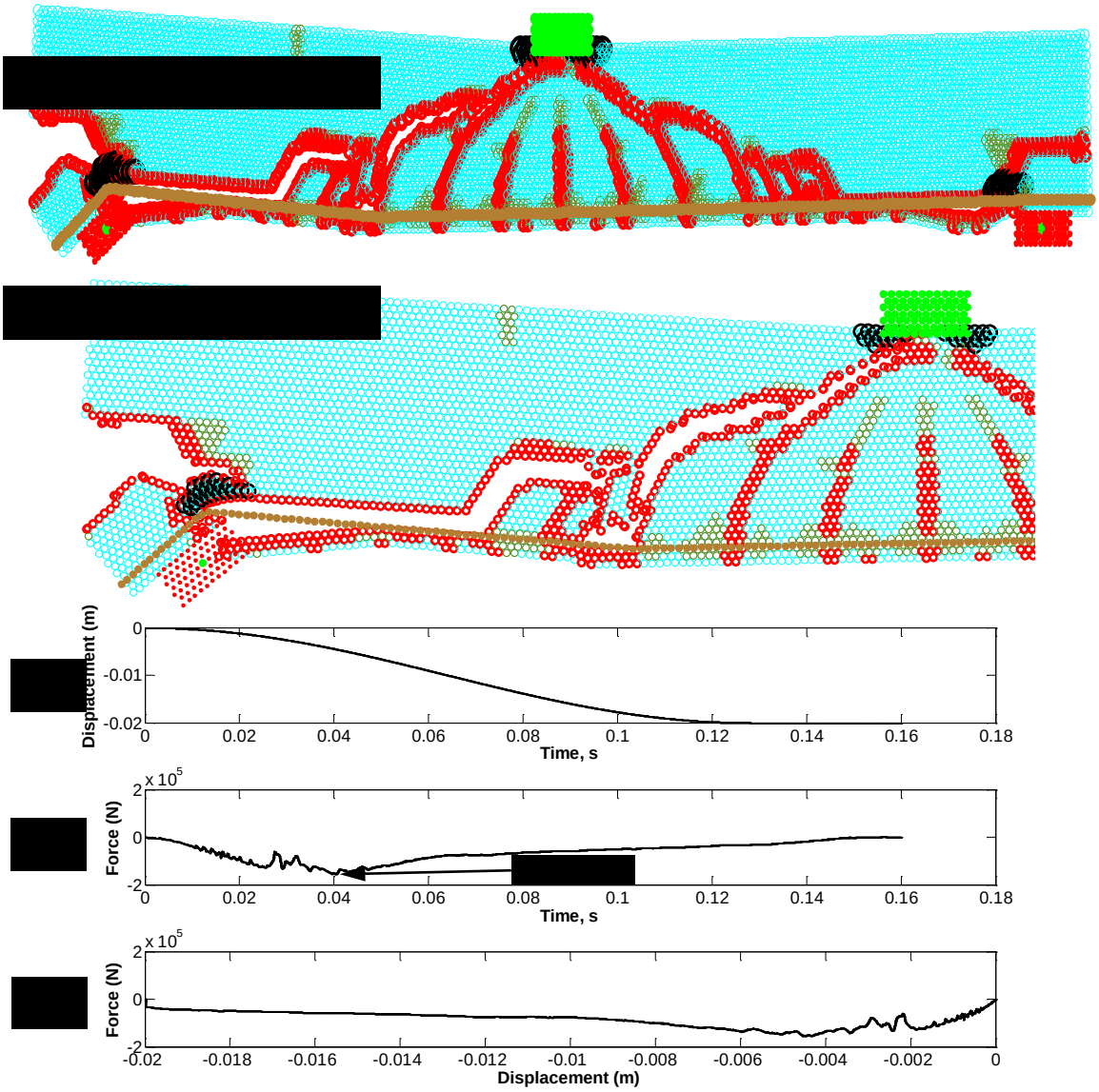

Figure 4.9 – Simulation results of beam with flexural steel ratio ρs=2.0%. (a) Deformed shape at end of simulation; (b) Close-up view; (c) Applied load point displacement vs. time step; (d) Force between loading plate and concrete beam vs. time step; (e) Load vs. load point displacement

The SPLM predicts a strength of this heavily reinforced beam to be 153 kN, which is 4.4% greater than ACI and 6.25% greater than Gerstle's prediction. The ACI code

predicted a shear failure, but we observe more of an anchorage failure. The closeness of the model's prediction is probably coincidence since the failure modes are different. Note that the beam continues to carry load after the anchorage failure occurs. As Gerstle, again, points out ([2], pp. 392), the ACI does not make special provisions for anchorage failure but uses a minimum development length as a way to avoid anchorage and splice failures.

4.2.1 – Discussion of Rerun Trials

Table 4.4 summarized our results compared to ACI and Gerstle.

ρ_s	$P_{ACI,V}$	$P_{ACI,M}$	Failure Mode	$P_{SPLM,G}$	Failure Mode	$P_{SPLM,M}$	Failure Mode
0.2%	146.5 kN	38.2 kN	Flexure	41.3 kN	Flexure	41.1 kN	Flexure
0.5%	146.5 kN	93 kN	Flexure	101 kN	Flexure	90 kN	Rebar Pull-Out
1.0%	146.5 kN	177.4 kN	Shear	109 kN	Shear	102 kN	Rebar Pull-Out
2.0%	146.5 kN	320.5 kN	Shear	144 kN	Anchorage	153 kN	Anchorage

Table 4.4 – Summary of our results compared to ACI and Gerstle

After implementing the new bond-slip model, the SPLM produced results that were different from ACI and Gerstle. The results were not necessarily wrong but different. We saw that as the steel ratio goes up, it seems to have a major effect upon the cracking pattern of the beam, but to a lesser degree the strength. With a low steel ratio of 0.2%, the SPLM was able to model the crack pattern and strength that was extremely close to what ACI would predict. In this trial, the beam was able to hold the load throughout the entire simulation.

As the steel ratio increased to 0.5% the SPLM showed it is sensitive to the amount of steel in the beam as the cracking pattern and failure mode differed from the ACI. The ACI predicted the beam would be controlled by its flexural strength, but the SPLM clearly showed a classic bond failure. What is interesting to note is the fact that Gerstle's trials had post peak strength, or where the beam would continue to hold load after it "failed". Our rerun trials, however, did not have post-peak strength but failed completely, not being able to hold any load.

As we increased the steel ratio even more, to 1.0%, the beam, again, failed differently than what ACI would predict. The SPLM predicts classic bond failure and a strength much lower than ACI. The unsymmetric action causes one half of the beam to take more of the load since energy will dissipate where the least amount of energy is required resulting in an increase in cracking where damage has already occurred.

Upon reinforcing the beam very heavily with a steel ratio of 2.0%, the strength predictions between us and the ACI were relatively close. The beam, as predicted by ACI, would fail in shear at a load of 146.5 kN but the SPLM predicts an anchorage failure at a load of 153 kN.

As we mentioned previously, ACI uses a minimum development length to avoid anchorage, splice, and bond failures. Considering this, we calculated the development length for the rebar in each of the simulations. According to ACI318 [13], the development length for this particular beam's geometry is:

$$\ell_d = 71 d_b, \text{ where} \qquad \textbf{(4.3)}$$

ℓ_d is the development length and d_b is the diameter of the rebar. Therefore, as the diameter of the rebar increases, the development length increases. This is important to

consider in the simulations presented in this chapter because while the steel ratio is increasing the geometry of the beam is not. Therefore, the rebar may not be fully developed.

Table 4.5 shows the required development length for each of the four steel ratios.

ρ_s	Span Length	d_b	ℓ_d
0.2%	6.5 ft	0.6 in	3.6 ft
0.5%	6.5 ft	0.95 in	5.6 ft
1.0%	6.5 ft	1.34 in	7.9 ft
2.0%	6.5 ft	1.89 in	11.2 ft

Table 4.5 – Required development length

Table 4.5 shows that based on the unchanging geometry of this problem, the rebar is *not* developed in any of the four steel ratio scenarios. Because the rebar is not fully developed in any of the simulations, we can expect rebar pull-out. Considering the four SPLM simulations in this light seems to validate our bond-model, as the SPLM displays pull-out for the higher steel ratios. We point out that although the lowest steel ratio of 0.2% was not fully developed, the SPLM predicts the strength or mode of failure not affected by this. Therefore, there seems to be a leeway in the development length given by ACI.

4.3 - Summary

In this chapter, we implemented the new bond-slip model discussed in Chapter 3. We showed in Chapter 3 that the SPLM produced reasonable results for small two-dimensional and three-dimensional tension-pull models. Therefore, in this chapter we

implemented that bond-slip model into the most basic structural analysis problem: a point loaded simply-supported beam.

We simulated four beams varying ρ_s only. We compared our analysis using the SPLM with Gerstle's results and with what ACI would predict. The SPLM with the new bond-slip model predicted similar results for a very low reinforced beam, when $\rho_s = 0.2\%$ when compared to Gerstle and ACI. As we increased the steel ratio, however, the mode of failure differed from Gerstle and ACI. This is due to the development length of the rebar. The rebar is not fully developed and pull-out failure, shown in our results, is explainable.

We implement the new bond-slip model in a very large beam that is mildly reinforced in Chapter 6. We discuss sequential load application in the next chapter.

Chapter 5

Sequential Loading

This chapter's objectives are to:

- Describe the need for sequential loading in nonlinear analysis
- Propose a sequential load application method
- Demonstrate the sequential load method

5.1 – Linear vs. Nonlinear

When considering linear analysis, the principal of superposition can be used. That is, displacements and/or loads occurring at different times can be added together to determine the maximum displacement/maximum load. Therefore, there is no need for the use of stage loading based on the very definition of linear. However, for nonlinear problems the principal of superposition cannot be used. Thus, there is a need for stage loading. Because we want to sufficiently model nonlinear problems, we need to implement stage loading into the SPLM.

Therefore, we propose sequential load application in the next section.

5.2 – Proposed Sequential Load Application Method

Principally, this process will break up our analysis into many stages of potential loadings the member will experience by externalizing some of the simulation's characteristics through 'Restart files'.

The SPLM writes out restart files depending on what the user has defined. The amount of restart files is a fraction of the amount of total time steps in the simulation.

Thus, if there are 20 time steps in the simulation and user wants the program to write out 5 restart files, this can be accomplished easily. The SPLM calculates various parameters for each particle located in the structure for every time step. Therefore, the user knows exactly what each particle is doing through the entire simulation, including the particles boundary conditions, current and reference positions, current and reference velocities, amongst others.

The SPLM begins a simulation by writing out a file termed '*restart.0'*, which describes the particles reference characteristics. This is when time is equal to zero. Furthermore, the SPLM writes out a file termed '*userInput*', which describes all the constitutive properties of the particles including Young's modules, lattice spacing, and the critical time step. The SPLM also writes out two other files termed '*input*' and '*postProcParams*', which help describe the initial model. Essentially these files establish all the characteristics of the model before any load is applied. This is important for SPLM because the user has the ability to take the restart file from the last time step in a previous stage's simulation and apply it to a new stage. Before now, the SPLM did not call restart files in programming and could not use previous stages' information. Therefore we have brought innovation and efficiency to the model.

We have at this point which is relevant to this thesis, defined two stages of loading: self-weight and an external point load. We will discuss the application of both in the SPLM. The self-weight is the load the beam will feel first and the load we apply to the particles first. Each particle will have its own self-weight according to its mass and the acceleration due to gravity. We have calculated the self-weight of each particle using Newton's second law. We then apply this force in the y-direction for each particle for a

specified amount of time. Applying the gravitational force for a predetermined amount of fundamental periods allows the beam to react and displace as if we were doing a static analysis. In the next section, we will demonstrate the sequential load application method in an example.

5.3 – Example of Sequential Loading

5.3.1 – Sequential Loading for Self-Weight

We can calculate the deflection, δ, of the beam shown in Figure 5.1 due to the beam's own self weight using classical beam theories as a means of comparison.

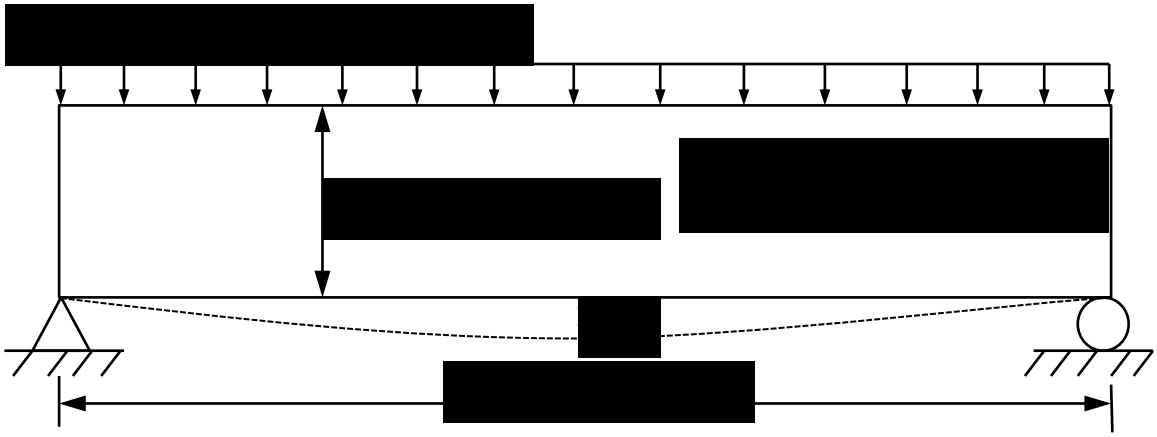

Figure 5.1 – Geometric parameters of beam loaded under its self-weight

δ_{max} using the classical theory is:

$$\delta_{max} = \frac{5wL^4}{384EI}, \text{ where} \qquad \textbf{(5.1)}$$

w is the self-weight of the beam (in this case), L is the clear span length of the beam, and EI is the flexural rigidity of the beam. According to Equation 5.1, the maximum deflection of the beam is 7.44×10^{-6}m (2.93×10^{-4} in).

In the SPLM we applied the beam's self-weight for 4 fundamental periods to reach a quasistatic solution. We also have within the SPLM the ability to monitor the displacement and forces a specific particle experiences during the simulation. In order to get the best prediction and comparison, we monitored particle 108 which is the particle located at the bottom of the beam in the center where there maximum deflection would take place, as seen in Figure 5.2.

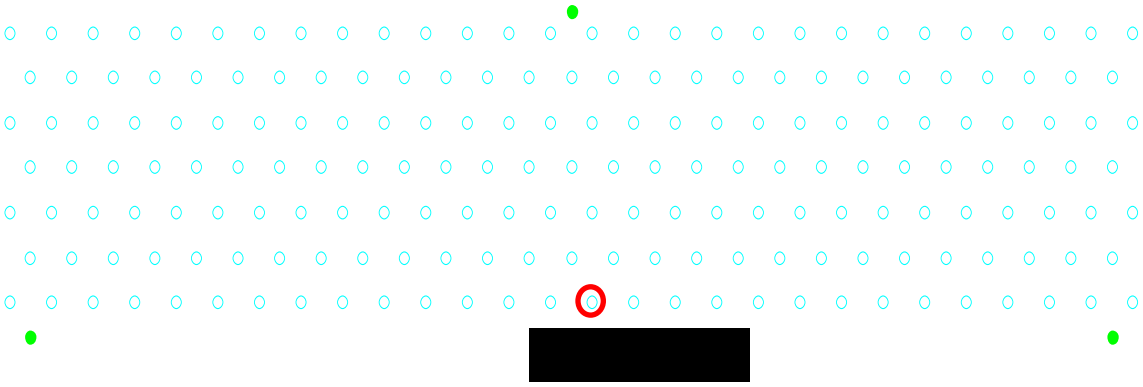

Figure 5.2 – Particle 108 in concrete beam under its self-weight

Figure 5.3 shows the deformed shape of our self-weight beam.

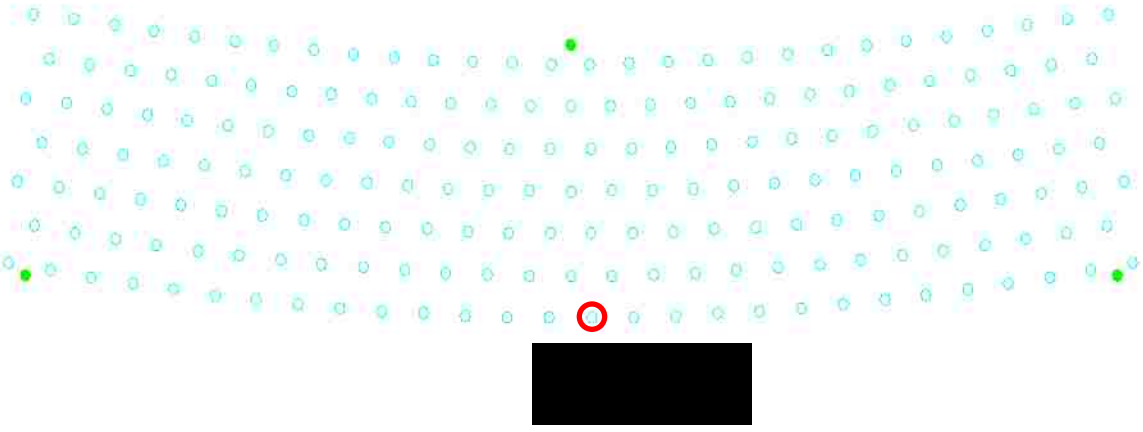

Figure 5.3 – Deformed shape of beam under its self-weight, deformation magnified by 10,000

The beam is deflecting in the way that we would expect, in a smooth quadratic shape with the maximum deflection in the middle. To compare the values of maximum deflection, we show the displacement of particle 108 as a function of time in Figure 5.4.

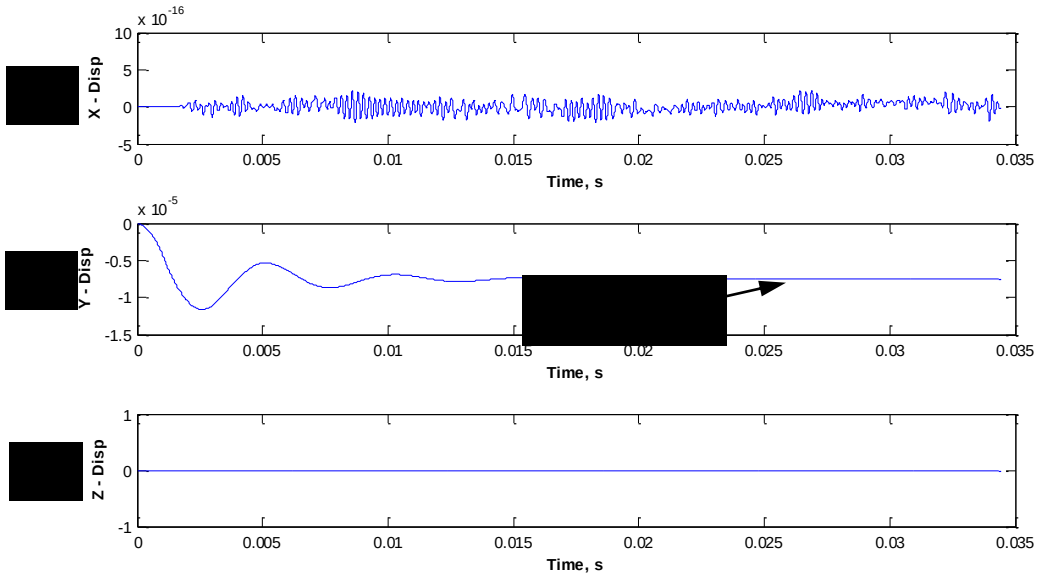

Figure 5.4 – a) x-displacement vs. time; b) y-displacement vs. time; c) z-displacement vs. time of particle 108

The SPLM predicts the maximum deflection of the beam to occur at the center of the beam, at particle 108, and equal to 7.523×10^{-6} m (2.96×10^{-4} in). Notice in Figure 5.4 there is no movement in the particle in the Z-direction, indicating there is no out of plane stretches or forces. There is, however, movement of the particle in X-direction which is significantly smaller to the movement in the Y-direction and is due to its freedom to move in the X-direction, which we specified in the SPLM. The SPLM predicts a deflection which is 1.1% greater than the classical theory would predict. This is reasonable due to fundamental differences between theories.

Also notice that we applied the gravitational force over a very short amount of time which we applied to simulate a sudden application of the gravity on the beam when it is placed on the supports. Once the gravitational force was applied, particle 108 experienced a bouncy action which is realistic. The beam will, accordingly, over-displace then settle down to a constant displacement (static solution). Therefore, self-weight has been shown to be successfully applied to the SPLM. In the next section we will show how we implemented the last restart file from this self-weight loading simulation into a new stage where an external point displacement is applied.

5.4.2 – Sequential Loading for an External Point Load

The SPLM can successfully apply the self-weight of a beam, but we are more interested the SPLM's ability to apply previous stages' information into a new stage. Figure 5.5 shows the beam we will analyze in the SPLM to demonstrate this.

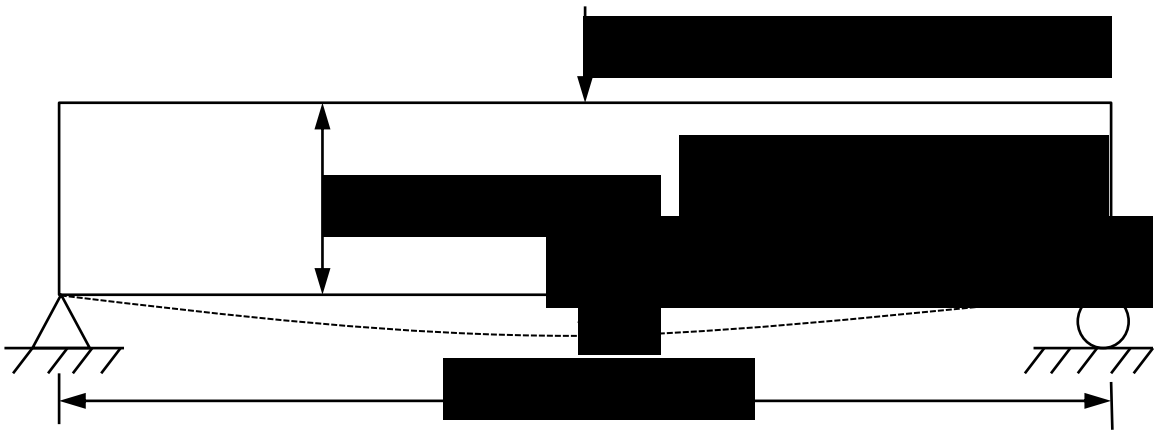

Figure 5.5 – Geometric parameters of beam loaded under its self-weight and an external point load

We will apply an external point displacement to the beam under complete elastic conditions—no damage or plasticity—to explore whether the SPLM can successfully

implement previous stages' information. Also, we will show that the SPLM can predict the load that should cause a certain displacement when compared to the classical theory.

Sequential loading allows us to use the results from a previous stage (in this case the application of the self-weight of each particle) and implement that information to run another analysis where we apply a displacement simulating an external point load. The benefits will allow us to view times of interest while simultaneously easing the modeling process. Using the information the SPLM calculates, which consists of the boundary conditions, positions, velocities, etc., for the last time step of the self-weight analysis as the first time step of the simulated point load we can evaluate the beam in a different simulation.

We applied three displacements to the beam simulating three different point load analyses and the results are summarized in Table 5.1. The classical theory predicts the maximum deflection of the beam to equal:

$$\delta_{max} = \frac{PL^3}{48EI}. \tag{5.2}$$

Therefore, we can rearrange Equation 5.2 to solve for an applied load that will cause a certain deflection.

Deflection, δ_{max} (m)	SPLM Load Prediction, P (kN)	Classic Theory Prediction, P (kN)	Difference
0.000121	12.7	11.7	8.18%
0.0005	50.1	48.5	3.32%
0.001	100.0	97.0	3.11%

Table 5.1 – Load prediction comparison between the SPLM and linear elastic theories

Table 5.1 shows the SPLM's ability to predict the load which causes a certain displacement on a beam. To further verify the SPLM, Figure 5.6 shows the deformed shape of the beam under its own self-weight and Figure 5.7 shows the deformed shape of that same beam with an applied displacement of 0.001 m and which uses the information from Figure 5.6 as its beginning time step.

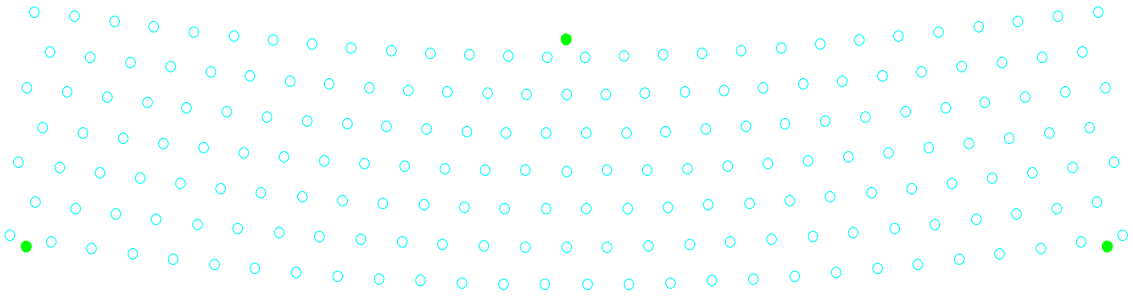

Figure 5.6 – Deformed shape of beam for first stage (self-weight), deformation magnified by 10,000

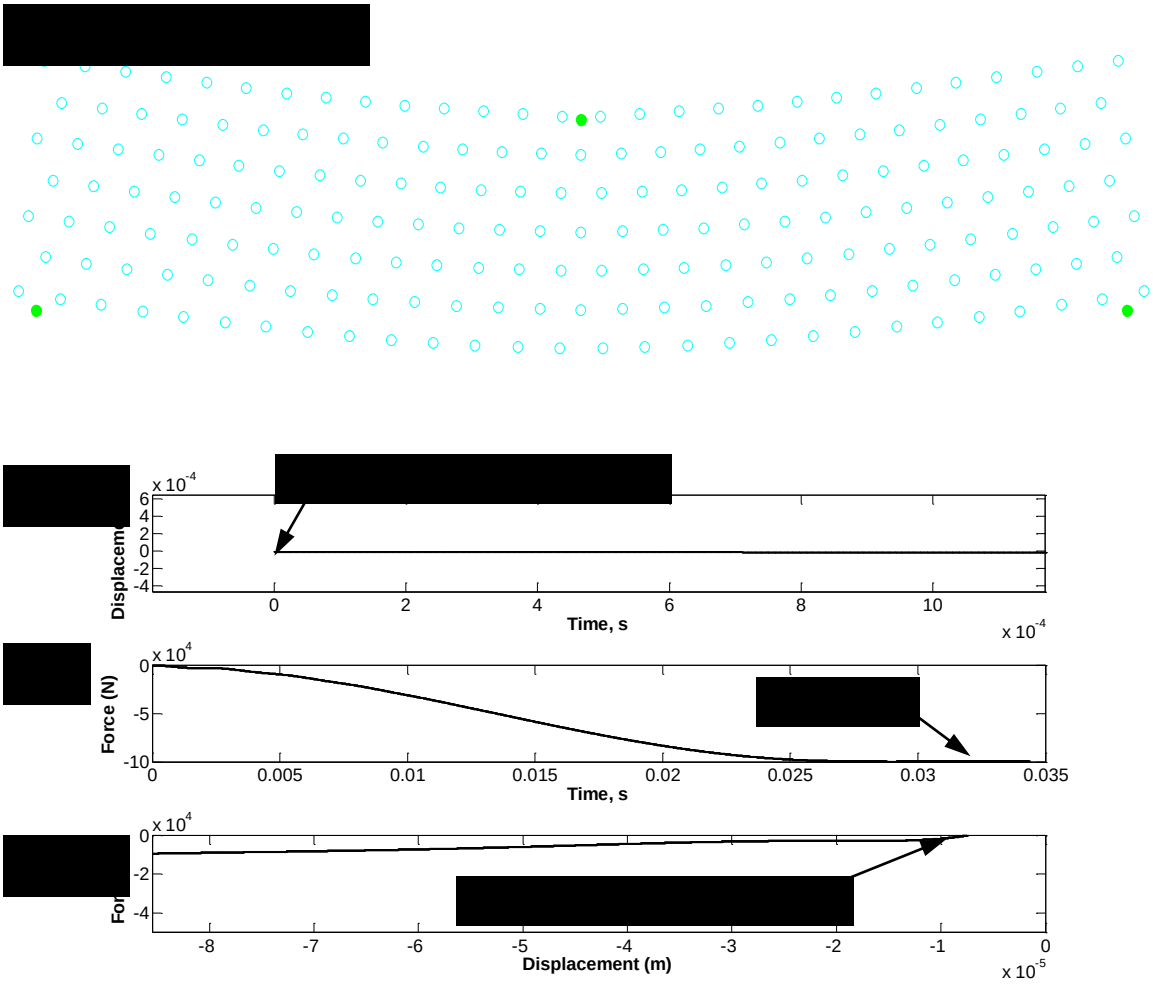

Figure 5.7 – a) Deformed shape of beam for second stage (applied displacement of 0.001 m), deformation magnified by 10,000; b) displacement vs. time; c) force vs. time; d) force vs. displacement

Notice in Figure 5.7 d) that the displacement does not begin at zero but at the self-weight displacement of the beam. This confirms that the information from the first stage was implemented successfully. Also notice that in c), which records the force between the steel loading plate represented by one particle on top of the beam and the concrete particles it is bonded with, the force reaches 100.0 kN. Nonetheless, the SPLM has demonstrated its ability to simulate the self-weight deflection as well as a point load applied to a beam.

5.4 – Summary

In this chapter we presented sequential loading into the SPLM. Implementing stages into the SPLM will allow us to analyze nonlinear problems more sufficiently and effectively. For example, in prestressed concrete beams there are numerous stages which each have different types of loads being applied to the beam. Thus, having the ability to simulate each stage will benefit users of SPLM in the future by providing an effective way to analyze nonlinear problems. Furthermore, implementing stages will allow the engineer to view the results he or she desires to view. The engineer now has the ability to view the deflection or the crack pattern of beam of a certain stage without having to significantly change the code and without having to wait for the entire analysis to run to see if the parameters changed in each change were correctly implemented. They can simply use information from a previous stage and change the necessary information such as time of simulation, boundary conditions of certain particles, or velocities of particles, and then continue analysis of the next stage.

We, moreover, showed that the SPLM can successfully predict a beam's deflection under its own self-weight. The SPLM also proved to be able to predict a load that would cause a certain deflection. Although there were differences between the classical theory's prediction and the SPLM prediction, the differences were small and this is expected. Sequential loading can now be implemented into a bigger, more applicable analysis, discussed in the next chapter.

Chapter 6

Toronto Beam

This chapter's objectives are to:

- Describe the Toronto beam competition
- Calculate crude estimates of the failure load of the beam using ACI
- Predict the failure load of the beam using SPLM
- Present the results of the laboratory test
- Compare SPLM results to laboratory test results
- Present a post-diction for the large beam

6.1 – Introduction

On May 12, 2015 we received an invitation to participate in a competition hosted by the University of Toronto in Toronto, Canada. Dr. Evan Bentz and Dr. Michael Collins of the University of Toronto constructed a very large reinforced concrete beam, in which they would load approximately in the center, in pursuit of a better understanding of the shear strength of very thick one-way slabs.

Figure 6.1 shows the beam drawn to scale as provided by Bentz and Collins (see Appendix A).

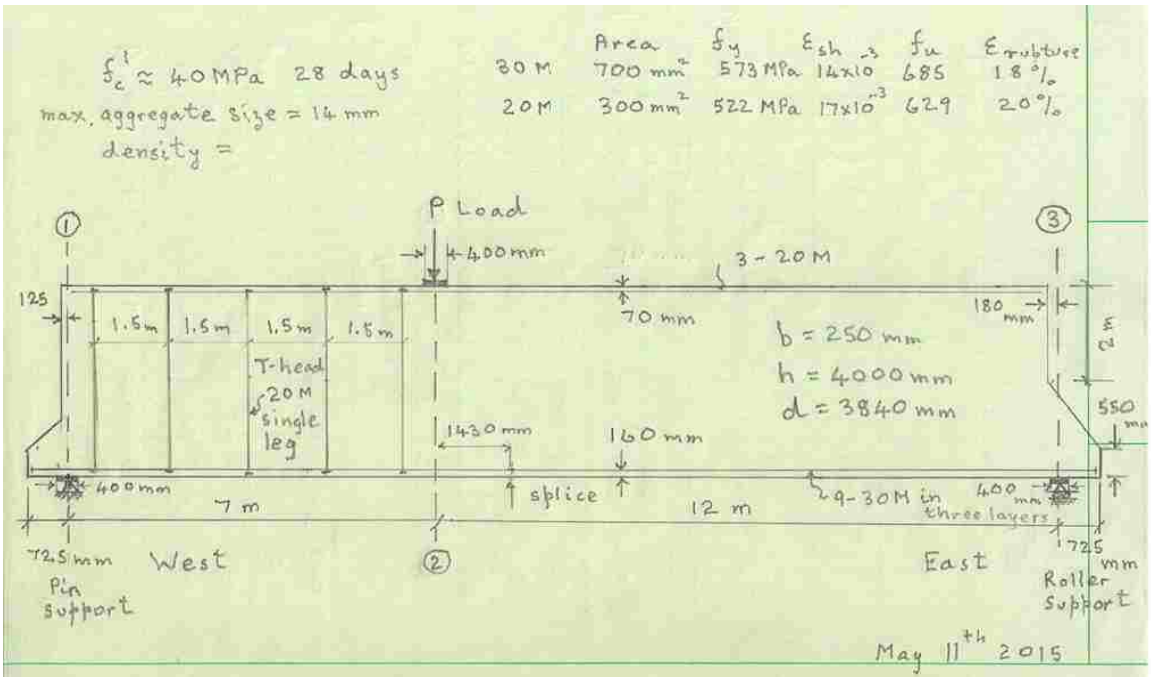

Figure 6.1 – Toronto beam drawn to scale

Very little, if any, laboratory testing on beams this size have been performed in the past. Bentz and Collins sent out an email to all ACI members (see Appendix A), asking them to consider calculating the following:

1. What is the value of the applied jack load, P, which in addition to the self-weight of the specimen will cause failure?
2. What is the location where the failure will occur?
3. If the East shear span of the slab strip contained the same shear reinforcement as that in the West shear span what would be the value of the applied jack load, P, which would cause failure?
4. For the actual specimen what will be the values for the downwards deflection of the bottom face of the specimen when the jack load P is at 0.25, 0.50, 0.75 and 1.00 of the predicted failure value given in 1)?

The compressive strength of the concrete is 40 MPa $(5801psi)$; the yielding strength, area per bar, and number of the *flexural* steel rebar for 20-M rebar and 30-M rebar are 522 MPa $(76\ ksi)$ and 573 MPa $(83\ ksi)$, 300 mm^2 $(0.456\ in^2)$ and $700mm^2$ $(1.06\ in^2)$, and 3 bars and 9 bars, respectively; the yielding strength, area per bar, and number of legs for the *shear* reinforcement 20-M rebar is 522 MPa $(76\ ksi)$, 300 mm^2 $(0.456\ in^2)$, and single leg bars, respectively ; the dimensions of the beam are 20 m $(66\ ft)$ by 4 m $(13\ ft)$; the type of supports, where the left is pin supported and the right is a roller; and the location at which they would load the beam, which is 7 m $(23\ ft)$ measured from the left support.

In the following section we attempt to first answer the four questions using the ACI318 code.

6.2 – ACI318 Predictions

6.2.1 – Static Analysis

Using simple statics, we developed a shear equation for the beam including the self-weight, *w*, of the beam and applied load, P. Figure 6.2 shows the beam with the self-weight and applied load.

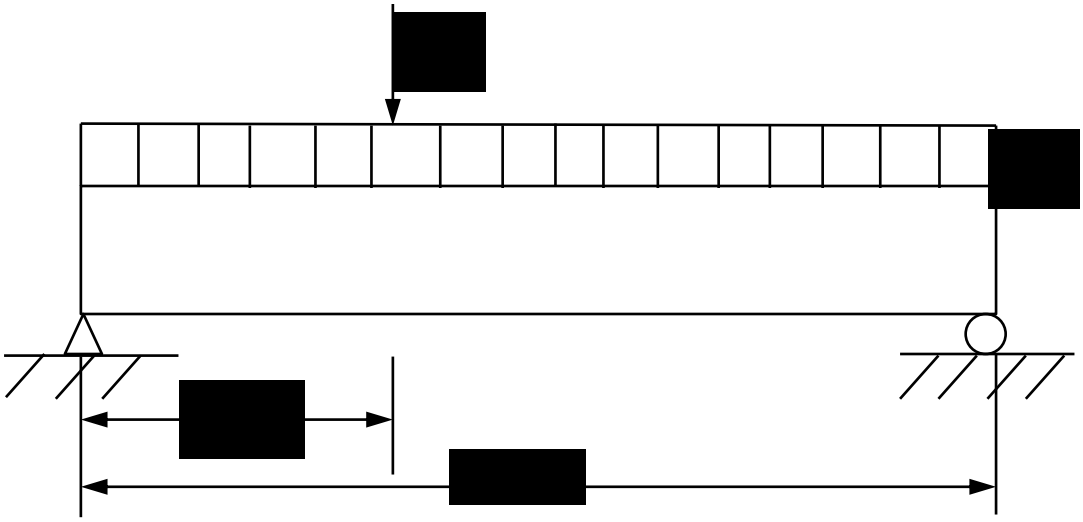

Figure 6.2 – Toronto beam with applied displacement and self-weight

w is equal to 2.19 $\frac{kN}{m}$ ($1.614\frac{kips}{ft}$); therefore, we developed the shear diagram for self-weight and the applied load. Figure 6.3 shows the shear diagram of the beam due to self-weight and Figure 6.4 the shear diagram for the applied displacement.

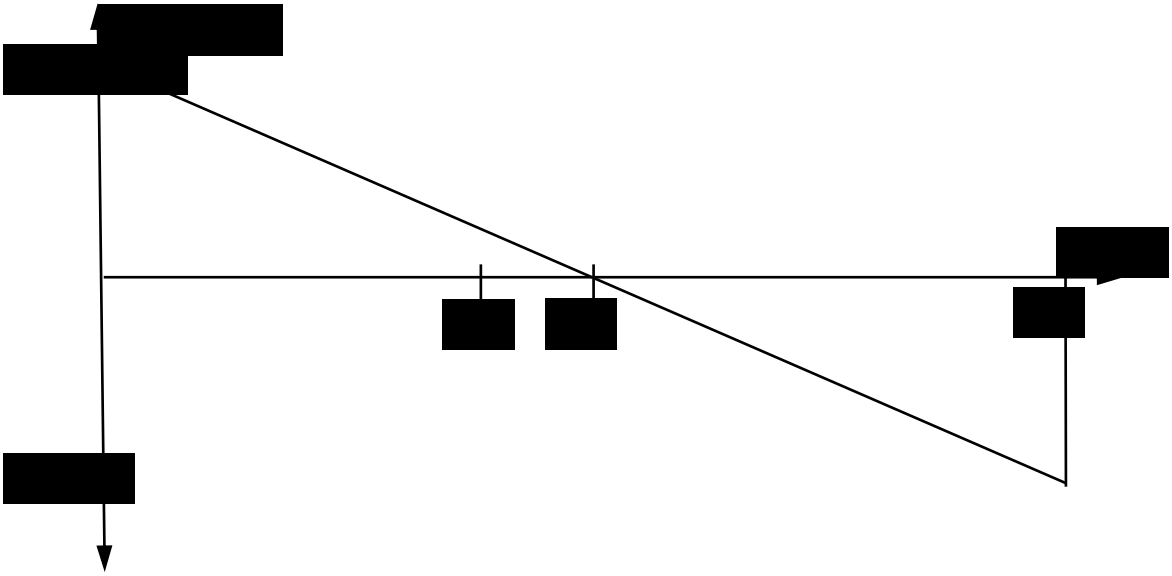

Figure 6.3 – Shear diagram for Toronto beam's self-weight

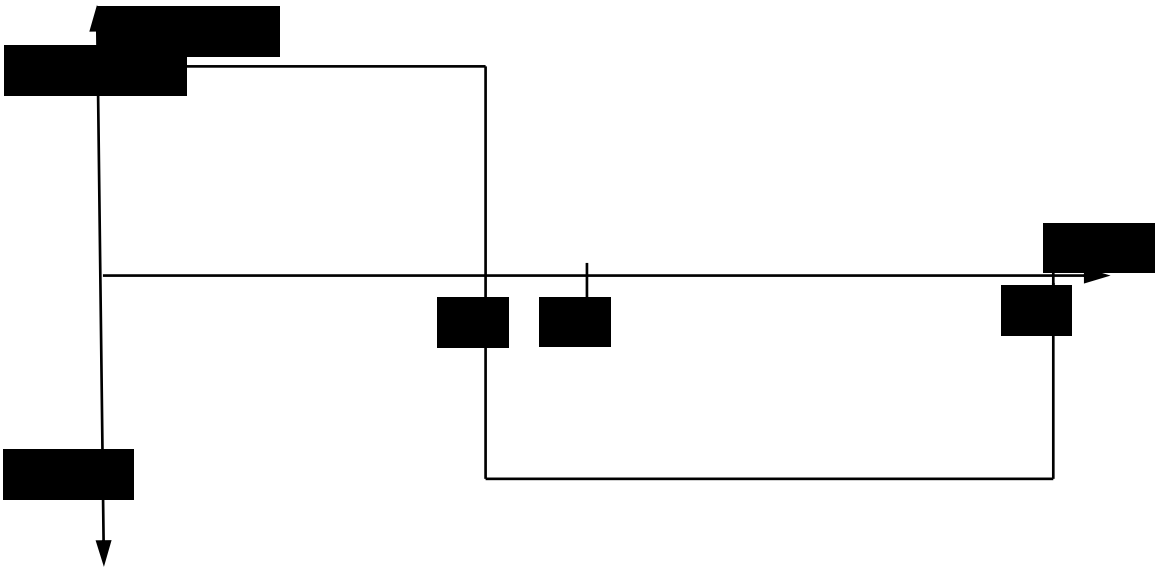

Figure 6.4 – Shear diagram for Toronto beam's applied displacement

Using the principal of superposition, we calculated the equations for shear failure in terms of the applied load. For the west side of the beam, the shear is equal to:

$$V_{maxWest} = 224.2 + 0.632P \ \ kN \ \ \ (50.31 + 0.632P \ \ kips).$$

And the shear for the east side of the beam containing no shear reinforcement is equal to:

$$V_{maxEast} = 224.2 + 0.368P \ \ kN \ \ \ (50.31 + 0.368P \ \ kips).$$

Performing the same static calculations above, Figure 6.5 shows the moment of the beam due to self-weight and Figure 6.6 shows the moment of the beam for the applied displacement.

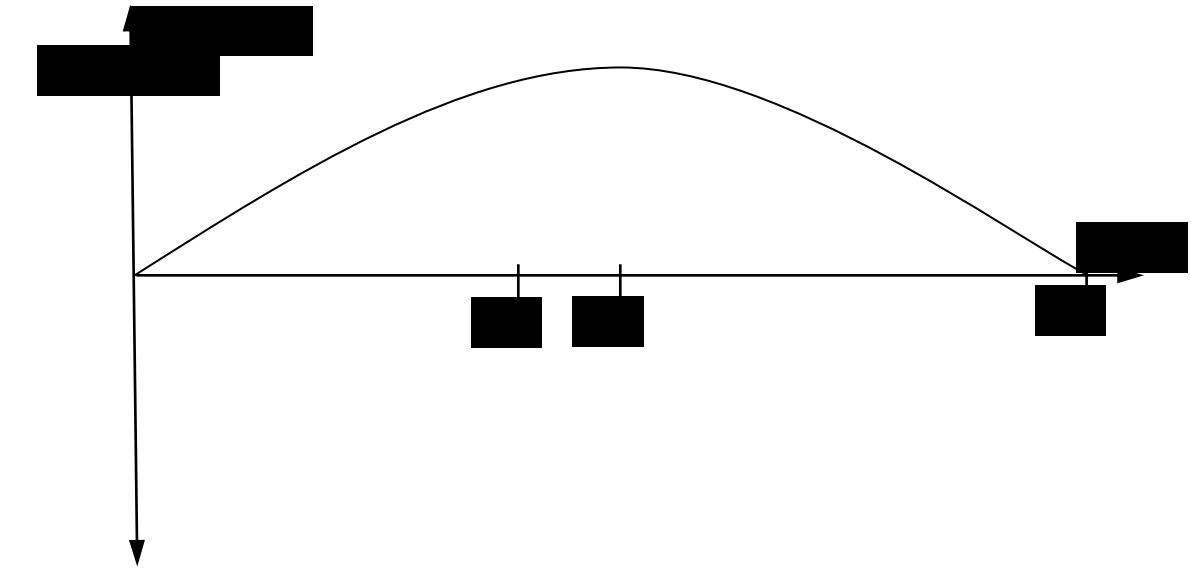

Figure 6.5 – Moment diagram for Toronto beam's self-weight

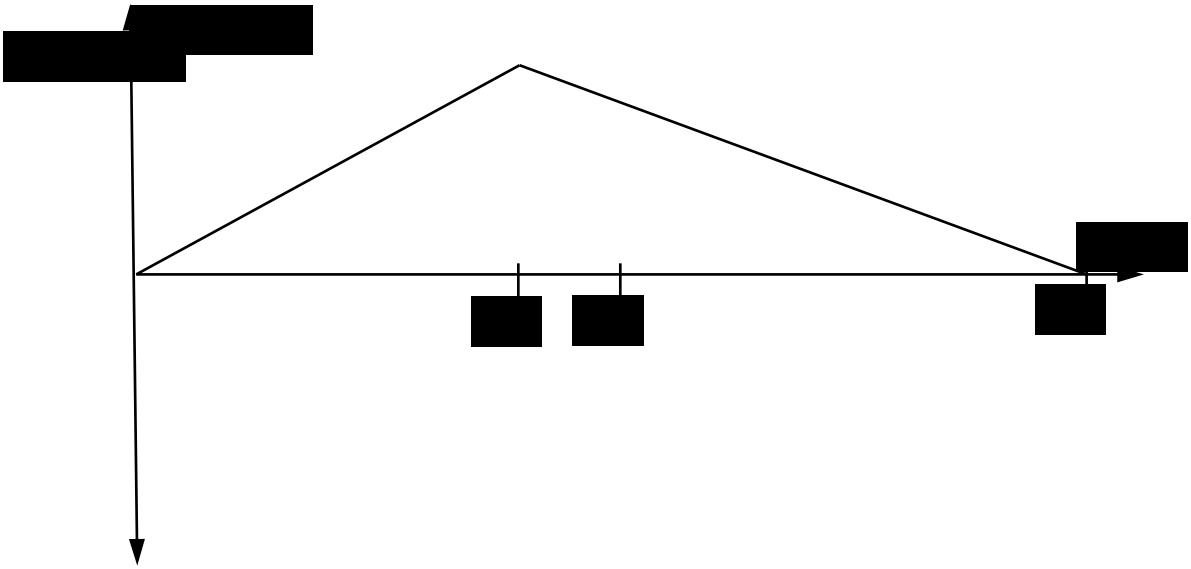

Figure 6.6 – Moment diagram for Toronto beam's applied displacement

Again, using the principal of superposition, we calculated the maximum total moment in terms of the applied load, P, to occur right under the loading point, 23 feet measured from the left support:

$$M_{max} = 991.2 + 4.42P \ \ kN - m \ \ \ (729.79 + 14.51P \ \ kip - ft).$$

We can thus use these equations to find the controlling applied load that would cause failure using ACI318 [13]. By doing this, we can calculate a rough applied displacement we will apply in the SPLM.

6.3.2 – ACI318 Shear Strength Prediction

Using Equations 2.27, 2.28, and 2.29:

$$V_c = 1008.1\ kN \quad (226.62\ kips);\ V_s = 394.9\ kN \quad (88.77\ kips);$$

$$V_n = 1402.9\ kN \ \ (315.39\ kips).$$

Thus, we calculated the controlling load, first, without shear reinforcement in the east side of the beam:

$$V_{n,W} = 0.632P + 224.2 = 1402.9\ kN\ (315.39\ kips) \text{ therefore,}$$

$$P_W = 1861\ kN\ (419.43\ kips).$$

Because, there is no shear reinforcement in the east side, we set the shear equation equal to the shear strength of plain concrete:

$$V_{n,E} = 0.368P + 224.2 = 1008.1\ kN\ (226.62\ kips) \text{ therefore,}$$

$$P_E = 2126\ kN\ (478.00\ kips).$$

According to ACI318, the west side controls shear strength.

6.3.3 – ACI318 Bending Strength Prediction

We used cross section equilibrium to determine our compression and tension forces, which would enable us to find the bending strength of the beam. Using Equations 2.31 and 2.32:

$$C_s = 413.7\ kN\ (93\ kips), \text{ and}$$

$$C_c = 3118.2\ kN\ (701\ kips).$$

We also know that the compression the member feels must be equal to the tension if equilibrium is to be kept. From Equation 2.34:

$$T = 3536.3\ kN\ (795\ kips).$$

Therefore, using Equation 2.33:

$$C_c + C_s = T = 3531.9\ kN\ (794\ kips).$$

Summing the moment about a tension point (Equation 2.30):

$$M_n = 12963\ kN - m\ (9561\ kip - ft\ )$$

Therefore, the controlling load due to moment is:

$$P_M = 2707\ kN\ (608.63\ kips)$$

Recalling the controlling shear strength, 1861 kN (419.43 kips), ACI318 predicts the beam will fail in shear on the west end.

6.3 – SPLM Prediction

6.3.1 – Preliminary Calculations

As shown in previous chapters, the SPLM models elasticity, plasticity, and damage for small two-dimensional and three-dimensional problems; therefore, a more complex problem may be investigated. The SPLM does not take into account an applied load, but rather, displacement is applied over time to simulate a point load. Therefore, we need to calculate an approximate displacement we can apply to the beam. This displacement should be that which would cause the beam to "fail" because it would be the displacement that would push the beam into the plastic region. The elastic displacement equation is:

$$\Delta = \frac{PL^3}{48EI} \text{ where,} \quad \textbf{(6.1)}$$

P is equal to the load applied to the beam (including self-weight), L is the length of the beam, and EI is the flexural rigidity of the beam. Using the parameters given in Figure 6.1, we calculated the deflection:

$$\Delta = 0.013\ m\ (0.51\ in).$$

We increased the total applied displacement in the SPLM to $0.04\ m$ $(1.5\ in)$ to ensure failure would be reached. Therefore, we have a rough starting displacement we can apply in the SPLM simulation.

Before we can analyze the beam using the SPLM, we calculated the fundamental period of the structure. The fundamental period is vital when running a model in the SPLM because the model applies a displacement for a certain number of fundamental periods. Furthermore, the critical time step is a function of the fundamental period. Calculating a critical time step produces smooth, accurate results. Using SAP2000 (Figure 6.7), we analyzed this beam as completely elastic with no damping to obtain the fundamental period. The beam was analyzed using a crude mesh under modal analysis with twelve modes. We show the deformed shape of mode 1.

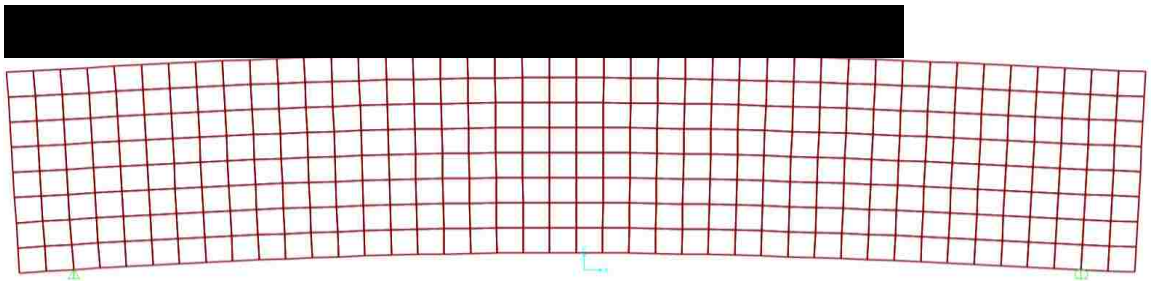

Figure 6.7 – Finite element analysis of Toronto beam

Thus, the fundamental period of the beam is 0.07593 seconds.

Using Equation 6.2,

$$\Delta t = \frac{1}{\pi c_o}\left(\sqrt{1+\xi^2} - \xi\right), \quad \textbf{(6.2)}$$

the critical time step is 7×10^{-6} seconds, which we analyzed over four fundamental periods or 50,000 time steps each time step being separated by the critical time step.

The particles, due to computer processing limitations, had a lattice spacing of $0.20\ m\ (7.87\ in)$. The top horizontal rebar and shear rebar were the same type of reinforcement, 20-M rebar, which has a cross-sectional area of $300\ mm^2\ (0.466\ in^2)$ and the bottom horizontal rebar, 30-M rebar, has a cross-sectional area of $700\ mm^2\ (1.09\ in^2)$. In the SPLM, we multiplied the area of an individual rebar by how many bars were located in the top and bottom of the beam and defined the shear reinforcement to have one leg and spaced at $1.5\ m(4.92\ ft)$. In addition to the beam's self-weight, the applied load, P, was applied under displacement control up to a peak displacement discussed in above.

6.3.2 – SPLM Results

Figure 6.8 shows the crack pattern for various times of the simulation and loading histories of the applied load. Notice the initial linearity of the force in the 'Force vs. Displacement' graph as the displacement is applied. From time equals 0 to point A the force in the particle being monitored seems to increase up to A linearly then goes 'bang', where a crack forms. This 'bang' occurs approximately around 7,000 time steps. Figure 6.8 B shows the time step of the bang and exhibits a flexural crack originating right under the applied load. Therefore, we predict that the failure load of the beam containing no shear reinforcement in the right (east) side of the beam to be $P_n = 2117\ kN\ (472\ kips)$,

as seen in Figure 6.8 C, which is 1.12 times greater than what ACI predicted ($P_n = 1861\ kN\ (419.13\ kips)$).

To answer question 2, which asked *where* the failure would occur, we observed the resulting crack pattern. Figure 6.8 B, C, and D show the crack pattern during loading.

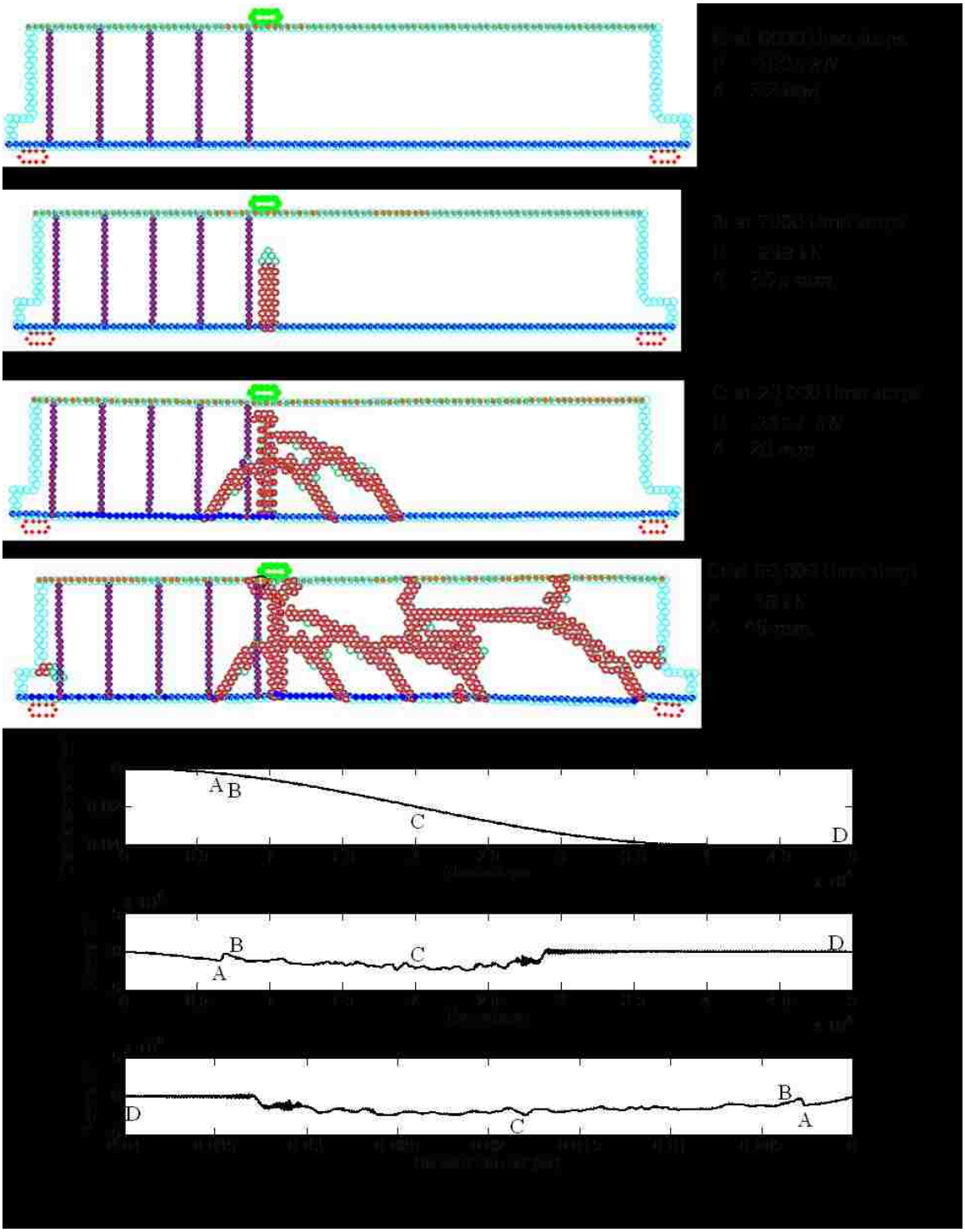

Figure 6.8 - SPLM results, showing damage (red), plasticity (black), load point displacement Δ, and applied load *P*, up to an applied displacement of $\Delta = 4\ cm$. 50,000 time steps total

It is apparent shear cracking occurred mostly on the right (east) side, which contained no stirrups. This is expected but not predicted, surprisingly, by ACI. ACI predicted failure

would occur in the west side of the beam. We assumed from our knowledge and understanding of shear, failure would occur in the east side. The SPLM also predicted this.

Recalling question three, which asked for the failure load if there was the same amount of shear reinforcement in the east side as the west side, we applied shear reinforcement in the east side. The reinforcement was spaced at 1.5 $m(4.92\ ft)$, the same as the west side. We kept the same parameters (time step, applied displacement for four fundamental periods, lattice spacing, amount of top and bottom horizontal rebar, and single leg shear reinforcement) that were used in the previous analysis to answer the first and second questions. Figure 6.9 shows the SPLM results of the simulation. Using the graphs in Figure 6.9, the failing load is $P_n = 2764\ kN$ $(621.4\ kips)$, which is 1.5 times greater than the ACI prediction of $P_n = 1861\ kN$ $(419.43\ kips)$. As expected, the strength of the beam increased with implementation of shear reinforcement in the east side of the beam.

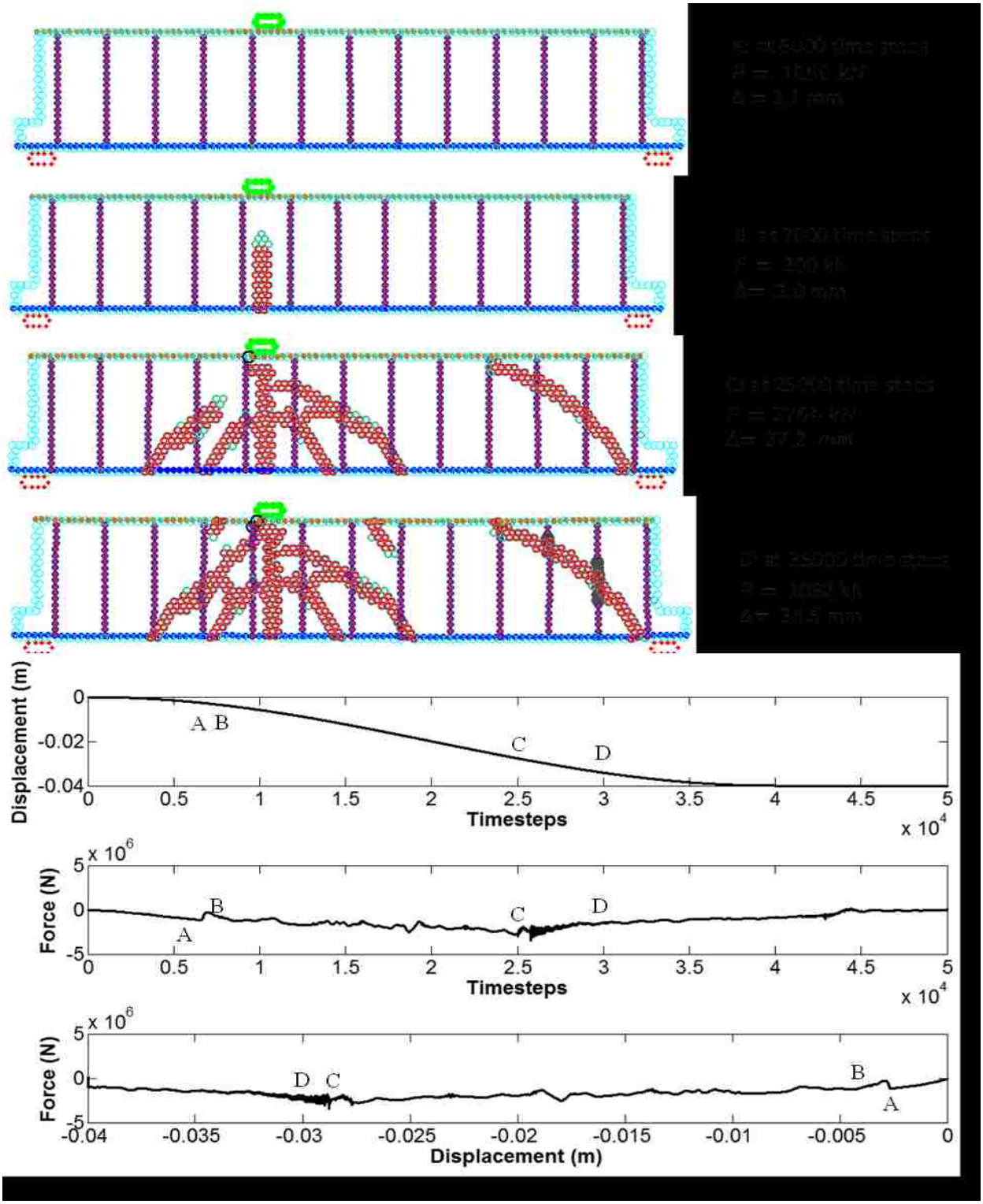

Figure 6.9 - SPLM results of beam with stirrups along entire length, showing damage (red), plasticity (black), load point displacement Δ, and applied load *P*, up to an applied displacement of Δ= 4 *cm* in 50,000 time steps. Note two yielded stirrups (grey) crossing shear crack at right

The displacements at $0.25 * P_n$, $0.5 * P_n$, $0.75 * P_n$, and $1.0 * P_n$, which is what question four asked for, where P_n is the applied load that would cause failure in the case *without* shear reinforcement in the east side, is shown in Figure 6.10.

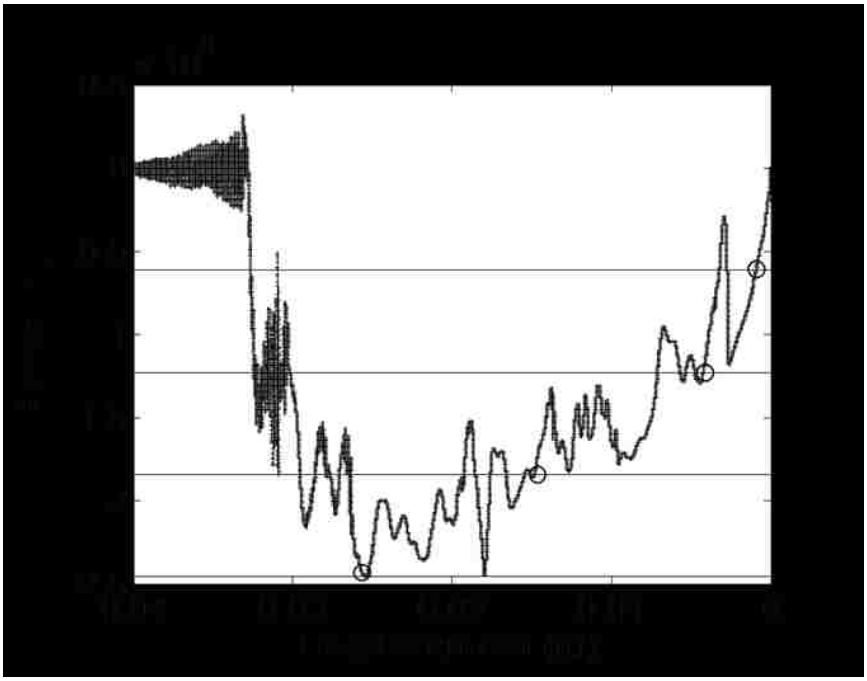

Figure 6.10 - Load versus displacement relation for original beam. First crossing points are marked with circular markers

The displacements for each specified load are circled in the figure above and equal to $\Delta_{0.25} = 1.0\ mm\ (0.039\ in)$; $\Delta_{0.50} = 4.2\ mm\ (0.165\ in)$; $\Delta_{0.75} = 14.8\ mm\ (0.583\ in)$; $\Delta_{1.0} = 25.3\ mm\ (1.0\ in)$.

6.4 – Laboratory Results

6.4.1 – Phase One Loading

Figure 6.11 shows the results of phase one loading, which consisted of applying the load to the beam with no shear reinforcement in the east side of the beam.

Figure 6.11 – Results of phase I

Notice the shear cracking pattern, the hydraulic loading piston, and the lateral torsional buckling supports perpendicular to the loading piston.

Figure 6.12 shows a close-up of the cracking pattern in the east side of the beam.

Figure 6.12 – Close-up of shear crack in east side of Toronto beam for phase I

Again, notice the shear cracking. According to the report from Bentz and Collins, this critical "flexural crack appeared at about 5 meters from the east support, spread

upwards and then turned towards the loading point and as this was happening the applied load (which was under displacement control) significantly decreased" (see Appendix B). Once the applied load significantly decreased, they stopped applying the load because of the desire to re-test the specimen after repairing the east end by implementing external "shear stirrups". Bentz and Collins state, "The specimen failed in shear in the east shear span (the 12 meter long side without shear reinforcement) when the applied point load, P, reached a value of 685 kN. " (see Appendix B)

Figure 6.13 shows a close-up view of the west side of the beam.

Figure 6.13 – Close-up of shear crack in west side of Toronto beam for phase I

According to Bentz and Collins, the west side of the beam "while containing significant diagonal cracks, showed no indication of being close to failure." (see Appendix B) This is very interesting, as ACI predicted failure to happen in the west side of the beam.

6.4.2 – Phase Two Loading

After applying four pairs of Dywidag bars, as seen in Figure 6.14, the beam was retested.

Figure 6.14 – Dywidag bars applied to Toronto beam in phase II

By doing this, they were able to determine the failure load of the beam as if there was the same amount of shear reinforcement in the east side of the beam as in the west. Figures 6.15 and 6.16 show the results of loading.

Figure 6.15 – Results of Phase 2

Figure 6.16 – Shear failure in west side of Toronto beam at 2162 kN (486 kips)

Notice the crushing that occurred right under the loading piston, which was seen in the SPLM as well. Also notice that the shear crack propagates at a near 45 degree angle from the bottom of the beam directly to the loading piston. Also notice the failure load of 2162 kN (486 kips), which was significantly higher that the failure load when the beam didn't have shear reinforcement in the east side of the beam (685 kN (154 kips)).

6.5 – Discussion of Results

6.5.1 – Summary of Results

Table 6.1 shows the summary of our results compared to ACI and the laboratory results.

Question	ACI318	SPLM	Laboratory
Failure load with no shear steel in east side	1861 kN (419 kips)	2117 kN (472 kips)	685 kN (154 kips)
Location of failure	West side	East side	East side
Failure load with shear steel in east side	2020 kN (454 kips)	2764 kN (621 kips)	2162 kN (486 kips)

Table 6.1 – Summary of ACI318, SPLM, and laboratory results for the Toronto beam

6.5.2 – ACI Prediction Discussion

ACI predicted a controlling failure load of 1861 kN (418 kips), which was 2.7 times greater than the laboratory results. Why did ACI predict such an unconservative strength? The author attributes its inadequacy to two reasons. One, the ACI code is based on hundreds of tests performed on small reinforced concrete beams. A beam this size had never before been tested, so how can we expect code written to express the results of small beams to accurately predict the shear strength of this massive beam?

Second, the ACI code especially can't predict the shear strength of this huge beam because nonlinear action in bigger beams is completely different than nonlinear action of smaller beams. Compare the fracture process zones of a small and large beam, for example. The entire depth of a small beam could be in the fracture process zone, whereas only a small fraction of the depth of a large beam could be in the fracture process zone. Therefore, the potential damage model is completely different based on the simple geometry of the beam.

6.5.3 – SPLM Discussion

Knowing that the SPLM reasonably models elasticity, plasticity, and damage, as seen in Chapters 3, 4, and 5 for smaller problems, we asked ourselves why our prediction was so different from the laboratory results. While the SPLM can model nonlinear action sufficiently, it also has limitations. One of those being the SPLM's inability to account for the self-weight deflection and an external displacement at the same time. In other words, the loading stages applied sequentially discussed in Chapter 5 was not applied to this prediction. Consequently, the particles were deforming under their own weight while

at the same time feeling an external displacement. This is unrealistic, as detailed in Chapter 5.

Our prediction also may be unconservative because of the lack of computational power. This was a massive beam. Therefore, in order to model it, we had to use a large lattice spacing. Essentially each particle in our prediction simulation was the size of a 6-inch concrete cylinder specimen. We chose to use this lattice spacing because of our limit in time, but we hypothesize that the SPLM prediction would have been much closer if the lattice spacing were reduced. Nonetheless, we applied the new bond-slip model and sequential loading and reran our analysis. We present the results in the next section.

6.6 – SPLM's Post-Diction

Using sequential loading discussed in Chapter 5 and the new bond-slip model discussed in Chapter 3, we reanalyzed the beam and ended up with different yet meaningful results. Figure 6.17 shows our post-diction SPLM results. The results are not what we expect but show promise for the model, that it has the potential to model known situations in reinforced concrete. The reason it shows potential, which we will show later, is based on a fundamental philosophical question. What is failure and when does it happen? Does a simple crack exemplify failure? No, as we know that reinforced concrete beams, like the Toronto beam presented in this chapter, can carry significant load after cracks appear. Moreover, is failure defined as failure in the steel, the concrete, or the overall collapse of the structure? This is a question that we think needs to be answered more specifically in all engineering applications.

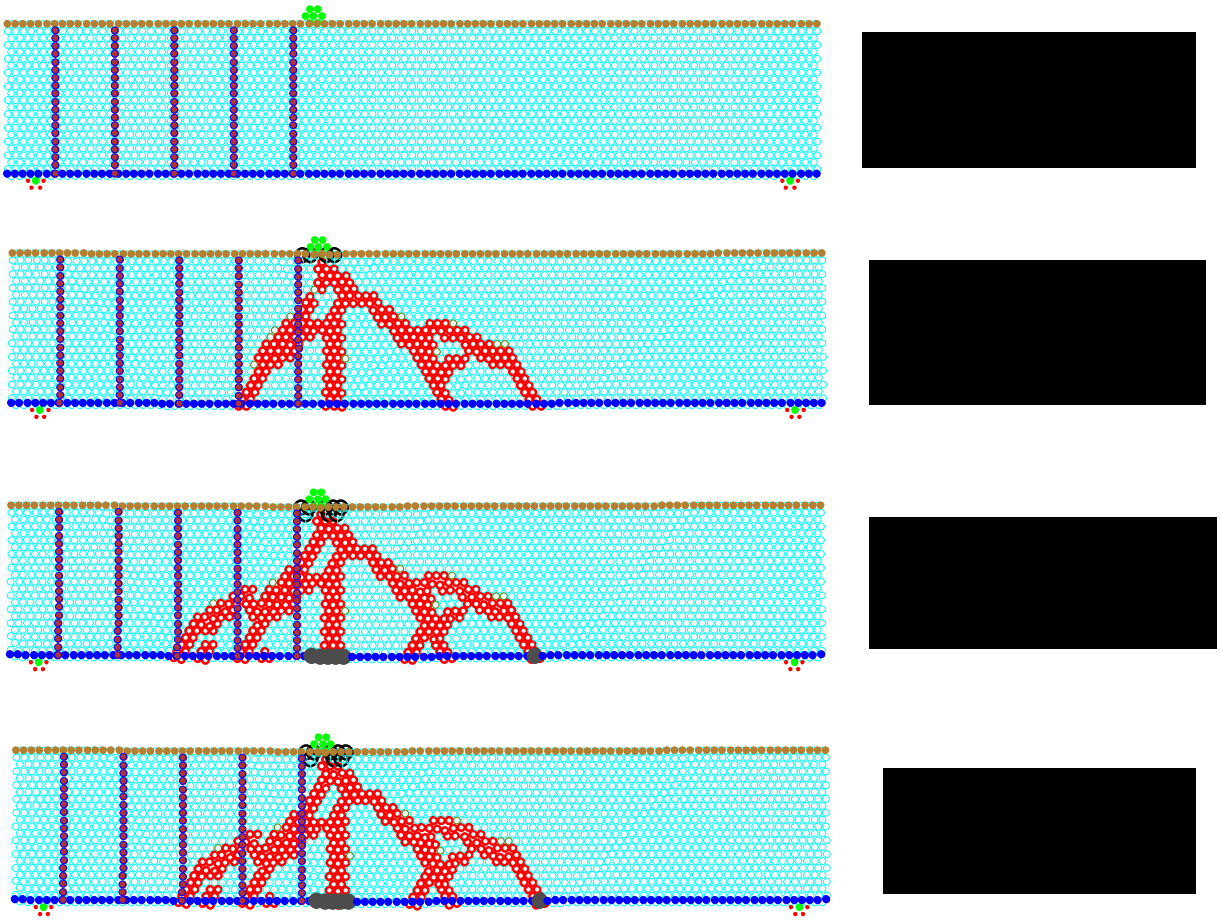

Figure 6.17 – SPLM post-diction

Figure 6.18 shows the load vs. displacement curve of the laboratory tests against our SPLM post-diction.

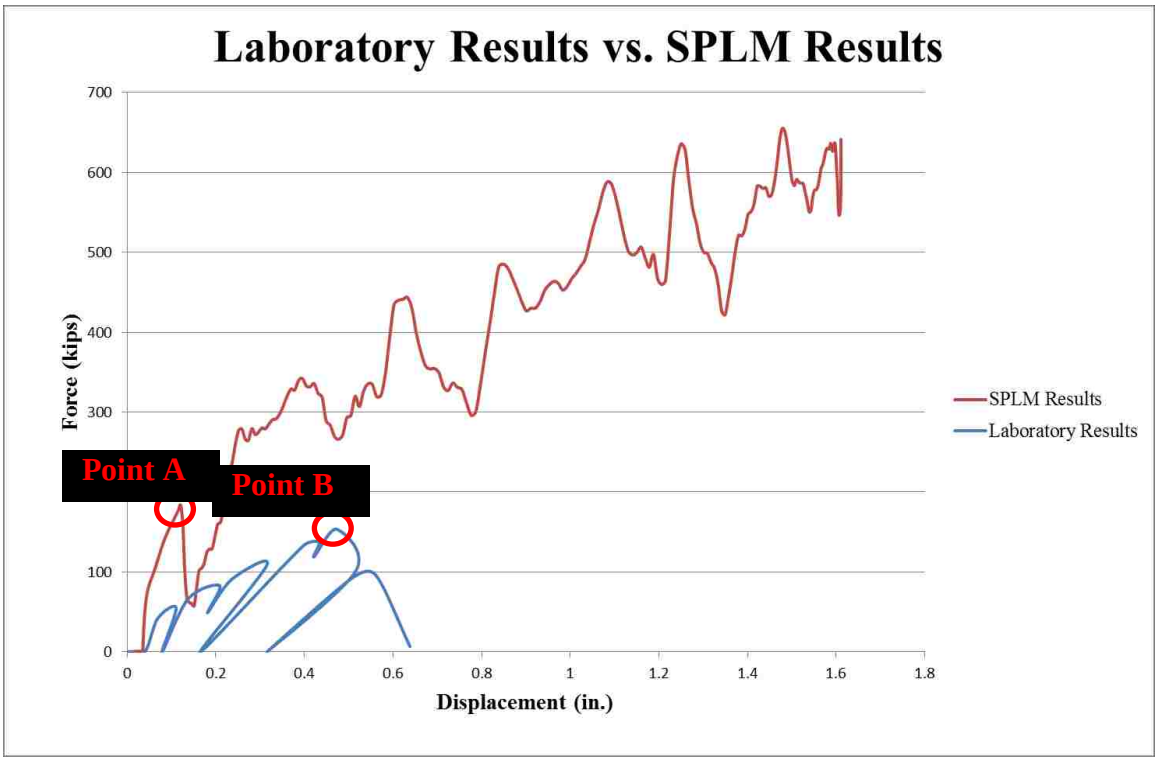

Figure 6.18 – Load vs. displacement curve comparing laboratory results and SPLM results

The curves above show us useful information. First, the SPLM seems to be initially responding in too stiff a manner. The high stiffness shown by the initial slope of the red line in the figure above may be different than the actual results because of its dependency on the constitutive relations between the stretch and force vectors for the particles or the SPLM's damage model may be incorrect. Second, the graph shows us that the SPLM has the potential to model a huge, practical problem like this. Notice that the displacements and loads the SPLM is predicting are close to that of the laboratory results. It is promising because the SPLM is not orders of magnitude off in its predictions. Third, going back to the philosophical question of failure discussed above, if failure for this beam is considered to be at Point A shown in Figure 6.18 then the SPLM predicts the beam's shear strength close to what was recorded in the laboratory (represented by Point B).

We can explain the post peak strength of the post-diction using the plasticity model. The SPLM assumes a perfect elasto-plastic model. In other words, the model accounts for plasticity but assumes that the "stress" a particle feels remains constant once the particle has gone plastic, equal to the tensile and/or compression strength of the material. It may be more realistic to say that the "stress" a particle feels would decrease once the particle has gone plastic. This will ensure the plastic particles are not adding strength to the structure. Doing so may even decrease the overall strength of structure, which, in the case of the Toronto beam, will be effective and more reasonable.

6.7 – Summary

The Toronto beam competition was a great opportunity to try out the SPLM. It opened up new doors for us and showed us bugs in the SPLM. Without opportunities like this, the world would stay where it is. Therefore, we are glad for the University of Toronto developing/hosting the competition.

To conclude the Toronto beam, the SPLM definitely shows potential. The cracking pattern of the SPLM is realistic and the applied displacements produce realistic loads. The ACI is unconservative when predicting the strength of extremely large beams. Using ACI to design a beam of this size at the bottom of a skyscraper, for example, could yield catastrophic results. Finally, the SPLM is compelling us to ask questions concerning definitions used in everyday engineering design such as stress, strain, and failure. What do these words really mean and do they change from problem to problem or from material to material?

Chapter 7

Conclusion

This chapter's objectives are to:

- Summarize this thesis
- Suggest future research to be done in the SPLM

In this work we presented the state-based peridynamic lattice model (SPLM) as it applies to reinforced concrete structures. We began with a brief review of classical linear mechanics, emphasizing the strengths and weaknesses. We proceeded to describe Silling's bond-based and state-based continuous peridynamic models and Gerstle's SPLM.

We developed a bond-slip model, which is a function of an interface horizon and stiffness between the steel and concrete. The bond-slip model proved reasonable for a tension-pull specimen modeled in two dimensions and three dimensions. We then used the new bond-slip model and Gerstle's elastic, plastic, and damage models to model four reinforced concrete beams where we validated each.

We also presented a sequential load application method for the SPLM, which increases the user's modeling capabilities. Sequential loading enables the user to view desired results quickly and efficiently. It also opens up the opportunity to model nonlinear deformation fields of structures loaded in different stages, such as prestressed concrete members.

Finally, we presented an SPLM prediction of a real world problem. We predicted the shear strength of an extremely large reinforced concrete beam. Surprisingly, the American Concrete Institute's (ACI's) prediction was underconservative as was the

SPLM's prediction. Interestingly, the strength of the beam increased after implementing the bond-slip model and sequential loading into the SPLM.

The SPLM has shown its ability to model simple and complex reinforced concrete structures. However, we feel the plasticity, damage, and bond-slip models need to be perfected. The current plasticity model has no post-peak relaxation. In other words, the current model assumes once the particle has plasticized, the "stress" remains constant for the rest of the simulation. This is unrealistic, as a particle's "stress" would decrease after plastifying, especially a concrete particle. This would lower the SPLM's strength prediction of the Toronto beam.

In terms of damage, the current model assumes that once the average stretch of all the bonds a particle feels surpasses a predetermined value, the particle is damaged. Is this realistic? We feel the model could be upgraded to be sensitive to damaged bonds. In other words, the model would consider the damage in each bond and determine whether that particle is damaged based on the damage in each bond that particle feels. This model has the potential to increase the SPLM's crack propagation prediction. The new model could also perfect the bond-slip model.

The current bond-slip model assumes the steel-concrete bond to act like a concrete-concrete bond. How realistic is this? Is this assumption realistic on the scale we are considering in the SPLM or should the model be refined to be sensitive to a specific concrete-steel bond?

The SPLM has shown its ability to model elasticity, plasticity, damage, and fracture in real engineering problems. With future work done in the areas suggested by

the author, the SPLM has the potential to compete with current design and analysis models.

References

[1] Wilde, R. E., "ACI: A Century of Progress," American Concrete Institute, Vol. 26, Issue No. 3, 2004.

[2] Gerstle, W. H., "Introduction to Practical Peridynamics: Computational Solid Mechanics Without Stress and Strain," World Scientific, 2015.

[3] Richardson, R., "The State-Based Peridynamic Lattice Model," M.S. Thesis, Civil Engineering Department, University of New Mexico, 2014.

[4] Silling, S. A., "Reformulation of Elasticity Theory for Discontinuities and Long-Range Forces," Journal of the Mechanics and Physics of Solids, 175-209, 2000.

[5] Silling, S. A., Epton, M., Weckner, O., Xu, J., and Askari, E., "Peridynamic States and Constitutive Modeling," Journal of Elasticity, 151-184, 2007.

[6] Newton, I., "The Principia," Berkeley: University of California Press, 1999.

[7] Timoshenko, S. P., "History of Strength of Materials," New York: McGraw-Hill, 1953.

[8] Navier, C. L., "Memoire sur les lois de l'equilibre et du mouvement des corps solides elastiques," Memoires de l'Institut, 375-384, 1827.\

[9] Cauchy, A. L., "Recherches sur l'equilibre et le movement interieur des corps solides ou fluids, elastiques ou non elastiques," Bulletin de la Societe Philomatique, 9-13, 1823.

[10] Gerstle, W. H. and Sau, N., "Peridynamic Modeling of Concrete Structures," Proceedings of the 5th Intl. Conf. on Fracture Mechanics of Concrete Structures, 949-959, IA-FRAMCOS, 2004.

[11] Gerstle, W., Sau, N., and Silling, S.,"Peridynamic Modeling of Plain and Reinforced Concrete Structures," 18th Intl. Conf. on Structural Mechanics in Reactor Technology (SMiRTl8), Beijing, China: Atomic Energy Press, 2005.

[12] Gerstle, W., Sau, N., Silling, S., "Peridynamic Modeling of Concrete Structures," Journal of Nuclear Engineering and Design, 1250-1258, 2007.

[13] ACI Committee, "Building Code Requirements for Structural Concrete (ACI 318-08 and Commentary," American Concrete Institute, 2009.

[14] Gerstle, W. H., "The Fracture Mechanics of Bond in Reinforce Concrete," M.S. Thesis, Department of Structural Engineering, Cornell University, 1982.

[15] Beeby, A. W., "A Study of Cracking in Reinforced Concrete Members Subjected to Pure Tension," Technical Report, Cement and Concrete Association, 42.468, 1972.

[16] Broms, B. and Raab, A., "The Fundamental Concepts of the Cracking Phenomenon in Reinforced Concrete Beams," Department of Structural Engineering, Cornell University, Report No. 310, 1961.

[17] Monti, G. amd Spacone, E., Reinforced Concrete Fiber Beam Element with Bond-Slip," J. Struct. Eng., 126(6), 654-661, 2000.

[18] Focacco, F., Nanni, A., and Bakis, C., “Local Bond-Slip Relationship for FRP Reinforcement in Concrete,” J. Comps. Constr., 4(1), 24-31, 2000.

[19] Shima, H., Chou, L., and Okamura, H., "Micro and Macro Models for Bond in Reinforced Concrete," Journal of the Faculty of Engineering, 39.2, 133-194, 1987.

[20] Houde, J. and Mirza, M., “A Study of Bond-Stress – Slip Relations in Reinforced Concrete,” Structural Concrete Series No. 72-8, McGill University, 1972.

[21] Goto, Y. and Otsuka, K., “Experimental Studies on Cracks Formed in Concrete Around Deformed Tension Bars,” The Technology Reports of the Tohoku University, Vol. 44, No. 1, 49-83, 1979.

[22] Gerstle, W. and Ingraffea, A., “Does Bond Slip Exist?,” Concrete International, Vol. 13, Issue 1, 44-48, 1991.

Appendix A

From: Michael P. Collins and Evan C. Bentz, University of Toronto

To: Engineers interested in the shear strength of reinforced concrete

Date: May 11th 2015

Re: Prediction contest for strength of four metre deep reinforced concrete slab strip

---

As part of research on the shear strength of very thick one-way slabs, we have constructed a reinforced concrete"slab strip" specimen four metres in overall depth and about twenty metres long. The specimen was cast on themorning of Monday April 27th 2015 and involved three truckloads of concrete (one per hour) for a total volume of 21cubic metres. In the photograph below, taken last Wednesday, the forms have been removed from the front (South)face and the marks left by the prefabricated forms and the holes from the form ties are clearly visible. The East endof the specimen is "cut back" so that it fits under the classrooms which are above this end of the laboratory.

For the three concrete trucks, the seven day strengths were 27, 32 and 31 MPa for bottom, middle, and top layers,while today the 14 day strengths are 33, 37 and 37 MPa for these three layers. We estimate that when the testing of the specimen commences two weeks from now the concrete strength should have reached about 40 MPa.

The figure below summarizes specimen geometry, reinforcement, loading arrangements and material properties. The density of the concrete at 14 days is 23.8 kN/m3. Note that the percentage of flexural tension reinforcement is 9 x 700/(250 x 3840) = 0.656 %. There is no shear reinforcement in the East 12 m long shear span, while in the West 7 m long shear span the amount of shear reinforcement is 300 x 522 / (250 X 1500) = 0.418 MPa. The nine longitudinal flexural tension bars and the five vertical bars used as shear reinforcement are all anchored with forged heads at their two ends. In addition the longitudinal tension bars have full-strength tapered threaded splices 1.43 metres to the east of the centre line of the load.

It would be appreciated if those of you interested in the current state-of-the-art of shear design could send us your predictions for some or all of the values below:

1) The value of the applied jack load, P, which in addition to the self-weight of the specimen will cause failure.

2) The location where the failure will occur?

3) If the East shear span of the slab strip contained the same shear reinforcement as that in the West shear span what would be the value of the applied jack load, P, which would cause failure?

4) For the actual specimen what will be the values for the downwards deflection of the bottom face of the specimen on line 2 when the jack load P is at 0.25, 0.50, 0.75 and 1.00 of the predicted failure value given in 1)?

It is planned to start loading the specimen on Monday 25th May and so to qualify as "predictions" your estimates should be received (email to bentz@ecf.utoronto.ca) by that date.

Thank you in advance for your interest and for your help.

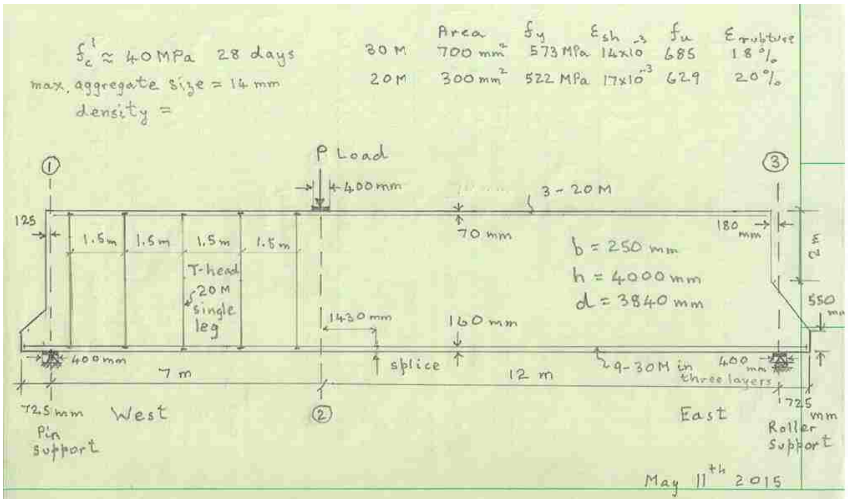

Appendix B

From: Michael P. Collins and Evan C. Bentz, University of Toronto

To Engineers who submitted predictions to the contest

Date: June 12th 2015

Re: Testing of strip from four metre thick one-way slab: Phase I results

---

This afternoon, after three days of testing, we finished the loading to failure in the first phase of our experiments on the shear strength of thick one-way slabs. The specimen failed in shear in the east shear span (the 12 metre long side without shear reinforcement) when the applied point load, P, reached a value of 685 kN. A new flexural crack appeared at about 5 metres from the east support, spread upwards and then turned towards the loading point and as this was happening the applied load (which was under displacement control) significantly decreased. Because we want to re-test the specimen after repairing the east end, we did not continue to load to produce total collapse of the east end.

While the reduced load and displacements were being held, the cracks were marked, crack widths were measured and X-Y displacements of surface targets were measured, See photo below.

The photograph below shows the critical diagonal shear crack. Note the black labels near the bottom of the member show the distance in metres from the east support. The measured crack widths, in millimetres, are given on labels beside the cracks.

The west side of the specimen, shown below, while containing significant diagonal cracks, showed no indication of being close to failure. Next week we will commence

phase II of the project by applying external “stirrups” to the failed east side of the specimen to allow additional load to be applied.

While extensive tracking of displacements and strains was conducted during the test, the simple X-Y plotter shown below was used to control the experiment. The plotter shows the relationship between the magnitudes of the applied point load on the Y axis against the deflection measured by an LVDT directly below the point load. Three University of Toronto professors made predictions and these were plotted on the graph paper prior to starting the test. First flexural cracking was observed at P = 198 kN and full load stages were taken at 250 kN, 325, 500 and 625 kN. At each load stage, the load was reduced somewhat to ensure safety of the students and lab technicians making the measurements. At the end of day one and day two of testing the load was reduced to zero overnight. The other reductions in load on the graph were caused by the formation of major new cracks.

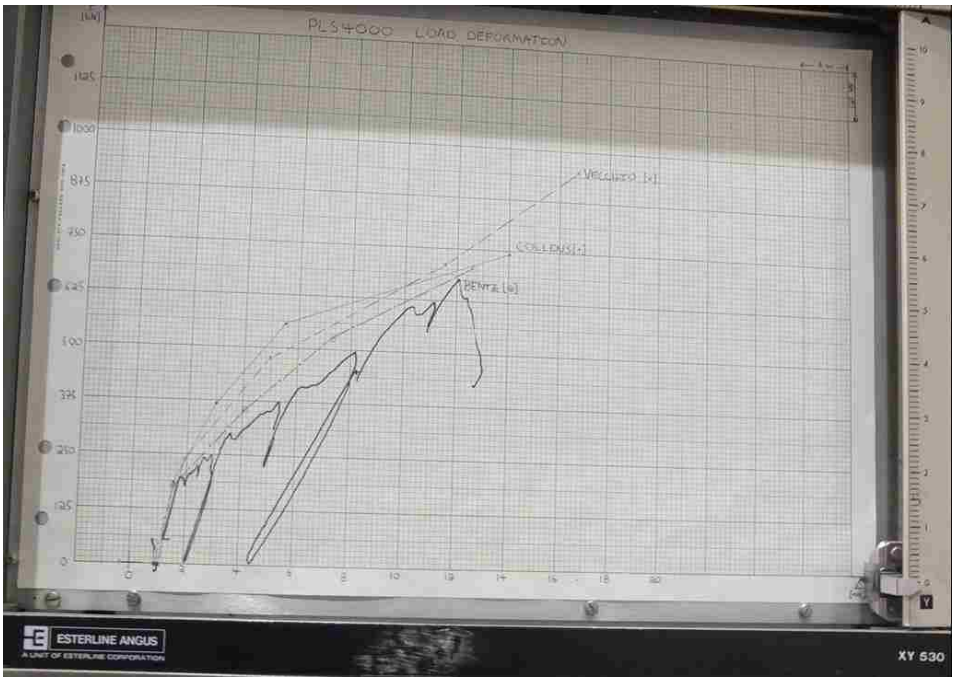

The photograph below shows the people who made this test possible. The creativity and problem solving abilities of the technical staff were crucial for this unique project. This includes lab manager Renzo Basset (on right) and chief technician John MacDonald (on left) assisted by technicians Bryant Cook, Michel Fiss and machine shop foreman Giovanni Buzzeo. This project will form part of the MASc thesis of Phil Quach who is seated at the front of the photo. Phil's Master's thesis will report on the testing of two specimens, the 4000 mm deep specimen in the background and the more traditionally sized 300 mm deep beam on which he is sitting.

From: Michael P. Collins and Evan C. Bentz, University of Toronto

To Engineers who submitted predictions to the contest

Date: June 15th 2015

Re: Reloading of strip from four metre thick one-way slab

A number of our colleagues upon receiving Friday's test summary indicated some doubts as to whether failure had actually occurred or was it simply the formation of the large diagonal crack that had caused the load deformation plot to reduce. To answer this concern, and to obtain more convincing photographs of the actual failure mechanism, we decided to reload the specimen this morning. The test has just completed with the maximum load that could be reached upon reloading being 433 kN. The very large widths of the failure cracks are currently being measured.

This photo shows the X-Y plotter at the end of the test. Note that the dropping of the load as the failure crack propagated occurred so quickly that the plotter pen left only a very light mark. If you zoom in, you can just see it. Note that the slope is consistent with the slope that occurred on Friday as the crack began to spread.

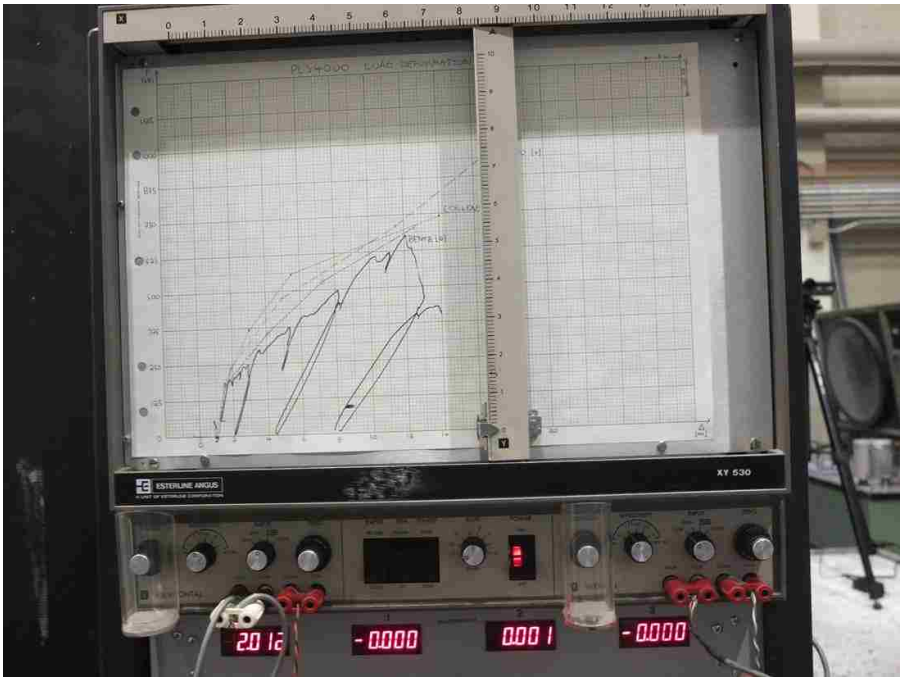

From: Michael P. Collins and Evan C. Bentz, University of Toronto

To Engineers who submitted predictions to the contest

Date: July 9th 2015

Re: Testing of strip from four metre thick one-way slab: Phase II results

---

On June 30th 2015 we failed the west end of the four metre slab strip specimen. The east end was repaired by applying four pairs of 36 mm diameter Dywidag bars, each bar post-tensioned to about 30 tons of force, see photo below.

The photo below shows the appearance of the west end at load stage 9. This load stage was taken when the applied point load had reached 1725 kN. As was the case for all load stages, the load was reduced significantly before cracks were marked, crack widths measured, and photos taken. Thus in the photo taken near the start of the load stage, the applied load can be seen to be 1600 kN.

Failure occurred by crushing of the compression zone near the loading point, what Prof. Boyan Mihaylov would call the Critical Loading Zone (CLZ). The load at failure was 2162 kN. The photograph below shows the specimen after failure had occurred.

A photograph of the XY plotter results are shown below. Like for the east end, the graph shows the applied load versus the displacement underneath the applied load.

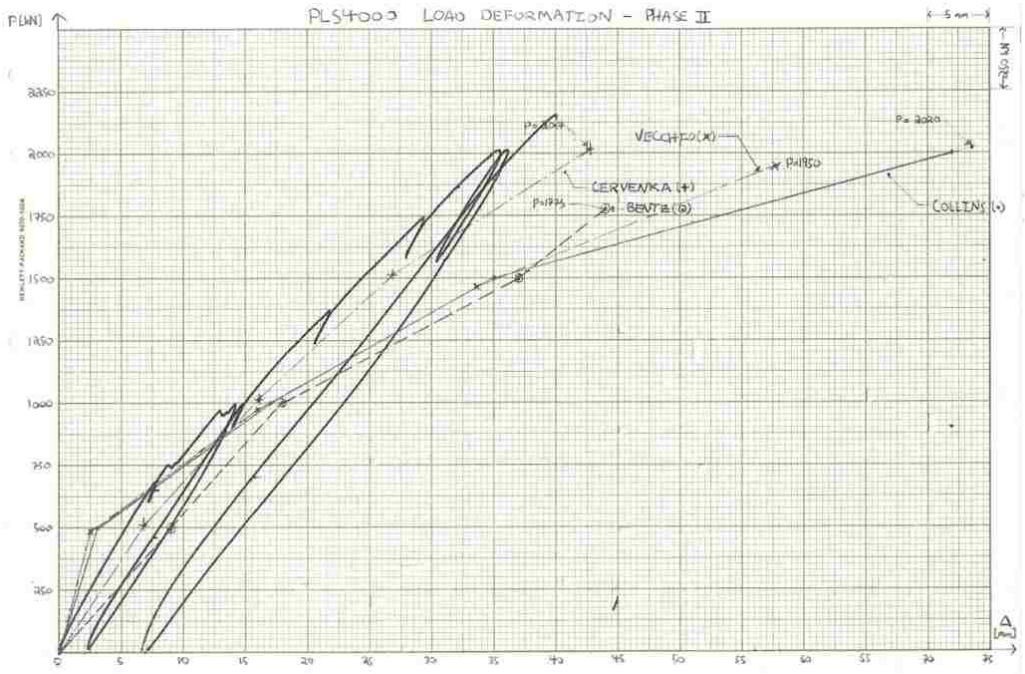

Results of Prediction Competition

The figure below compares the experimental result from the east shear span with the 66 predictions we received. Also shown are the predictions from a number of codes of practice. The yellow band indicates the range of plus or minus 10% from the observed strength. Thirteen of the predictions were within this "golden zone" of prediction. In other words, 20% of the predictions were excellent. Given the very large range shown in the figure, it is evident that predicting the shear strength of very thick slabs remains a challenging task.

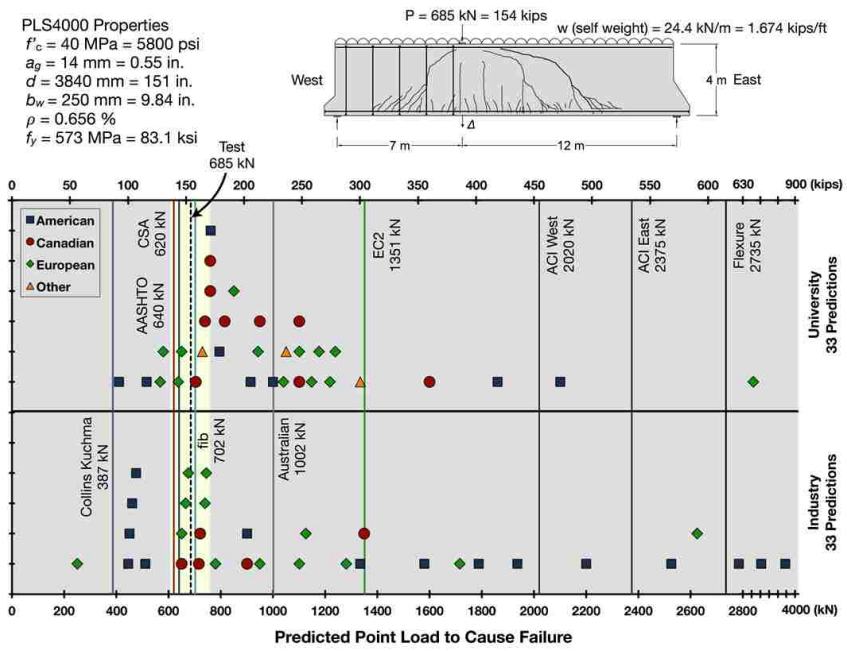

The figure below compares the observed load-deformation response during phase I with the predictions made in the contest. As with the load predictions, we have identified the entrants in terms of their place of residence and whether they come from industry or academia. The range of the predicted load deformation responses is surprisingly large. The prediction labelled "Cervenka" in solid green is the most accurate prediction of the load-deformation response.

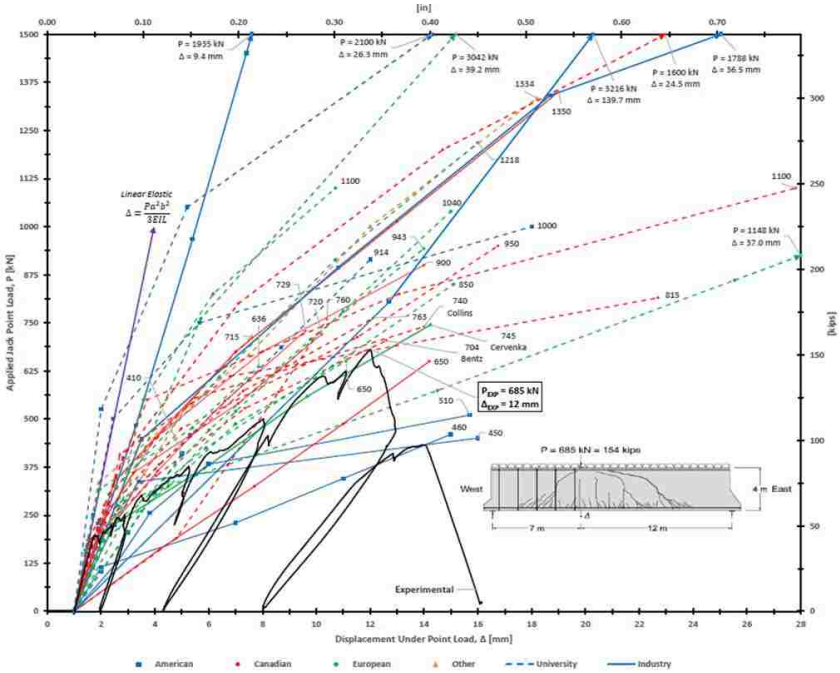

For the west end, the failure load predictions and the experimental result are compared below. Once again, about 20% of the predictions fall within the "golden zone" of plus or minus 10% from the experiment.

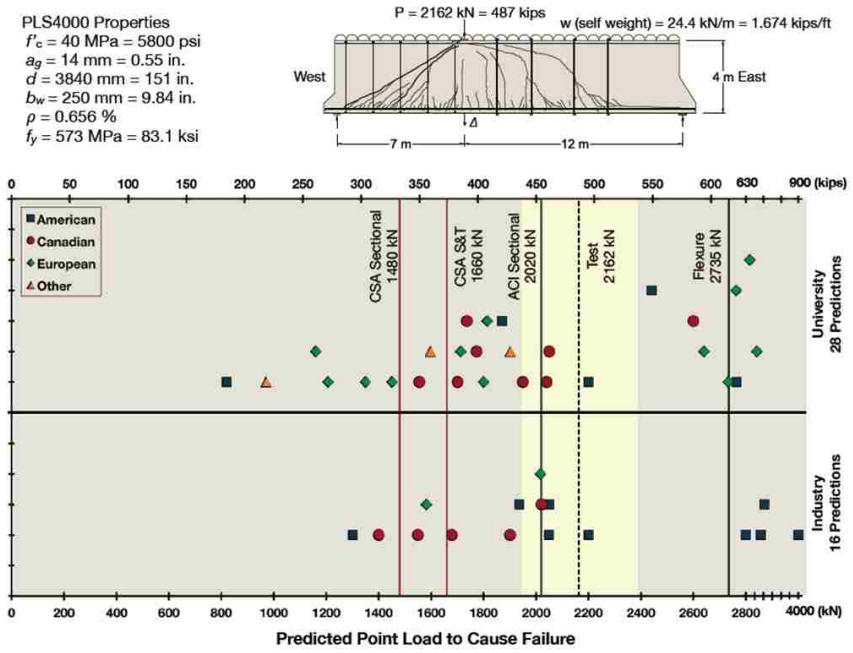

Only two of the entries were within plus/minus 10% for both the east and west end predictions. These were:

· Cervenka Consulting, of Prague, Czech Republic

· SNC-Lavalin Hydro & Prof. M.B. Ftima of École Polytechnique de Montréal, Canada

They both submitted entries based on nonlinear finite element analysis programs which they developed. Of these two excellent predictions, the load-deformation prediction from Cervenka Consulting was better and, thus, the winner of the contest is:

Cervenka Consulting with the report written by Vladimir Cervenka and Tereza Sajdlova.

Congratulations to them for an excellent job. It is interesting to note that the last shear response prediction contest conducted by the University of Toronto was in 1982 and it was also won by Vladimir Cervenka. At that time, his predictions were the only ones to be within 17% of the observed values for each of the four panels. Given that we now have two predictions within 10% of the observed values, the profession has definitely made progress in the past 30 years.